UC Berkeley
UC Berkeley Electronic Theses and Dissertations

Title
Studies of Inter-and Intra-Molecular Coordination in Cytoplasmic Dynein

Permalink
https://escholarship.org/uc/item/2hb6m146

Author
DeWitt, Mark Alan

Publication Date
2014

Peer reviewed|Thesis/dissertation

eScholarship.org Powered by the California Digital Library
University of California

Studies of Inter-and Intra-Molecular Coordination in Cytoplasmic Dynein

By

Mark Alan DeWitt

A dissertation submitted in partial satisfaction of the

requirements for the degree of

Doctor of Philosophy

in

Biophysics

in the

Graduate Division

of the

University of California, Berkeley

Committee in charge:

Professor Ahmet Yildiz, Chair

Professor Carolyn Bertozzi

Professor Eva Nogales

Professor Ke Xu

Spring 2014

Abstract

Studies of Inter- and Intra-Molecular Coordination in Cytoplasmic Dynein

by

Mark Alan DeWitt

Doctor of Philosophy in Biophysics

University of California, Berkeley

Professor Ahmet Yildiz, Chair

Cytoplasmic dynein is one of the principle motors in eukaryotic cells, responsible for most microtubule (MT) minus end-directed motility and force generation processes, including vesicular and organelle transport, and mitotic spindle MT organization. Despite being essential to the maintanence of cellular structure in higher eukaryotes, many aspects of dynein's stepping mechanism have remained enigmatic. In this Dissertation, I directly observe several fundamental aspects of dynein's mechanism, and build a strong framework for future studies. I outline in detail the methods for the fluorescent tracking of motor proteins, including advanced two-color and super-resolution techniques. To study cytoplasmic dynein, I developed a two-color fluorescent tracking assay to simultaneously measure the positions of both heads of the motor while it walks along the MT. The results of this experiment clearly show that dynein steps through a unique mechanism: the heads remain widely separated, and do not appear to coordinate with each other to a significant extent. However, the leading head is less likely to take a step at large inter-head separations, indicating some degree of residual coordination remains. I hypothesized that tension along the linker connecting the two heads is the source of this coordination. Using a high-speed two-color assay, I examined the motility of a homodimeric dynein with a flexible linker between the two heads that decreases inter-molecular tension. Despite this alteration, this homodimer has identical stepping and overall motility properties to wild-type dynein, but has reduced coordination, indicating that coordination is dispensable to motility. Coordination could be achieved by gating one of the heads. I investigated gating using a heterodimeric dynein with a wild-type head and an inactive, tightly-bound head. In this heterodimer, we find that the WT head is gated when widely separated from its inactive partner, but becomes un-gated when immediately behind it, indicating that the gating is caused by extension-dependent changes in linker tension as predicted. I next I turned from inter- to intra-molecular communication. Dynein has six distinct AAA subdomains on its motor head, of which only two AAA1 and AAA3, are essential to robust motility. By reducing MT affinity with added salt, I found that AAA3 is required for robust MT release, and that MT release in turn promotes hydrolysis at AAA1. To investigate coordination between AAA1 and AAA3, I analyzed motility in the presence of a slowly-hydrolyzable ATP analog, ATPγS. I found that ATPγS selectively inhibits the AAA3 site. In the presence of saturating analog, the motor can still take long runs of fast motility, indicating that the hydrolysis cycle of AAA3 is much shorter than AAA1. These results show that AAA1 and AAA3 do not coordinate. Instead, AAA3 acts as a "switch" that controls AAA1-directed release from the MT.

ACKNOWLEDGEMENTS

I gratefully acknowledge the excellent guidance and supervision by my advisor, Ahmet Yildiz. I would not be the scientist I am today but for him.

I also recognize the contributions of my previous two supervisors. My undergraduate advisor Arthur Glasfeld introduced me to the joy of laboratory research. My supervisor after college David Farrens taught me the discipline and focus required of all succesful scientists.

I also acknowledge all the fantastic people who supported me during my years at Berkeley: My family: Janet, Chip, Julia and Rebecca, and my friends: Cliff Collins, Joe Kliegman, Will Draper, Joshua Brown and my friend, colleague, and erstwhile paramour Sisi Chen.

Like all successful research, the work presented here is entirely collaborative. I acknowledge the specific contributions of some of the talented scientists I have worked with here at Berkeley:

Chapter 1: Adapted from a chapter co-written with my advisor, Ahmet Yildiz

Chapter 2: Adapted from a published article (DeWitt et al., 2012) co-authored with Ahmet Yildiz, Amy Chang, and Peter Combs. Co-written with Ahmet Yildiz. Amy Chang collected the one-color data. Peter Combs and I co-developed the image registration method.

Figures and text are reprinted with permission from (DeWitt et al., 2012).

Chapter 3: Constructs were the generous gift of Frank Cleary. The data presented is incorporated in two manuscripts written by Frank Cleary and Ahmet Yildiz, now under review.

Chapter 4: Adapted from a manuscript in preparation co-authored by myself, Ahmet Yildiz, and Caroline Segura. Co-written with Ahmet Yildiz. Caroline Segura collected the WT dynein pausing data under my supervision.

TABLE OF CONTENTS

Chapter 1. An Overview of Fluorescent Tracking Methods for Motor Proteins **1**

1.1 Summary 1

1.2 Imaging of Single Molecules 1

1.3 Particle Tracking Beyond the Diffraction Limit: Theory and Practical Considerations 2

1.4 Tracking Fluorescently Labeled Molecular Motors *in vitro* 4

1.5 Applications of Single-Color Tracking of Molecular Motors *in vitro* 8

1.6 Two-Color Fluorescence Tracking: Theory and Practice 10

1.7 Other Tracking Methods for Studying Processive Cytoskeletal Motors 15

1.8 Conclusion 18

Chapter 2: Cytoplasmic Dynein Moves Through Uncoordinated Stepping of the AAA+ Ring Domains **19**

2.1 Summary 19

2.2 Introduction 19

2.3 Results and Discussion 19

2.4 Materials, Methods, and Supplemental Data 28

Chapter 3: Investigating the Role of Linker Tension in Dynein Motility Using Two-Color Fluorescence **34**

3.1 Summary 34

3.2 Introduction 34

3.3 Two-Color Experiment on a Dynein with Reduced Linker Tension 35

3.4 Two-Color Experiment on a Dynein with Increased Linker Tension 37

3.5 Conclusion 40

3.6 Materials and Methods 41

Chapter 4: The AAA3 Domain of Cytoplasmic Dynein Acts as a "Switch" to Facilitate MT Release **44**

4.1 Summary 44

4.2 Introduction 44

4.3 Results 45

4.4 Discussion 56

4.5 Materials and Methods 59

References **63**

CHAPTER 1. AN OVERVIEW OF FLUORESCENT TRACKING METHODS FOR MOTOR PROTEINS

1.1 Summary

Motor proteins convert the chemical energy of adenosine triphosphate (ATP) hydrolysis into directed movement along filamentous tracks, such as DNA, microtubule and actin. The motile properties of motors are essential to their wide variety of cellular functions, including cargo transport, mitosis, cell motility, nuclear positioning and ciliogenesis. Detailed understanding of the biophysical mechanisms of motor motility is therefore essential to understanding the physical basis of these processes. Which direction is the motor going? How fast and how far can a single motor walk down its track? How is ATP hydrolysis coupled to directed motion? How do multiple subunits of a motor coordinate with each other during motility? These questions can be addressed directly by tracking motors at a single molecule level. This chapter will focus on high-resolution fluorescence tracking techniques of the processive cytoskeletal motors: myosins, kinesins, and cytoplasmic dynein. I outline the theoretical and practical considerations for studying the motors *in vitro* using fluorescence tracking at nanometer precision.

1.2 Imaging of Single Molecules

Direct observation of the motility of subcellular structures, including molecular motors, long remained elusive due to lack of appropriate microscopy techniques. The development of transmission light microscopy methods (e.g. brightfield, differential interference contrast, phase contrast methods) and digital video microscopy allowed tracking the movement of large (>~300 nm) organelles and microtubule filaments (Horio and Hotani, 1986). However, most organelles and all individual proteins were invisible, because they do not have sufficient contrast to be detected using these methods. Early attempts to track single molecules involved attachment of large beads or long polymers to make their motility visible under a microscope (Gelles et al., 1988). However, these methods are usually limited to *in vitro* applications because of the large probe size, and provide information about the overall motility of a motor (e.g. speed and run length and directionality). They are not suitable for *in vivo* labeling or high resolution tracking, because of the Brownian motion of the large probe under thermal fluctuations. Optical trapping methods have frequently been used to study the movement of molecular motors under an applied load (Ashkin et al., 1986; Finer et al., 1994; Svoboda and Block, 1994), in which the Brownian motion of the bead is greatly reduced and the bead position can be tracked with sub-nanometer resolution.

Single-molecule detection of fluorescent dyes (Moerner and Kador, 1989) has opened new opportunities in particle tracking studies, because of their small size, availability of site-specific labeling strategies for protein conjugation, and high signal to noise ratio (SNR). Due to the large Stokes shift between the absorption and fluorescence emission, fluorophores can be excited by intense laser illumination and fluorescent photons are readily isolated using optical filters, allowing detection of extremely weak signals. However, the detection of single fluorophores in solution posed a bigger challenge because the signal of a single fluorophore is usually weaker than the Raman scattering of 1 μm^3 of water, which overlaps with the spectrum of the fluorescence emission. In order to minimize the background, several attempts centered on reducing the excitation volume, effectively reducing the Raman signal. Confocal microscopy focuses light into

a diffraction limited spot and utilizes a small pinhole in front of a single-channel detector to block out-of-focus light, allowing 3D imaging of whole cells at single molecule sensitivity. However, in order to create an image using confocal microscopy, the focused spot needs to be scanned over the region of interest. As a result, the time resolution of scanning confocal microscopy is lower than wide-field excitation, which limits its suitability for tracking fast-moving particles. The development of spinning disk confocal greatly improved the time resolution of the confocal method, at the cost of reduced signal detection and high crosstalk between adjacent pixels due to spurious emission from out-of-focus planes, which can increase background in thick samples (Shimozawa et al., 2013).

Axelrod and coworkers used total internal reflection (TIR) of the excitation light to greatly improve the sensitivity of fluorescence detection without sacrificing time resolution (Burghardt and Axelrod, 1981). TIR creates an evanescent field at the glass/water interface of a sample chamber (Fig. 1.1a). The evanescent wave does not propagate through the sample and illuminates to a depth of ~100 nm in water, greatly reducing the Raman cross section. The method is only applicable when the imaged object is bound to the coverslip surface (for *in vitro* imaging) or at or near the cell surface (*in vivo*). Use of TIR alone greatly reduces the background, but SNR still suffers from the glow of objective lenses and scattered light bypassing fluorescence filters, when the TIR beam is sent directly through the objective. In order to further reduce the background, the TIR beam can be directed to the top surface of the sample chamber using a prism. As a result, the excitation path is fully separated from the detection path, which results in further improvement in SNR. Use of TIR microscopy allowed detection of single fluorescently labeled motors in solution (Funatsu et al., 1995; Vale et al., 1996). Due to the combined ease of use, superior SNR, and high time resolution, TIR is the most widely used method for tracking motor proteins *in vitro*.

1.3 Particle Tracking Beyond the Diffraction Limit: Theory and Practical Considerations

While the development of fluorescent TIRF video microscopy allowed routine tracking of individual fluorescent molecules, the ability of conventional light microscopy to resolve fine details in the image plane is limited by the diffraction of detected light. Small particles cannot be observed smaller than the width of the diffraction-limited spot, the so-called Point Spread Function (PSF, Fig. 10.1b) (Bobroff, 1986). The width of the PSF is equal to $\lambda/(2NA)$, where NA is the numerical aperture of the microscope objective (1.4 – 1.65 NA objectives are available). For visible light, this makes resolution of distances smaller than 200-300 nm impossible (Yildiz and Selvin, 2005).

High-resolution fluorescence tracking is a means of getting around the diffraction limit, and determining the "true" location of a fluorophore with nanometer accuracy. However, it only works under certain conditions. First, a fluorophore must act as an isotropic emitter during the acquisition of each image (Enderlein et al., 2006) and the microscope is free of aberrations to ensure that the center of the PSF represents the position of a dye (Bartko et al., 2002). Second, the fluorophores must be physically separated so as to produce distinct spots, and the spot must be sufficiently bright. This makes imaging of fluorescent molecules in crowded environments (e.g. in cells) very challenging, unless both photoactivation (Betzig et al., 2006; Huang et al., 2008; Rust et al., 2006) and localization techniques are employed.

Another challenge in tracking single fluorophores is the precise localization of particle position. To find the center of PSF, the spot intensity profile is fitted to a peak function, and the

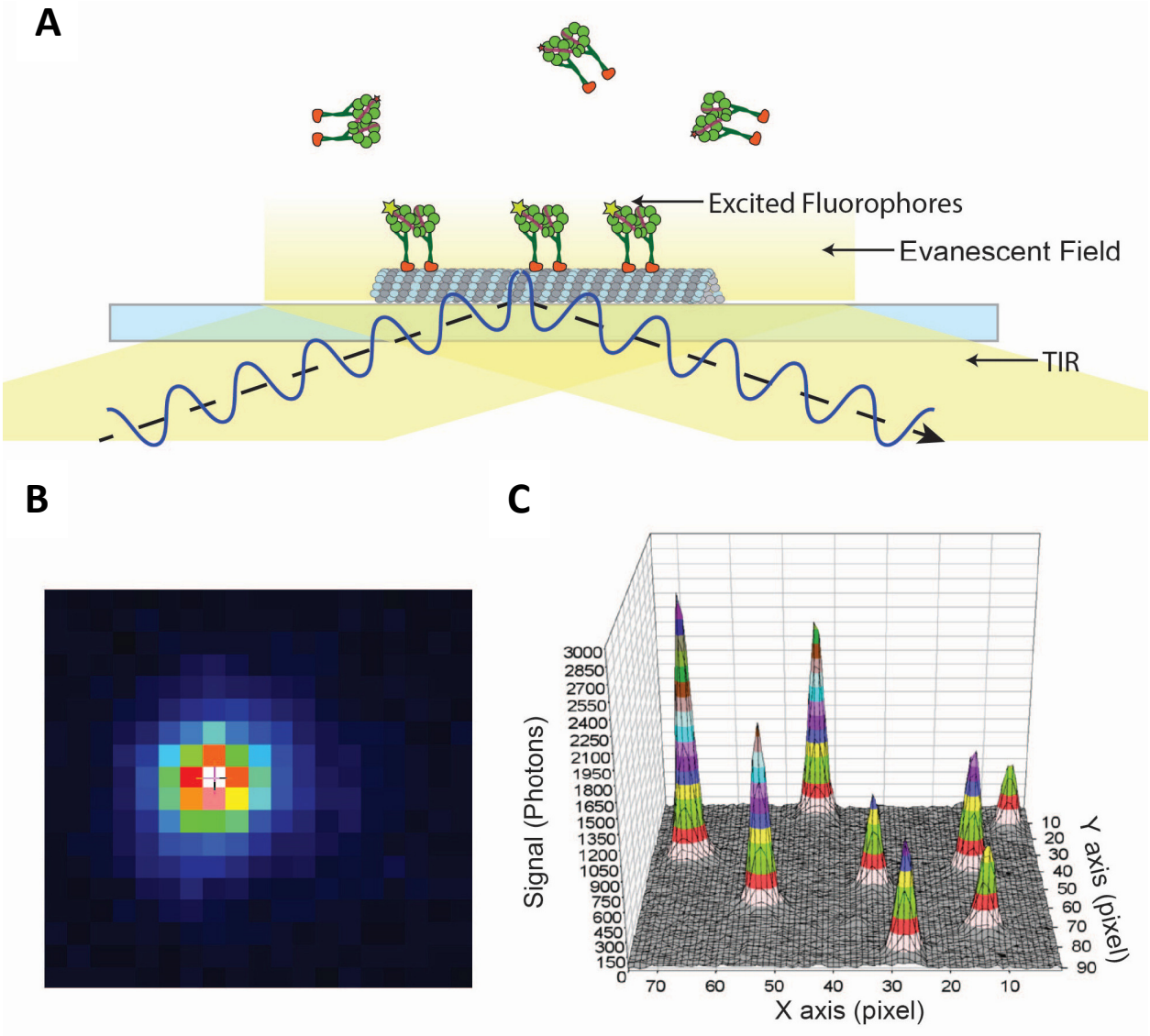


Figure. 1.1 Fluorescence tracking of molecular motors. **(a)** Schematic of typical *in vitro* single-molecule motility assay. Cytoskeletal tracks are immobilized on a glass coverslip. Fluorescently-labeled motors are flown into the sample chamber. Excitation light is total internally reflected at the glass water boundary of a coverslip. Evanescent field created by the TIR excitation decays exponentially with 100 nm decays constant. Therefore, fluorescently-labeled motors bound to cytoskeletal filaments are selectively excited, in the presence of diffusing motors in the chamber, **(b)** Image of individual fluorophores are diffraction limited and generate PSFs, **(c)** Three dimensional representation of a camera image shows that individual PSFs can be approximated by a two-dimensional Gaussian. While the width of the Gaussian is large (~300 nm), its center can be tracked with nanometer precision if a sufficient number of photons per image is collected

center of this fit is taken as the true location of the emitter (Fig. 1.1c). Most particle tracking algorithms fit the intensity profile to a two-dimensional Gaussian function, which is a good approximation of the central peak of the PSF (Thompson et al., 2002). However, other algorithms have been employed, such as centroid tracking or Gaussian mask fitting, although these can introduce biases into tracking data and/or reduce tracking accuracy (Cheezum et al., 2001). Recently developed maximum-likelihood fitting with empirical functions that better approximate

the PSF can improve the fitting by up to one third, without the biases introduced by other methods (Mortensen et al., 2010). In our experience, least-squares fitting with a 2D Gaussian function yields the best results for bright probes (Yildiz et al., 2003), while a specially designed Gaussian mask algorithm is more suitable for dim probes (DeWitt et al., 2012; Mortensen et al., 2010). The accuracy of particle tracking is limited by several noise factors. Statistical noise in photon counting (shot noise) is a fundamental limitation. In a photon shot noise-limiting case, the precision of Gaussian center localization, or the standard error of the mean, is equal to $\sigma/\sqrt{N}$, where σ is the standard deviation of a Gaussian (approximately one half of the PSF width, ~100 nm) and N is the total number of detected photon per image (Bobroff, 1986). Using this equation, ~10^4 photons need to be detected to achieve 1 nm precision.

In most cases, the actual noise of the experiment is higher than the photon-shot noise. Background fluorescence caused by the excitation light is discussed above. The choice of camera for TIRF imaging is also critical to reduce detection-related noise, such as camera pixelation and readout noise. The ideal pixel size of the magnified image should be between 80 – 150 nm (Thompson et al., 2002), depending on the SNR. The readout noise of the camera can be reduced by amplifying the signal before readout. The most common amplification technique is electron multiplication (EM), wherein the photon signal (photoelectric current) is amplified prior to digital readout. EM-CCD (EM charged coupled device) cameras almost completely eliminate camera readout noise without creating artifacts in the pixelated image. However, EM is a random process which multiplies the photon shot noise by ~$\sqrt{2}$ along with true signal. As a result, EM is ideal for low (<6) SNR imaging, but reduces the precision in particle tracking at high SNR. Newly-developed scientific CMOS cameras are promising, because they have a very low readout noise and hence do not require amplification. However, the most advanced front-illuminated (where the amplification electronics lie in front of the photo-detection surface, reflecting some of the incident light) CMOS chips have 70% photon detection efficiency, which is low compared to 92% of the back-illuminated (where the electronics are behind the photo-detection surface) EM-CCDs in the market. Furthermore, pixel-to-pixel variation in detection efficiency and digitization creates artifacts in CMOS images, which are particularly problematic for two-color tracking experiments (see below). The anticipated development of back-illuminated CMOS cameras may overcome some of these difficulties.

1.4 Tracking Fluorescently Labeled Molecular Motors *in vitro*

Motor proteins are well suited to single-molecule tracking, because they walk along polymer tracks, such as microtubules and actin, which can be readily fixed to glass surfaces. High-resolution tracking of motors requires that two conditions be met: Motors must be spatially isolated from one another on a filament, and labeled with a bright probe to estimate the center of an isolated spot (Fig. 1.1, 1.2). Single molecule assays reveal the motile properties of processive motors, such as speed, run length and directionality (Vale et al., 1985). For non-processive motors, filament-gliding assays, in which the motors are immobilized on a coverslip and fluorescent tracks glide on motor-coated surfaces (Toyoshima et al., 1990), are more suitable.

1.4.1 Choosing the Right Fluorophore for the Tracking Application

The choice of fluorescent probe is critical for tracking time and precision and dye photostability in solution must be optimized to achieve high precision (Fig. 10.2). For tracking *in*

vivo, where labeling may be difficult, genetically encoded fluorescent proteins (FPs) such as green fluorescent protein (GFP) can be used, but they are not bright or photostable enough to accurately resolve individual steps taken by motors, unless the target can be labeled with >10 FPs (Kural et al., 2005). Most *in vitro* studies use organic dyes, because they have higher photo-stability compared to FPs. These dyes are small in size, available in many colors and can be readily and irreversibly linked to a multitude of biological targets. The three primary pathways of dye photo-bleaching (irreversible loss of fluorescence under intense illumination) are photo-oxidation by singlet oxygen species, triplet excited state formation and charge-separated states by electron transfer reactions (Vogelsang et al., 2008). Several enzymatic approaches have been used to scavenge free oxygen from solution. Glucose oxidase and catalase have been commonly used, but this method produces peroxides that slowly acidify the solution (Tokunaga et al., 1997). The mixture of PCA/PCD (protocatechuic acid/protocatechuate-3,4-dioxygenase) system yields superior results without affecting pH, and has been used more widely in recent years (Aitken et al., 2008). Anti-blinking reagents such as Trolox and β-mercaptoethanol (BME) have been used to prevent triplet state arrest of dyes (Rasnik et al., 2006). The best performing organic dyes, such as tetramethylrhodamine (TMR) and cyanine-3 (Cy3), have been successfully used for tracking the stepping of cytoskeletal motors (Okten et al., 2004; Reck-Peterson et al., 2006; Yildiz et al., 2003). Single fluorophores were tracked with 1 nm precision for more than a minute. Red-shifted dyes such as Cy5 suffer from poor photostability, making the selection of a second color difficult (Rasnik et al., 2006). Alexa and Atto dyes may offer improved photostability at these wavelengths (Qiu et al., 2012). Alternatively, newly developed triplet-state quencher conjugates significantly improve the photostability of Cy5 (Altman et al., 2012), which may allow minutes-long tracking of Cy5, comparable to Cy3.

Quantum dot (QD) nanocrystals offer unprecedented photostability and brightness, allowing tracking at nanometer accuracy for several minutes without photobleaching (Lacoste et al., 2000) (Fig. 1.2). QDs have been used to track kinesin, myosin and dynein motors, providing detailed information about the step size and kinetics at very high temporal resolution (up to 500 images per second). Unfortunately, commercially available QDs are large (~15-20 nm diameter), which can hinder the dynamics of many motor proteins, especially when two QDs are used. Several groups have developed smaller QDs for *in vivo* labeling (Howarth et al., 2008; Smith and Nie, 2008), but reduction in the thickness of the multilayer polymer coat around the semiconductor core of a QD reduces their solubility and photostability over extended periods of time. In addition QDs "blink" on and off frequently. Blinking can be reduced by addition of thiols such as BME (Hohng and Ha, 2004). QDs are multivalent, making crosslinking of different motor proteins a possibility. This can be limited by using a large molar excess of dots, or attaching QDs to motors that are already immobilized on tracks. QD labeling is often poor, with ~20% or less of motors are labeled when using ~10-100 molar excess of QDs. In future, small multicolor dots with controllable valency for both one- and two-color studies must be developed specifically for use in *in vitro* motility assays.

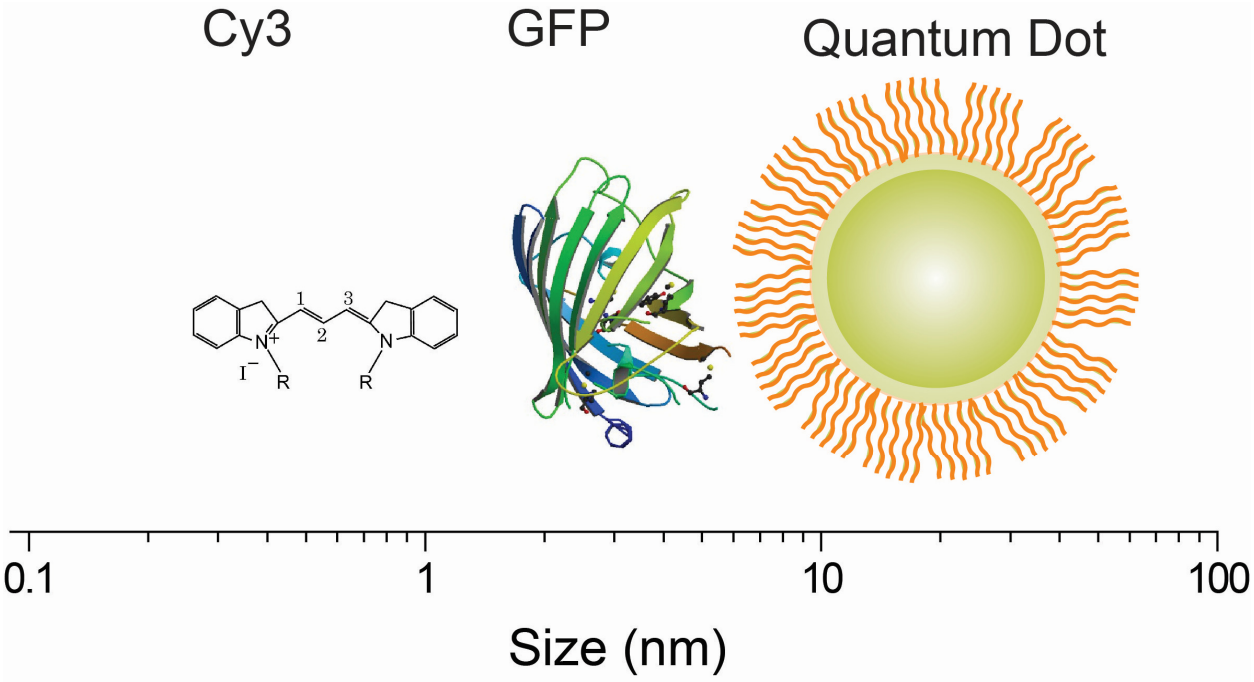


Figure. 1.2 Fluorescence tracking of molecular motors. Schematic of typical *in vitro* single-molecule motility assay. Cytoskeletal tracks are immobilized on a glass coverslip. Fluorescently-labeled motors are flown into the sample chamber. Excitation light is total internally reflected at the glass water boundary of a coverslip. Evanescent field created by the TIR excitation decays exponentially with 100 nm decays constant. Therefore, fluorescently-labeled motors bound to cytoskeletal filaments are selectively excited, in the presence of diffusing motors in the chamber, **(b)** Image of individual fluorophores are diffraction limited and generate PSFs, **(c)** Three dimensional representation of a camera image shows that individual PSFs can be approximated by a two-dimensional Gaussian. While the width of the Gaussian is large (~300 nm), its center can be tracked with nanometer precision if a sufficient number of photons per image is collected

1.4.2 Preparing motors proteins for in vitro tracking experiments.

To prepare fluorescently-labeled motor proteins, standard heterologous expression and purification techniques are commonly used. Different strategies can be used to label cytoskeletal motors. In kinesin, native solvent-accessible cysteines are removed with site-directed mutagenesis, and the fluorophore is attached directly using maleimide or similar chemistry (Rice et al., 1999). A unique cysteine can be labeled with biotin, allowing attachment of a streptavidin-coated QD. In myosin, most studies labeled the calmodulin accessory proteins that coat the heavy chain lever arm first, and then exchanged them onto the motor complex (Irving et al., 1995). In cytoplasmic dynein, specially engineered genetic tags (such as SNAPTag from Promega Inc. and HaloTag from New England Biolabs) were fused to the N- or C-terminus and protein was labeled with ligands bearing fluorescent head groups (such as SNAP-TMR or HaloTag-rhodamine) (Reck-Peterson et al., 2006). To attach QDs or other large probes, streptavidin-coated QDs (Warshaw et al., 2005), or QDs coated with a ligand that attaches directly to a genetic tag have been used (DeWitt et al., 2012)

1.4.3 Sample Preparation

Cleaning of glass coverslips is necessary to reduce background fluorescence from dirt on glass surface. Organic substrates can be effectively cleaned using Piranha etch (a mixture of sulfuric acid and hydrogen peroxide). However, Piranha solutions are extremely corrosive, and routine use is not recommended. Routine cleaning can be done using a combination of 1M KOH and water washes followed by oxidative cleaning, using plasma cleaner or a similar device.
Once motor proteins are labeled with a suitable probe, the sample is prepared by immobilizing tracks on glass. Large bundles of filaments such as sea urchin axonemes can be nonspecifically adsorbed to a glass surface. Individual cytoskeletal filaments, such as actin and microtubules, can be immobilized by biotin-streptavidin linkage. In these assays, unlabeled tubulin (or actin monomers) are mixed with 5-10% biotinylated tubulin in polymerization reaction. Glass surface is treated with 1 mg/ml biotynilated bovine serum albumin (BSA) and then with 0.2 mg/ml streptavidin. Biotinylated filaments attach tightly to the streptavidin-coated surface. After filament immobilization, the glass surface is passivated with 1-2 mg/ml BSA or casein to prevent nonspecific adsorption of motors to the glass surface. If BSA or casein passivation is not sufficient, the glass surface can be passivated with a mixture of polyethylene glycol (PEG) and PEG-biotin before track immobilization. After the track is stably bound to a surface, a dilute (~1 nM) solution of labeled motor proteins are added to the flow chamber, and washed several times with assay buffer, leaving only motors immobilized along the tracks. Stepping movement is induced by addition of ATP. In addition to ATP, oxygen scavengers, triplet state quenchers and anti-blinking reagents (see above) are commonly added to final imaging buffer to improve fluorophore performance.

1.4.4 Imaging and Image analysis

The sample is typically excited under TIR illumination and the fluorescent signal of labeled-motors is detected with an EM-CCD camera. Selection of proper image acquisition parameters is important to obtain the best quality data for a given application. The frame transfer mode of a CCD is used to prevent inter-frame dead time and optimize light detection. For most EM-CCD cameras, the EM gain and pre-amplifier gain should be set according to manufacturer specifications. Magnification of the microscope detection path is adjusted to obtain 85-150 nm camera pixel size.

Depending on the stepping rate of the motor, frame rate and laser power should be optimized to resolve individual steps. A general rule of thumb is that on average 10 frames should elapse for each step the motor takes. For example, yeast cytoplasmic dynein takes 10 steps per second at saturating ATP (Reck-Peterson et al., 2006), and hence ~100 frames per second acquisition is necessary to detect ~90% of the steps. Once a target frame rate is selected, the illuminating laser intensity should be adjusted to offer the best trade-off between the resulting fluorescent spot intensity and photobleaching. To achieve 1.5 nm localization, the laser intensity should be adjusted to collect 10,000 photons per frame from a single molecule (Yildiz et al., 2003). For tracking of small-molecule dyes such as TMR and Cy3, illumination with 10-50 mW of laser intensity is sufficient to track a motor for ~1 minute at 2 frames per second (Yildiz et al., 2003). For tracking of bright QD probes, tracking with acquisition rates as high as 500 frames per second have been reported (DeWitt et al., 2012). Rather than increasing the frame rate and laser intensity, the amount of ATP can be reduced to slow the motor stepping rate for *in vitro* applications. Data

acquisition at saturating ATP is often difficult, because motors take 10-250 steps per second. Tracking these motors at full speed requires more than 1,000 Hz acquisition rate to observe individual steps, which can be achieved by the dark-field tracking methods (Sect. 1.6).

Videos of moving fluorescent spots are processed into traces using single-particle tracking algorithms discussed above. These algorithms find or are given a starting location of a spot to begin tracking, localize the spot center and continue to track the spot until it photobleaches or the video ends. The output of the tracking algorithm is a trace of motor x-y position in time (Fig. 10.3).

1.4.5 Analysis of traces

Analysis of the traces of single motors gives insight into their mechanism and dynamics. Motors "step" in a stochastic fashion and a plot of motor position versus time has a "staircase" appearance. The two parameters of interest from step fitting are the step size of the labeled site, and the "dwell time" between individual steps (Fig. 1.3). If the motor takes a constant step size, such as kinesin-1, we recommend using a model-free pairwise method to determine the average step size (Svoboda et al., 1993). In order to discern individual steps, fluorescent traces must be fit with a staircase function (Fig. 1.3b). Selection of a step-fitting method is important for accurate fitting. Several fitting algorithms are available to automatically detect steps and minimize user bias. T-tests can be employed to estimate when the steps occur (Moffitt et al., 2009), or more detailed statistical analyses such as Hidden Markov Models to compare alternate models for stepping (Müllner et al., 2010). Least-squares fitting of staircases with a user-specified number steps (Kerssemakers et al., 2006) fits steps well, but are biased toward the user's estimation of the number of steps. The appropriate number of steps can be estimated using the Schwartz Information Criterion (Kalafut and Visscher, 2008), thus eliminating the main source of bias. Importantly, even with the best step fitting methods, it is essential to verify all steps by eye. Issues with step finding are a major source of systematic error in tracking experiments. If the average number of data points between adjacent steps is less than 10, or the standard deviation of spot localization is higher than 25% of the step size, a significant portion of steps will be missed, skewing the data towards high step sizes and long dwell times. Step fitters assume constant uncorrelated Gaussian noise, while in practice traces may have correlative or time-dependent noise.

The resulting step size and dwell time data from many individual traces are binned into histograms and further analyzed to infer key structure-function relationships. Step size histograms reveal the average step size, its standard deviation and presence of additional stepping modes, as well as the percentage of backward steps. By comparing the step size and dwell time histograms of fluorophores attached at different sites on the motor, the mechanism of a motor can be inferred (Sect. 10.4). The distribution of dwell times can give insight into the number of rate limiting steps in the mechanochemical cycle. If an observed step of a motor is limited by a single step, such as ATP binding at low ATP concentrations, the dwell time histogram fits well to a single exponential decay. If there is more than one identical rate limiting step, such as multiple ATP hydrolysis events, the histogram fits well to a gamma distribution (Yildiz et al., 2003). The order of the gamma distribution reveals the number of rate limiting steps. The number of rate limiting steps can also be deduced directly from the traces by calculating the randomness parameter, which is defined as the ratio of the squared mean of dwell times over the variance of the dwell times (Schnitzer and Block, 1995).

1.5 Applications of Single-Color Tracking of Molecular Motors *in vitro*

Fluorescence tracking has been used in a variety of contexts to gain insight into the stepping mechanism of molecular motors. High-resolution fluorescence tracking was first developed to study myosin V (Yildiz et al., 2003) and kinesin-1(Yildiz et al., 2004a). A primary goal of these studies is to use step size and step timing at different label locations to determine how the heads of a molecular motor communicate to achieve processive motion. For example, Yildiz *et al.* (Yildiz et al., 2004a) used single-color tracking measurements to determine whether kinesin walks via a "hand-over-hand" or "inchworm" mechanism (Fig. 10.3a). From previous studies, it was already known that kinesin takes 8 nm steps along a microtubule filament (Svoboda et al., 1993). If kinesin steps in a "hand-over-hand" manner, the heads alternate taking 16 nm steps to generate 8 nm center-of-mass steps. Alternately, if kinesin steps in an "inchworm" manner (Hua et al., 2002), the heads do not alternate, and each takes an 8 nm step at every cycle. Kinesin was labeled with a single Cy3 on the motor domain, and the step size and dwell time were measured using Gaussian

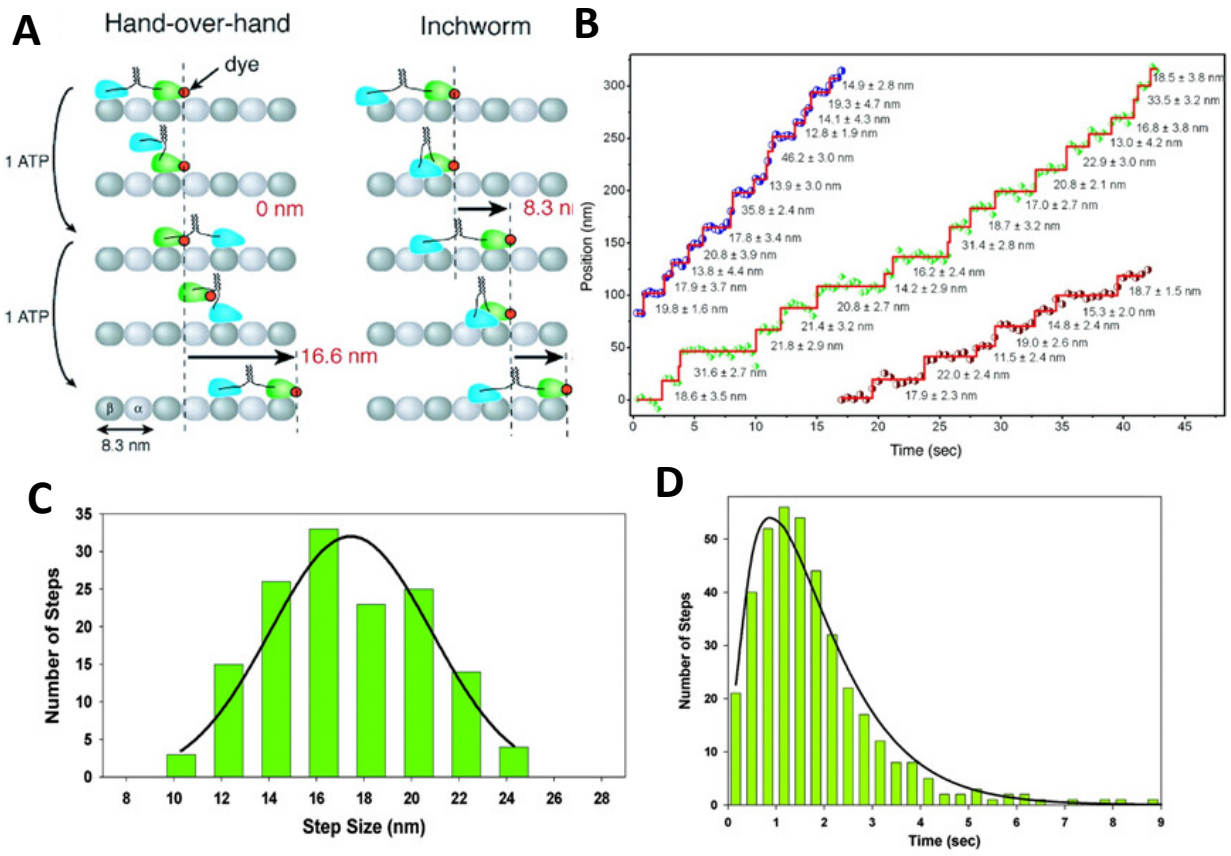


Figure. 1.3 Using single-color fluorescence tracking (FIONA) to determine the stepping mechanism of kinesin. **(a)** Models for processive stepping of kinesin. In the hand-over-hand mechanism, the two identical heads step past each other in an alternating manner, each taking a 16 nm step, then waiting for the other head to step. In the inchworm mechanism, the two heads step 8 nm simultaneously. One head always leads, and the other follows. **(b)** Using FIONA, stepping movement of a kinesin head is determined by fitting the traces to a "staircase" function. **(c)** The step size was ~16 nm on average. **(d)** The dwell time distribution was consistent with a two-step process for a given head's step. These data clearly show that kinesin steps through a hand-over-hand and not an inchworm mechanism. Figure is reprinted from (Yildiz et al., 2004a).

tracking, to ~±2 nm resolution at 500 msec frame time, at limiting ATP (340 nM, Fig. 10.3b). By

comparing the step size of motors labeled at different locations, it was found that the step size of one head was exactly twice that of the tail (16 nm vs. 8 nm, Fig 10. 3c and 3d). The dwell time distribution of motors labeled at the head fit well to a Gamma distribution with a two-step process. In contrast, the dwell time distribution of motors labeled at the tail fit well to a single exponential decay. These data showed that the heads of a kinesin dimer take twice the center-of-mass step at every other step of a motor. Therefore, these studies conclusively showed that the heads of kinesin alternately take steps in a "hand-over-hand" manner and not in an "inchworm" manner (Asbury et al., 2003; Kaseda et al., 2003) (Fig. 1.3), similar to myosin V (Forkey et al., 2003; Yildiz et al., 2003) and VI (Okten et al., 2004; Yildiz et al., 2004b).

Similar approaches have been used to answer a variety of questions about the stepping mechanism. Tracking studies on kinesin mutants with extended polypeptide linkers showed that loosening the mechanical connection between heads of a kinesin dimer reduced the apparent amount of head-head coordination (Yildiz et al., 2008). The step size of these loosely connected kinesin heads was highly variable, more closely resembling the results from a similar tracking study of yeast cytoplasmic dynein (Reck-Peterson et al., 2006). Subsequent tracking studies on yeast dynein at high time resolution showed that the heads likely do not alternate either, indicating that cytoplasmic dynein likely steps via a unique uncoordinated mechanism (DeWitt et al., 2012). It is possible that these loosely connected kinesin dimers achieve robust processivity with a similar lack of coordination. Comparable studies on mammalian dynein did not show high variability in step size (Toba et al., 2006). Tracking has also been used to determine the complex mixed hand-over-hand-inchworm mechanism of myosin VI stepping (Nishikawa et al., 2010).

1.6 Two-Color Fluorescence Tracking: Theory and Practice

If two different colors of fluorescent label are used to track a single motor, entirely new dimensions of analysis become accessible. Simultaneous tracking of two fluorophores allows measurement of dwell time and step size at two distinct locations, allowing more definitive characterization of the mechanism of a dimeric motor. Using two-color mapping techniques, the relative location of the two fluorophores in space can be determined with 3-5 nm accuracy (Churchman et al., 2005). This allows simultaneous tracking and distance measurement, analogous to single-molecule fluorescence resonance energy transfer (FRET) (Ha et al., 1996) but for larger distances (>10 nm for mapping vs. <10 nm for FRET). Two-color experiments yield exceptionally rich information, but they are more challenging than one-color experiments.

1.6.1 Selection of Probes

Additional care must be taken in selection of probes for a two-color assay than for a one-color assay. Both probes must be spectrally distinct so as not to cause bleedthrough between fluorescent channels. Because two-color measurement is impossible when one of the probes photobleaches, both probes must be exceptionally photo-stable. Very few small-molecule probe pairs meet these requirements (Churchman et al., 2005; Qiu et al., 2012). For the highest resolution imaging, investigators have primarily used QD probes (DeWitt et al., 2012; Ikezaki et al., 2012; Nishikawa et al., 2010; Warshaw et al., 2005), however the large size of commercial QDs renders measurement of short distances (<15 nm) difficult.

1.6.2 Two-color labeling and protein preparation

Two-color tracking requires attachment of two spectrally distinct probes at two distinct sites on a motor protein. Many processive motors are homodimeric, and one can randomly label these sites with a mixture of differently-colored probes, and limit analysis to two-color dual-labeled motors. Where two chemically distinct sites are needed, the multimeric nature of processive motors can be used to engineer artificial heterodimers, allowing specific labeling of monomers and subsequent dimerization. For example, to label heterodimeric dynein motors, In Chapters 2, 3, and 4 I utilized monomeric forms of cytoplasmic dynein fused with a HaloTag at the motor domain (DeWitt et al., 2012). One of the monomers is labeled with biotinylated HaloTag ligand, while the other was left unlabeled. After the heterodimerization of the monomers, two distinct sites were labeled with a mixture of streptavidin-coated and HaloTag-coated QDs. A number of enzyme-directed tags have been developed that ligate probes to small moieties within proteins (Fernández-Suárez et al., 2007; Howarth et al., 2005; Kaiser et al., 2011), but these labeling strategies have not yet been applied to fluorescent tracking studies of motor proteins.

1.6.3 Two-Color Fluorescence Imaging

The microscope setup employed is identical to that used for one-color imaging above, with a few modifications. For different emission but similar excitation spectra (e.g. QDs), both probes can be excited with a single laser beam. For probes with different excitation spectra, two laser beams must be aligned together for excitation (e.g. a 532 laser for Cy3 imaging, and a 633 laser for Cy5 imaging). In fluorescence detection, the goal is to image the two probes with perfect separation of their signal, either in space or in time. For separation of imaging in time, two laser beams can be alternately turned on and off to excite only one type of fluorophore at a time (Qiu et al., 2012), and images can be collected with a single CCD camera. For separation of imaging in space, both fluorophores are excited at the same time and the signal of the fluorophores is separated onto two different detection channels (Churchman et al., 2005) using a set of dichroic and emission filters (Fig 1.4a). Splitting the fluorescence in space allows high-speed acquisition with QD probes over a full CCD surface, while splitting in time may make sub-pixel map construction more reliable. For multichannel detection, I recommend EM-CCD cameras over sCMOS cameras, because currently-available sCMOS cameras have significant variation in pixel sensitivity, making map construction difficult. In either case, the output of the experiment will be two sets of images, one for each color.

1.6.4 Construction of sub-pixel maps

To simultaneously track two fluorophores at distinct locations on a walking motor and measure the distance between them, the relative positions of the fluorophores must be registered with nanometer accuracy. For image registration, the sample is decorated with fiducial markers that appear in both channels. To map the CCD surface, fiducials are localized in both fluorescent channels to generate a set of colocalizations (Churchman et al., 2005). Coordinates of colocalized spots are fitted using non-linear regression with Taylor polynomials to make a subpixel map from these colocalizations.

Image registration corrects for several distortions and optical aberrations between the channels. There are three primary contributing factors to the mapping accuracy: First, the channels

may differ in terms of actual position, rotation and magnification. These types of errors can be easily fixed by polynomial fits of the fiducial markers. Second, optical aberrations (spherical, astigmatism) slightly distort one channel image relative to the other. These aberrations, while substantial, can also be modeled using polynomial regression of relatively limited number of points. Remarkably, using the subpixel map generated by one set of fiducials fails to fully register another set of fiducial markers, emitting at a slightly different wavelength. Ideally the same set of fluorophores should be used as fiducials to correct for chromatic aberrations. Third, the CCD surface often bears slight pixel-to-pixel imperfections (Pertsinidis et al., 2010). This error can be only be corrected by collecting multiple colocalizations per pixel and/or separately registering small parts of the CCD surface. Using active feedback of a nanopositioning stage, the Chu group achieved mapping accuracies of ~1 nm (Pertsinidis et al., 2010) in a small part of a CCD chip. Alternatively, mapping can be bypassed entirely using confocal imaging and multicolor QDs (Agrawal et al., 2008; Antelman et al., 2009). The key principle is that differently colored QDs have similar excitation spectra, allowing simultaneous excitation and multicolor detection. This approach is appealing, as nanoscale mapping procedures are not required. However, the time resolution of scanning confocal microscopy limits its application in dynamic systems, such as tracking of molecular motors.

It is also important to calibrate the mapping accuracy by measuring short end-to-end distances (e.g. short DNA oligonucleotides at different lengths) using the same set of fluorophores (Churchman et al., 2005; DeWitt et al., 2012). The mapping and localization errors lead to systematic overestimation of the measured distance, which can be corrected for two fluorophores that remain at a fixed distance. However, calibration of measured distances is problematic when the distance between the fluorophores fluctuates stochastically, as is the case for motor proteins and other dynamic systems. Therefore, mapping and localization error must be kept significantly lower than the required resolution of the experiment.

1.6.5 Methods for generation of sub-pixel maps

Exact approaches to generate a map vary. We will describe the approach used in our laboratory in more detail. In a two-color study of dynein using QD probes, DeWitt *et al.* (DeWitt et al., 2012) constructed maps of the entire CCD surface using two rounds of image registration (Fig. 1.4). First, a subpixel map was generated using an array of diffraction-limited nanoholes (Fig. 1.4b) (W. J. Moberly Chan et al., 2007). The 25x25 array of nanoholes was formed in a 150 nm thick gold layer deposited on a glass slide by sputter deposition. A 12.5 nm thick titanium layer served to enhance the adhesion of the gold film to the glass surface. Holes were formed by focused ion beam drilling using the 30 keV gallium ion beam. The hole diameter was 180 nm and the hole spacing was ~2 μm (Fig. 1.4b).

The sample was illuminated under bright-field and moved at random intervals and directions across the surface. Each nanohole produces a diffraction-limited spot in both fluorescent channels (Fig 1.4c). These spots were localized to ~1 nm accuracy, and paired to create a list of >1,000,000 colocalizations. The subpixel map created from these colocalizations can achieve image registration with ~3 nm accuracy. To correct for chromatic aberrations, it was necessary to generate a smaller set of colocalizations using custom-made fluorescent fiducial markers. For the QD585-QD655 pair used in the study, the fiducial was an amino-polymer QD655 coated with Rhodamine Red X, whose spectrum is nearly identical to the QD585. A second corrective map of the entire CCD chip was able to map pairs of QDs with 3-5 nm accuracy (DeWitt et al., 2012).

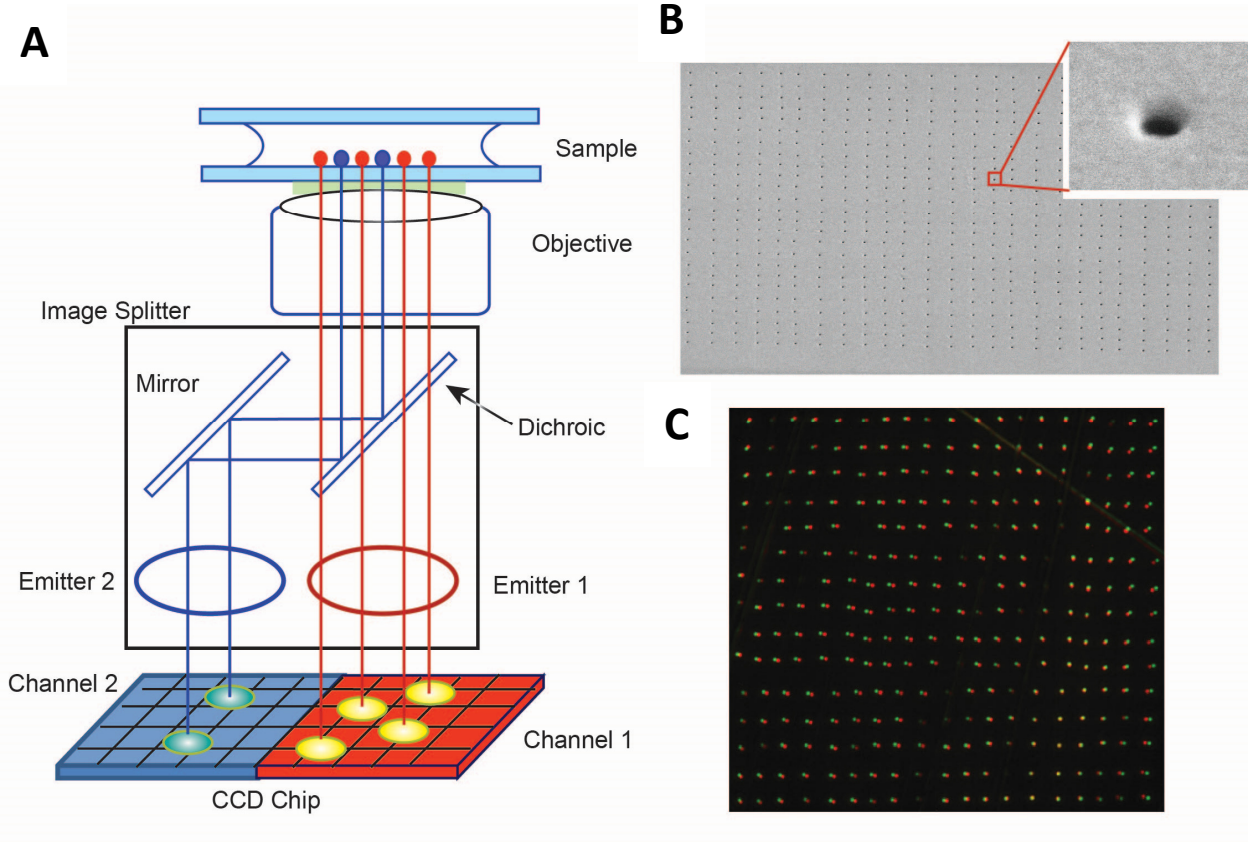


Figure. 1.4 Multicolor Fluorescent Tracking and Image Registration. **(a)** Fluorescence emission of different-colored probes is splitted to different detection channels on a CCD chip, using a set of dichroic mirrors and emission filters in the detection path. **(b)** To register the two channels with respect to each other, a gold thin film decorated with 180 nm diameter holes is imaged under bright-field. **(c)** Superimposed images of nanohole pairs show that relative positions of the pairs differ depending on where they are located on the CCD. Image registration requires correction for various sources of image distortion and aberration. Precise mapping requires a secondary map of probes isospectral to the labels used in the motility assay. Finally, corrective maps are applied to the traces to measure relative position of the dye labels

1.6.5 Data Analysis

Once maps are constructed, movies of labeled motors are acquired in an analogous manner to the one-color experiments described above, producing movies of dual-labeled motors. Colocalized fluorophores are tracked using the same algorithms. The stepping trace of one dye is overlaid upon the other using the mapping function created from the set of colocalizations of the fiducials, as described above. The overlaid two-color trace (Fig. 1.5) is then fit to staircase functions as described above.

Two-color traces yield substantially more information than one-color traces (Fig. 1.5). In addition to the simultaneous detection of step size and dwell time of the two labeling sites, these traces reveal the distance between the sites, which site is in the lead and the orientation of the sites relative to the cytoskeletal track. Two color tracking methods were first used to observe the hand-over-hand movement of the two motor domains of myosin V (Churchman et al., 2005; Warshaw

et al., 2005). Yanagida and coworkers showed that myosin VI steps via a combination of hand over hand and inchworm stepping during processive motility (Nishikawa et al., 2010).

The information that can be gleaned from a two-color experiment allows direct observation of the stepping mechanism. The results of a two-color study on myosin V by Warshaw et al are illustrated in Fig. 1.5 (Warshaw et al., 2005). The investigators measured the distance between the two heads at 500 msec time resolution as the motor walked along actin filaments. This allowed direct observation of the hand-over-hand mechanism. The leading head would wait ~37 nm in front of the trailing head until the trailing head stepped over it. This head in turn waits in the lead for the next head, and so on. This experiment demonstrates the power of the two-color technique. In Chapter 2, I will apply this method to the more complex motor cytoplasmic dynein (DeWitt et al., 2012).

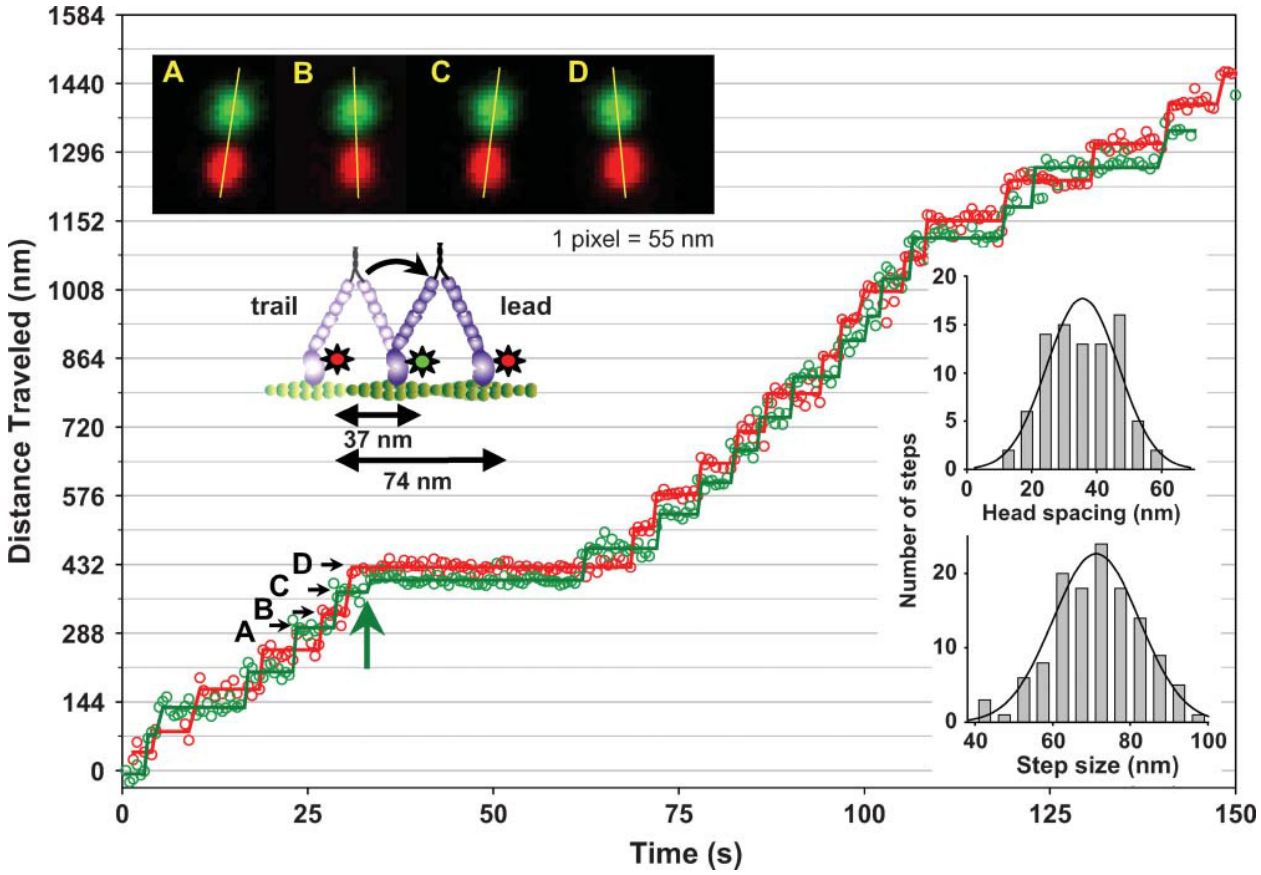


Figure 1.5. Use two-color tracking to directly observe the stepping mechanism of myosin V. Myosin V was labeled with a QD585-QD655 pair. Simultaneous tracking of the two heads not only resolves their stepping motion, but also provides information about their relative orientation during motility. The subpixel trace of a dual-labeled myosin V shows that the heads almost always step in an alternating fashion. The lead heads waits for the trailing head to step. These data unambiguously show that myosin V steps in a coordinated, hand-over-hand manner, in contrast to the more complex, uncoordinated stepping mechanism of cytoplasmic dynein and myosin X (DeWitt et al., 2012; Nishikawa et al., 2010). Figure adapted from (Warshaw et al., 2005).

1.7 Other Tracking Methods for Studying Processive Cytoskeletal Motors

Dark-field microscopy, which detects scattered light from objects with high index of refraction, is a promising tool to track motor proteins (Fig. 10.6). Dark-field tracking (DFT) works by imaging gold nanoparticles under darkfield illumination (Braslavsky et al., 2001). Since the image arises from light scattering and not fluorescence, probe photostability is not a concern, and very high incident light flux can be used. This allows the probe to be localized with arbitrarily high spatiotemporal resolution (~1 nm spatial and ~100 µsec time resolution). DFT can be used to study extremely rapid events at zero applied force, such as the release and re-binding of a motor head during a step (Dunn and Spudich, 2007) or the step size of rapidly moving motors (Dunn et al., 2010). To get sufficient scattering, the gold nanoparticle must be relatively large (>40 nm diameter), and thus DFT is not suitable for applications that require a small probe.

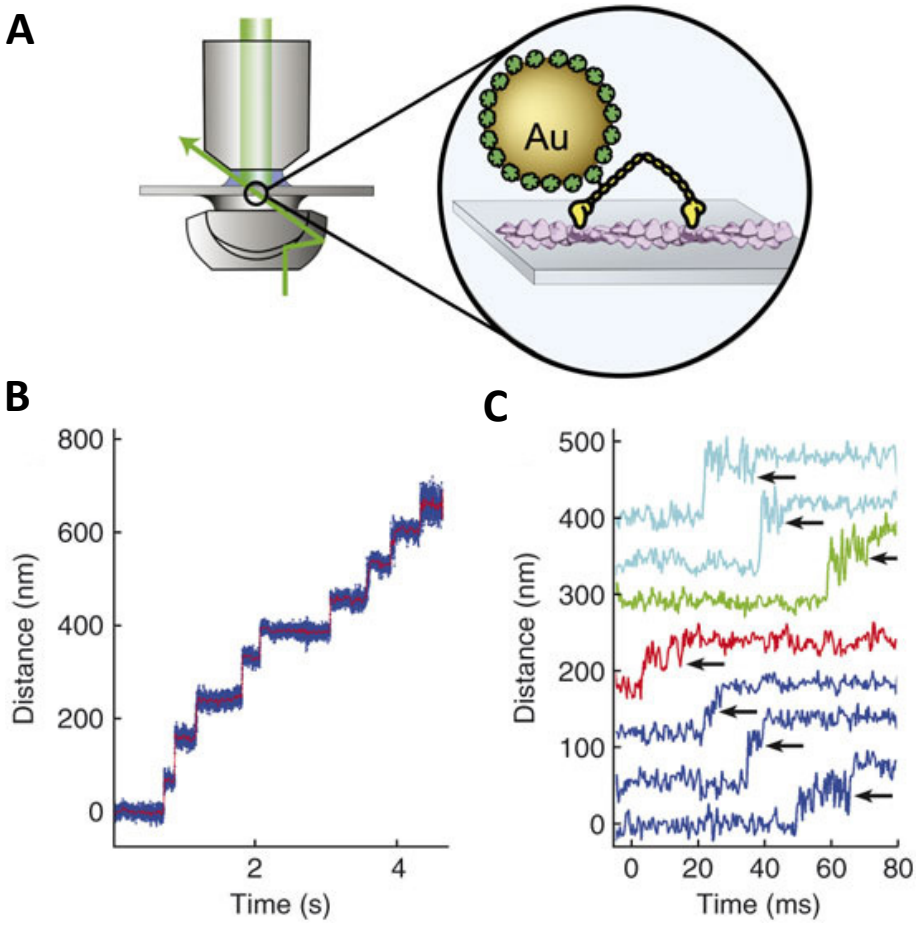


Figure. 1.6 Dark-Field Tracking. **(a)** Step-wise movement of myosin V was tracked by dark-field imaging of ~40 nm gold nanoparticles, which allows extremely fast and accurate position detection with zero applied force. **(b)** Individual steps taken by myosin V were clearly discernible. **(c)** Rapid conformational changes, such as the myosin head fluctuations (arrow heads) were detected between adjacent steps (Reproduced from (Dunn et al., 2010)).

Polarization-based methods provide information about the orientation of the probe attached to a molecular motor (Fig. 1.7). The key principle is that fluorophores have an excitation dipole moment and absorption efficiency of linearly polarized excitation light is given by $\cos^2\varphi$, where φ is the angle between the excitation dipole moment and the photon polarization. Therefore, it is possible to obtain the orientation of the dye from its intensity when illuminated with different polarizations of excitation light (Ha et al., 1998). However, polarization measurements are limited by the high rotational mobility of probes attached through a single linkage. If the rotational correlation time is shorter than the image acquisition rate, the probe acts as an isotropic emitter. This can be circumvented by attaching the dye at two locations, using bi-functional rhodamine (Corrie et al., 1999), or a multivalent QD nanorod (Ohmachi et al., 2012).

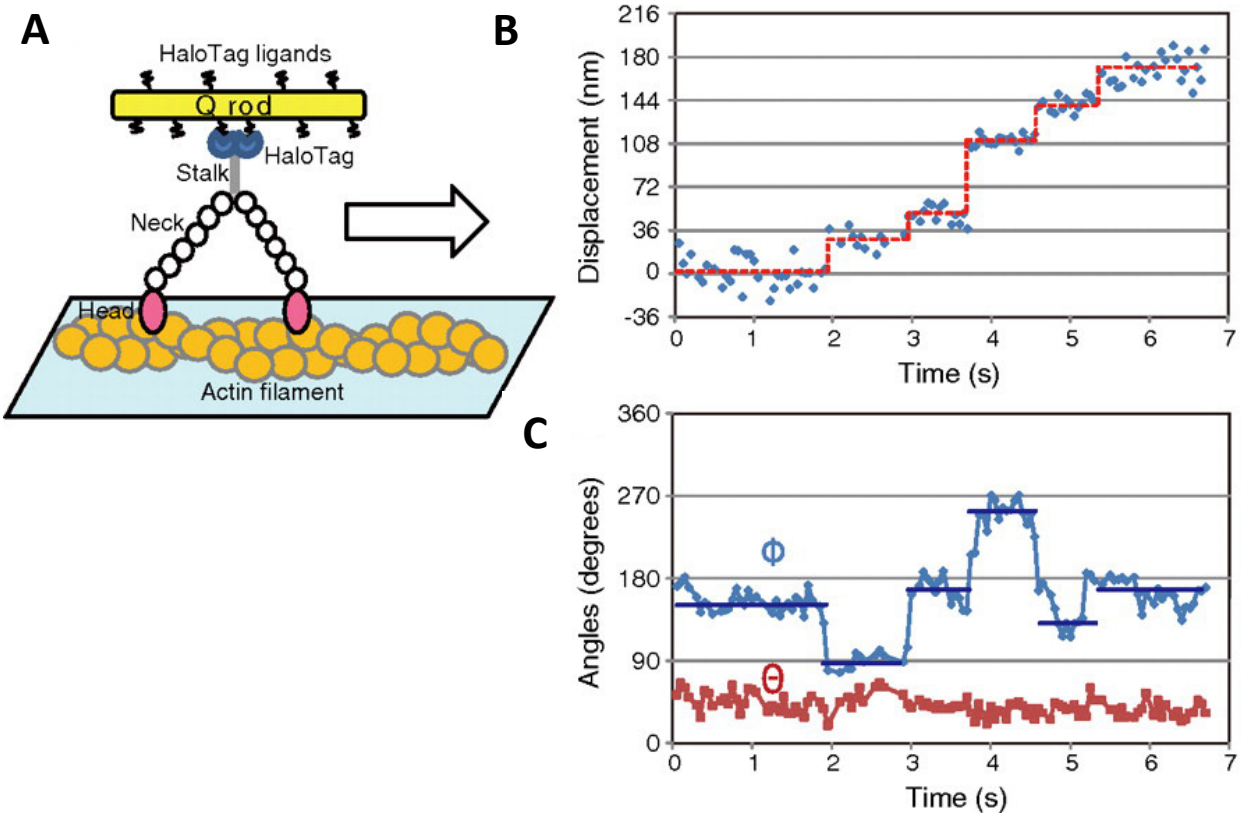


Figure. 1.7 Tracking both the position and orientation of a motor with a nanorod**. (a)** QD nanorods are attached at two locations on myosin V to track rotational and translational steps of the motor. **(b-c)** Simultaneous position **(b)** and orientation **(c)** detection allows measurement of angular changes along with position changes (Reproduced from (Ohmachi et al., 2012)).

In a single molecule fluorescence polarization microscope, the sample is excited with linearly polarized light under TIR illumination and the fluorescence emission is recorded with a single channel. An alternative strategy is to excite the sample with circularly polarized light and split the fluorescence emission into two orthogonal polarizations (Sase et al., 1995). In order to circumvent two fold degeneracy of in plane angles (φ versus $-\varphi$), the sample can be excited with four different polarization angles (0˚, 45˚, 90˚, 135˚) (Sosa et al., 2001).

Goldman and coworkers excited the sample with two orthogonal incident beams in a prism-type TIR to determine the three dimensional orientation of a fluorophore (Syed et al., 2006). The emission pathway was split into two orthogonal channels. By labeling the myosin V lever arm with bi-functional rhodamine, they observed that the myosin V light chain alternates between two well defined orientations as the motor walks, providing evidence that myosin V walks hand over hand (Forkey et al., 2003).

Single molecule high resolution imaging with photobleaching (SHRImP) is an alternative to two-color mapping that can be used to measure distances between two sites of motor protein without the construction of sub-pixel maps (Gordon et al., 2004). SHRImP has been applied to myosin VI labeled with two GFPs, one on each motor head (Fig. 1.8). The fluorescent spot of two GFPs were localized using Gaussian fitting. When one of the GFPs photobleaches, the resulting spot from the remaining GFP is localized. The distance between the centers of the two spots (categorized based on spot intensity) can be used to calculate the original GFP-GFP distance with ~5 nm accuracy (Balci et al., 2005). Further studies showed that the photobleaching based distance measurements are not limited to two sites (Rust et al., 2006) and can potentially be extended to obtain detailed structural information about the motor proteins as they walk along their respective track.

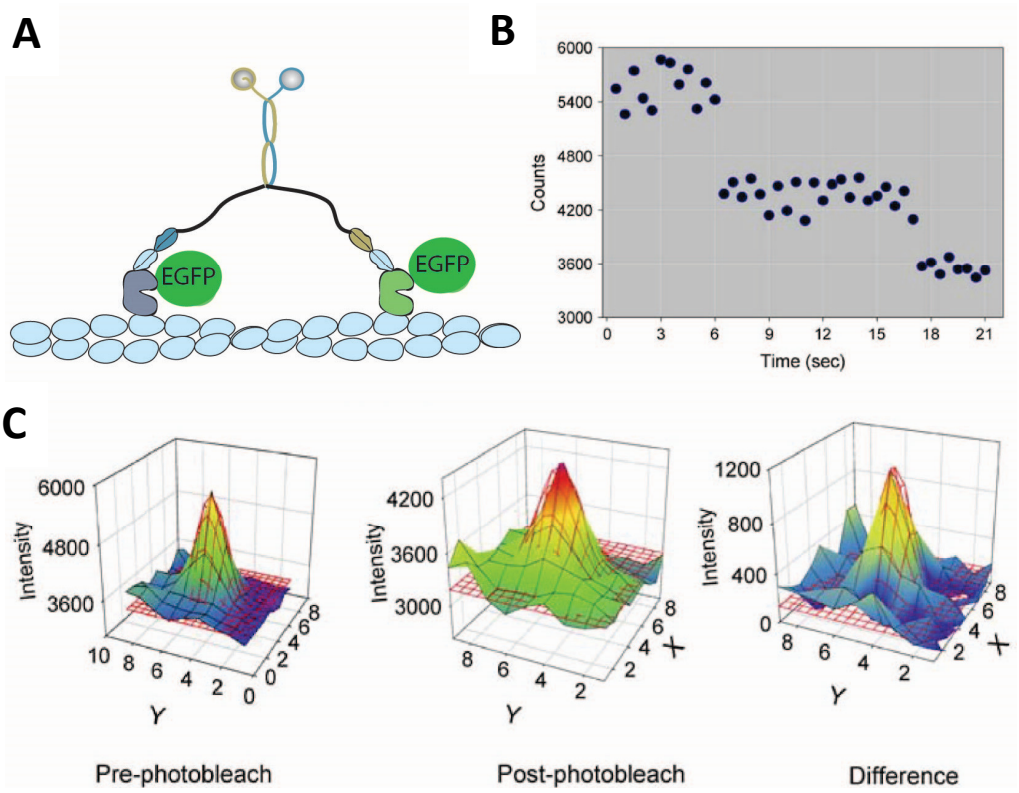


Figure. 1.8 SHRImP to measure head to head distance. **(a)** A myosin VI motor is labeled with an eGFP per head. **(b)** Intensity of a diffraction limited spot disappears in two steps, evidence for the presence of two probes on a motor. **(c)** (Left) PSFs of eGFPs overlap, when they are both fluorescent, (Middle) As one of the eGFPs bleach, the center of the PSF shifts. This reveals the PSF of the remaining fluorescent eGFP, (Right) The PSF of the bleached eGFP can be calculated by subtracting the fluorescent image from each other. Localization of both EGFPs measures the inter-head distance (Adapted from (Balci et al., 2005)).

1.8 Conclusion

Fluorescent tracking is a powerful method for determining the mechanism of motor proteins. Compared to optical trapping methods, high resolution fluorescence tracking methods require no applied force to observe steps and they can track hundreds of motors molecules at a time. Advances in probe technology, commercialization of TIRF microscopes and the latest generation of detectors have made single-molecule tracking *in vitro* accessible to non-specialists. Using these probes, data can be acquired at high time resolution, at multiple sites of attachment. Using two-color tracking methods and the construction of nanoscale CCD maps, the relative movements of different parts of a protein can be followed at every step, yielding data of striking richness for mechanistic analysis. Future improvements in fluorescent probes and detection ability will be required to study more complex systems such as identification and characterization of motor regulatory proteins and protein complexes.

CHAPTER 2: CYTOPLASMIC DYNEIN MOVES THROUGH UNCOORDINATED STEPPING OF THE AAA+ RING DOMAINS

2.1 Summary

Cytoplasmic dynein is a homodimeric AAA+ motor 2.that transports a multitude of cargos towards the microtubule minus end. How the two catalytic head domains interact and move relative to each other during processive movement is unclear. Here, I tracked the relative positions of both heads with nanometer precision and directly observed the heads moving independently along the microtubule. The heads remained widely separated and their stepping behavior varied as a function of interhead separation. One active head was sufficient for processive movement and an active head could drag an inactive partner head forward. Thus, dynein moves processively without interhead coordination, a mechanism fundamentally distinct from the hand-over-hand stepping of kinesin and myosin.

2.2 Introduction

Cytoplasmic dynein forms a 1.2 MDa complex that uses adenosine triphosphate (ATP) hydrolysis to power minus-end directed motility along microtubules. The catalytic head domain is composed of six AAA+ (ATPases associated with diverse cellular activities) modules arranged in a ring (Burgess et al., 2003). ATPase activity at AAA1 is essential for dynein motility (Kon et al., 2004). The two rings are connected by the dimerization of N-terminal tail domains and bind to the microtubule through a ~15 nm coiled-coil stalk bearing a small microtubule-binding domain (MTBD). Dynein is required for many cellular processes, including organelle transport and cell division, and dynein malfunction can lead to motor neuron degeneration (Ori-McKenney et al., 2010).

Despite recent advances in understanding dynein's structure (Carter et al., 2008, 2011; Kon et al., 2011, 2012; Schmidt et al., 2012) and mechanism (Gennerich et al., 2007; Reck-Peterson et al., 2006), the stepping mechanism of dimeric dynein during processive motion remains unclear. Studies of kinesin and myosin motors have shown that their heads take alternating steps in a hand-over-hand (HoH) fashion (Asbury et al., 2003; Yildiz et al., 2003, 2004a). Dynein motility also requires two heads (Reck-Peterson et al., 2006), but it is unclear whether they coordinate with each other to achieve processive motion (Tsygankov et al., 2009). Dynein's structure and origin are distinct from kinesin and myosin, suggesting that it may use a different mechanism.

2.3 Results and Discussion

To investigate dynein's stepping mechanism, I tracked the movement of an artificially dimerized, tail-truncated yeast cytoplasmic dynein (GST-Dyn$_{331kD}$), which has similar stepping properties to native dynein (Reck-Peterson et al., 2006). First, I tracked a dynein labeled with a single quantum dot (QD) at 2 msec temporal resolution in the presence of rate-limiting [ATP] (Figs. 2.1A and 2.2). As reported previously (Mallik et al., 2004; Reck-Peterson et al., 2006), the distribution of step sizes was multimodal. The step size histogram of head-labeled dynein revealed two major peaks at 9.3 ± 0.7 and 17.5 ± 1.2 nm that were nearly two-fold larger than the peaks observed in the tail histogram (4.8 ± 0.3 and 8.7 ± 0.9 nm) (Fig. 2.1B). The probability of

backward stepping (p_{BW}) was 0.2. The dwell time histogram for head-labeled dynein at 12 µM ATP (Fig. 2.1C) was best fit by a convolution of one slow (k_1 = 2.1 ± 0.2 sec^{-1}) and one fast (k_2 = 14.1 ± 2.5 sec^{-1}) exponential rate constant. The product of k_2 and the average head step size (d_{head} = 10.2 nm) agrees well with the average velocity of dynein at saturating [ATP] (124 nm/sec). This data excludes the symmetric HoH model, which predicts the stepping kinetics of a head to be a convolution of two equal rate constants (Fig. 2.2). Instead, the dwell time histogram of tail-labeled dynein was well described by a kinetic model in which the heads can step independently and the tail moves each time either head takes a step (k'_1 = 1.2 ± 0.1 sec^{-1}, k'_2 = 12.2 ± 2.7 sec^{-1}) (Fig. 2.2).

To directly address how the two heads interact and move relative to each other, I labeled GST-Dyn$_{331kD}$ with different-colored QDs (17-22 nm in size) at the C-termini and simultaneously tracked the positions of the heads during processive movement (*11*). The fluorescent signal was split into two channels and registered to 3 nm precision (Fig. 2.3). Representative traces (Fig 2.4A) clearly showed that either head could take a step regardless of which head was leading, a mechanism distinct from HoH. While 68% of the steps showed a canonical alternating pattern, one head could take multiple consecutive (non-alternating) steps before the other head moves (Fig. 2.4B). Non-alternating stepping occurred ~2-fold less frequently than alternating stepping (Fig. 2.5). This may partly be due to the time needed for a head to complete its ATPase cycle before it can take another step. The heads often walked along different protofilaments, with the leading head preferentially located to the right of the trailing head (Fig. 2.4C). Measurements using organic dyes showed that the heads were separated by 23.0 ± 13.2 nm, excluding the possibility of a stacking interaction between the AAA+ rings (Nicastro et al., 2006).

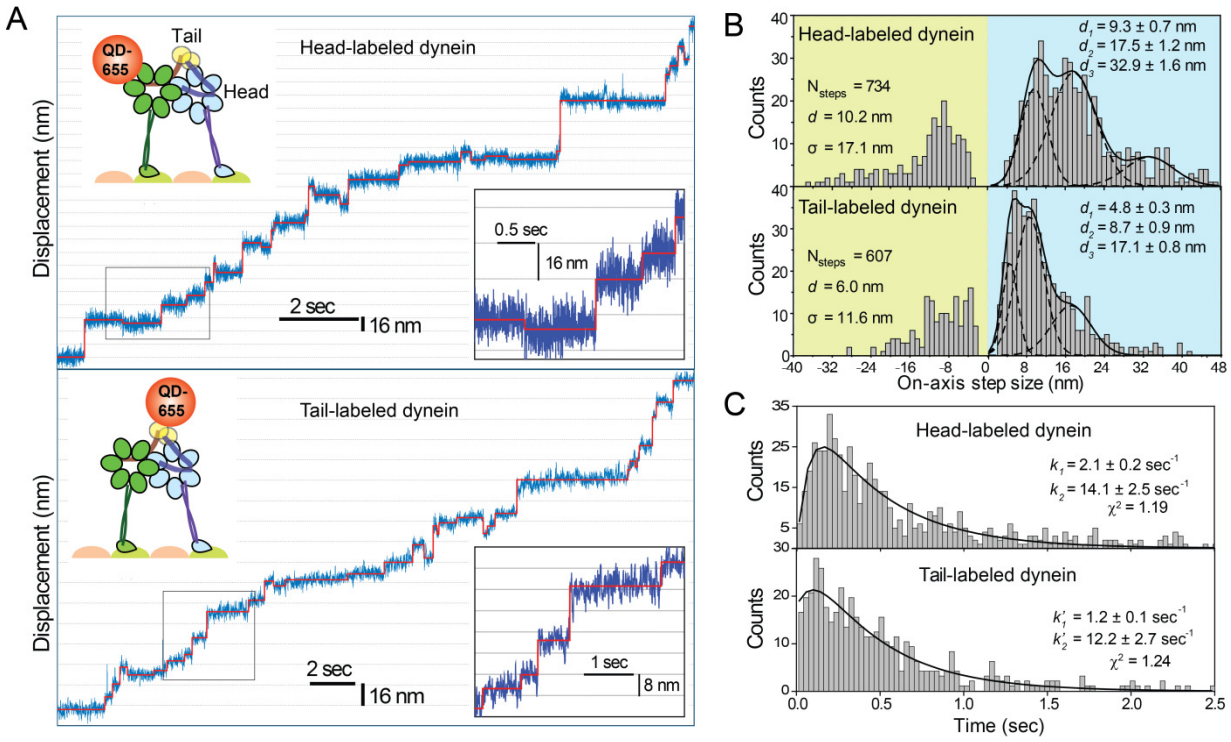


Figure. 2.1. (**A**) Step size measurements of tail- and head-labeled GST-Dyn$_{331kD}$ with a single QD-655 at 2 msec temporal resolution. The QD position (blue traces) was fit by a step-finding algorithm (solid red lines). (**B**) Multiple Gaussian fits to step size histograms reveal two major peaks at 9.3 and 17.5 nm for the head and 4.8 and 8.7 nm for the tail. (**C**) Dwell time histogram of head-stepping fitted to a convolution of two unequal rate constants, and that of tail-stepping fitted to a model assuming uncoordinated stepping between two heads, each with two unequal rate constants.

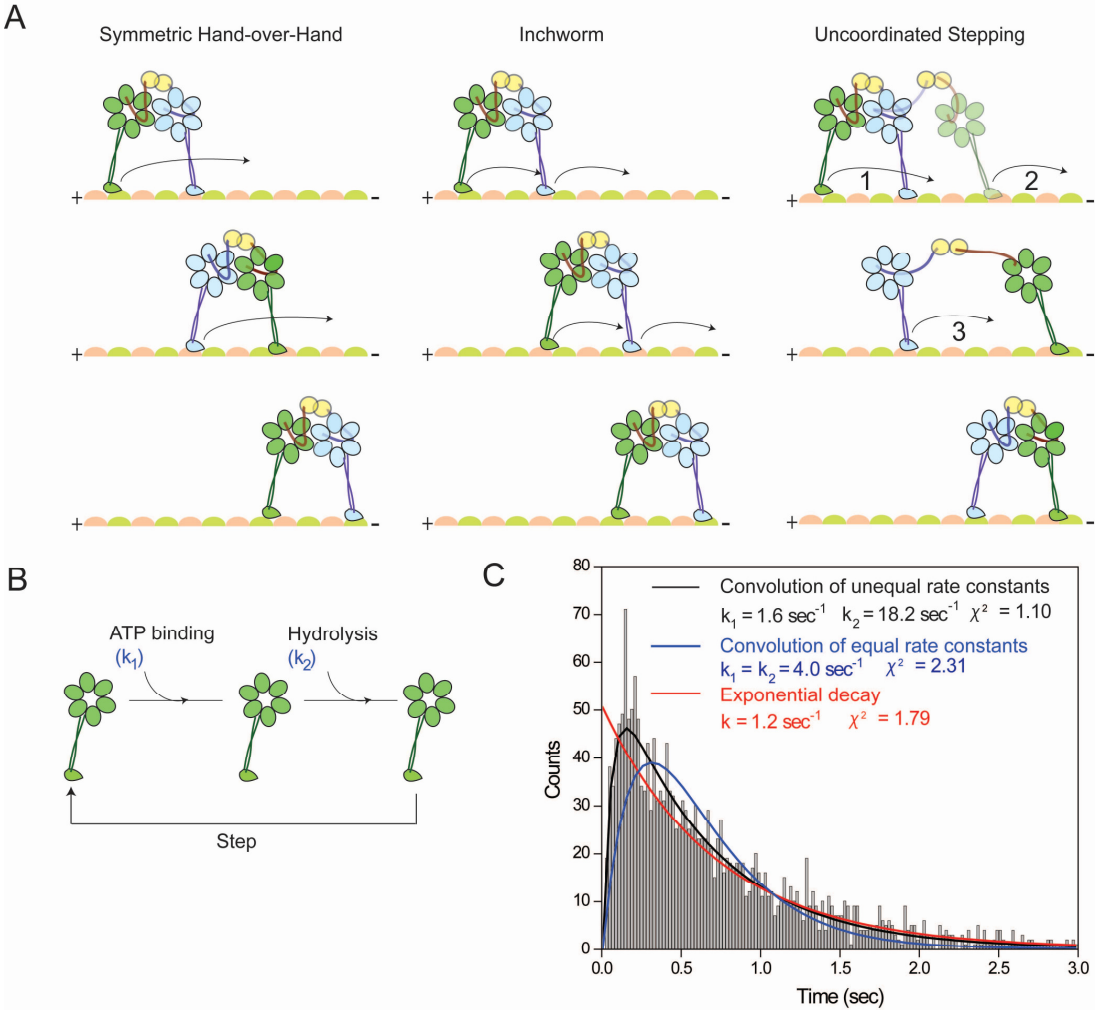


Figure 2.2. **(A)** Possible models for dynein processivity. In a symmetric hand-over-hand model, the two heads (green and blue) alternately take steps and exchange the lead position. Each head moves once for every other step of the motor, and the tail moves half the head step size for every step of the motor. If there is a single rate-limiting constant for a head to take a step, the model predicts the stepping kinetics of an individual head to be a convolution of two equal rate constants. In the inchworm model, both heads move together at every step of the motor and the heads do not exchange leads. The tail step size is equal to that of the head. The model predicts the stepping kinetics of an individual head to be a single exponential decay. In the uncoordinated stepping model, the heads do not strictly follow either of the hand-over-hand or inchworm models. Instead, either head is equally likely to take a step. The tail still moves half the head step size when either of the heads take a step. This model predicts the kinetics of both head and tail stepping to fit to a single exponential decay. **(B)** Dynein stepping requires the binding and hydrolysis of ATP at the catalytic (head) domain. At low (< 10 µM) ATP concentrations, ATP binding becomes rate-limiting. At saturating (> 1 mM) ATP concentrations, the motor will be limited by the ATP turnover rate. If the rates of both of these events are rate-limiting, then the dwell time distribution of a head would be a convolution of two unequal rate constants, assuming that dynein walks inchworm or in an uncoordinated manner. In contrast, if dynein walks hand-over-hand, the dwell time distribution would be best fit by a convolution of two identical heads, each stepping via a convolution of two unequal rate constants. (**C**) A histogram of dwell times between the steps of head-labeled GST-Dyn_{331kD} at 12 µM ATP (N_{dwells} = 1952). Data were fit to a convolution of two unequal exponential rate constants ($y = A*[exp^{-k1t} - exp^{-k2t}]$, black curve), a convolution of two equal exponential rate constants ($y = A*t*exp^{-kt}$, blue curve) and to a single exponential decay ($y = A*exp^{-kt}$, red curve). Out of the three functions, only the convolution of two unequal exponential rate constants produces a good fit ($\chi^2 = 1.10$) to the histogram. The slow rate ($k_1 = 1.59$ sec^{-1}) may correspond to ATP binding and the fast rate ($k_2 = 18.3$ sec^{-1}) may correspond to the ATP turnover rate. k_2 is in close agreement with the previously reported catalytic rate ($k_{cat} = 16.1 \pm 0.3$ ATP/dimer/s) for yeast cytoplasmic dynein, as measured in bulk microtubule-stimulated ATPase assays.

The heads frequently swapped the lead, but not strictly after every step of the motor. The stepping characteristics of a head in the leading and trailing positions differed significantly depending on interhead separation, forming the basis of the high variability in dynein's step size (Reck-Peterson et al., 2006). The on-axis (parallel to the microtubule long axis) step size decreased by ~0.4 nm per nanometer increase in interhead separation (Fig. 2.6A). The trailing head took larger (d = 17.5 nm) forward and fewer (p_{BW} = 0.14) backward steps. In contrast, the leading head took significantly shorter (d = 1.5 nm) forward and more frequent (p_{BW} = 0.45) backward steps. The off-axis (perpendicular to the microtubule long axis) step size also decreased with interhead separation, but without a net bias toward left or right (Fig. 2.6B). The stepping probabilities of the leading and trailing heads were nearly identical when they were positioned close (10-20 nm) to each other. At larger separations, 65% of the steps were taken by the trailing head (Fig. 2.6C).

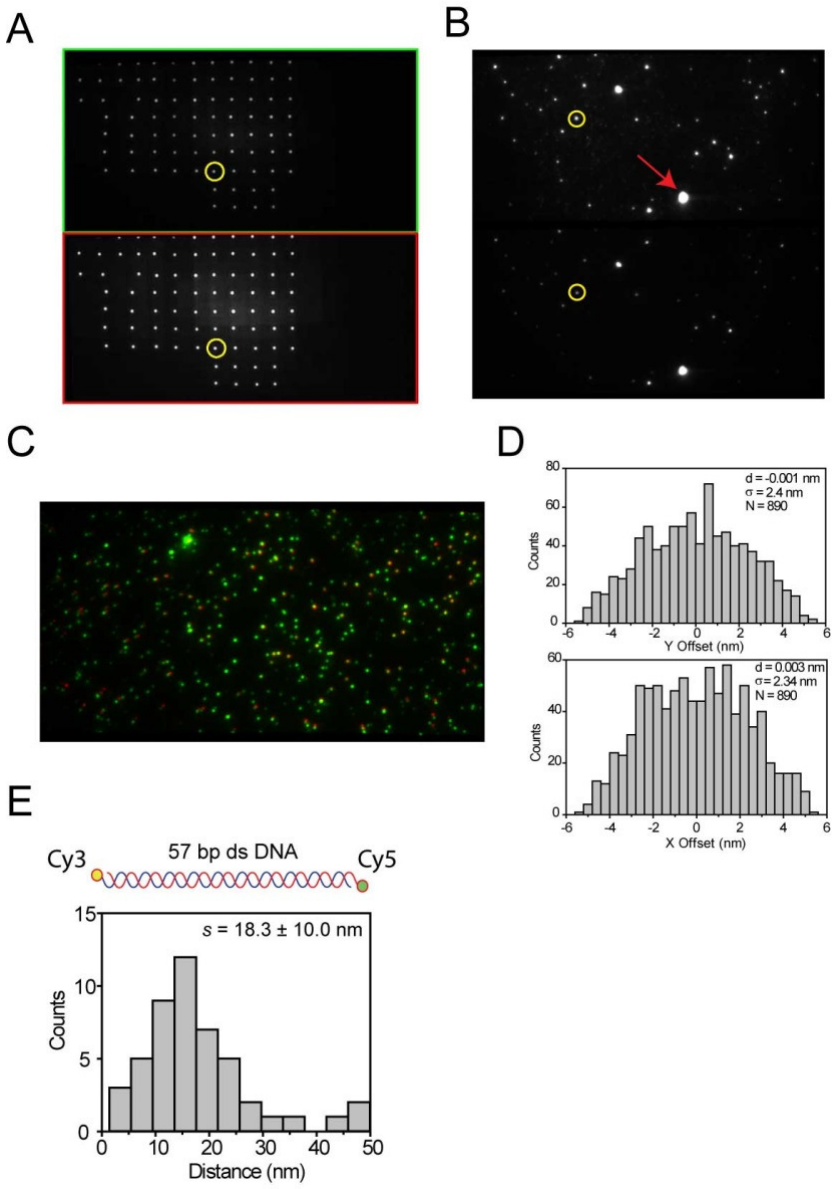


Figure 2.3. Registration of the two fluorescent channels. (**A**) A metallic film decorated with 180 nm diameter nanoholes was imaged under brightfield. Pairs of matching nanohole images (yellow circles) in two channels of the CCD were automatically detected and their positions were determined by two-dimensional Gaussian fitting for the first round of calibration. The sample was scanned with 20 nm increments in the *xy* plane to achieve sub-pixel registry in the entire CCD surface. (**B**) Pairs of Cy3/Cy5 fluorescent beads (yellow circles) were detected by using the calibration data obtained from nanohole imaging. A second round of calibration using a Cy3/Cy5 bead image was performed to refine the mapping algorithm. Aggregates (red arrow) in the sample were excluded from analysis. (**C**) Pairs of QD655 (green)/Rhodamine Red-X (red) probes were colocalized to correct the chromatic aberrations between QD655-QD585 channels. (**D**) Histogram of registration error between 890 individual QD655/Rhodamine Red-X pairs shows that the two channels can be registered together with an average error of 2.4 nm, in either direction. (**E**) 57 bp duplex DNA was labeled with Cy3 and Cy5 dyes at opposite ends. The two fluorescent channels were registered using an image registration map. The distance between Cy3 and Cy5 was measured to be 18.3 ± 10.0 nm (mean ± st.dev.) which agrees well with the expected length of the DNA molecule (18.8 nm).

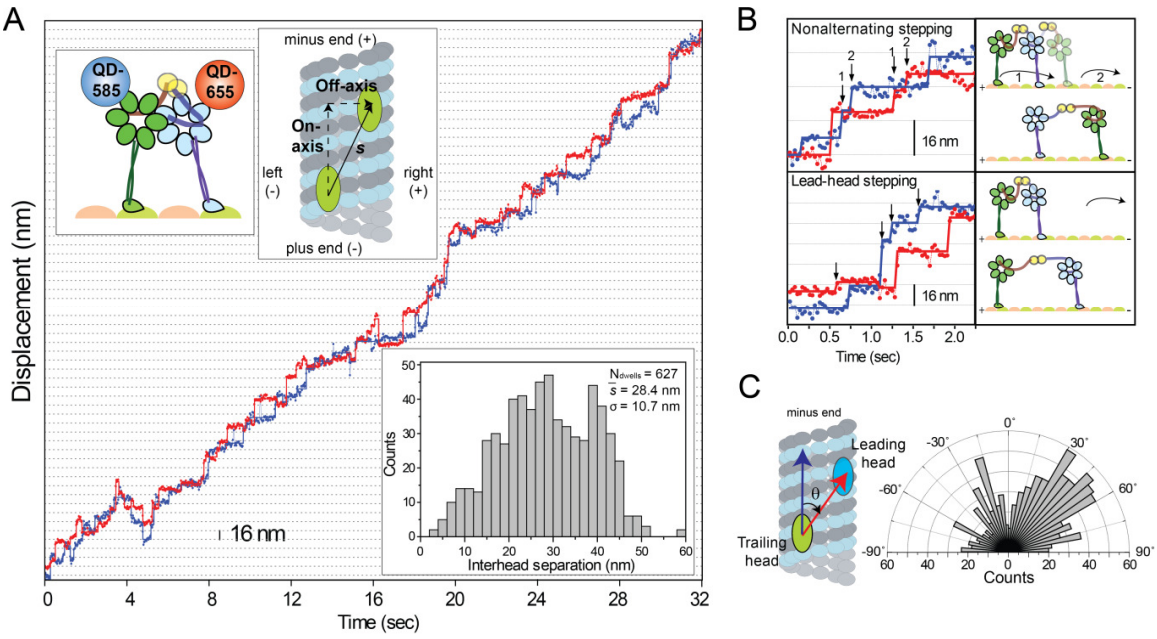


Figure. 2.4. (**A**) Stepping trace of GST-Dyn$_{331kD}$ labeled with QD-585 (blue) and QD-655 (red) shows that the heads move independently of each other during processive runs. The heads are separated by 28.4 ± 10.7 nm (bottom insert). (**B**) Examples of "non-alternating" and "lead-head" stepping (arrows) show that dynein stepping deviates significantly from the HoH mechanism. (**C**) Histogram of the angles between the interhead separation vector (red arrow) and the microtubule long axis

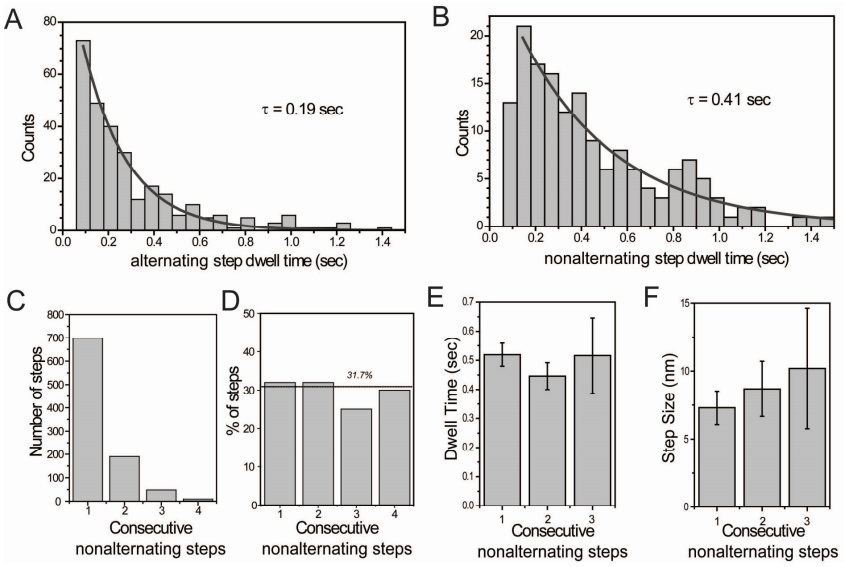


Figure 2.5. (**A**) Histogram of dwell times between the alternating-head steps of GST-Dyn$_{331kD}$. Data fits well (R^2 = 0.97) to a single exponential (black line) with a decay constant of 0.19 ± 0.01 sec/step. (**B**) Histogram of dwell times between consecutive steps taken by the same head (nonalternating steps), before the other head takes a step (exponential decay constant: 0.41 ± 0.03 sec/step, R^2 = 0.94). The ~2-fold difference between the stepping rates of nonalternating and alternating steps favors alternating stepping of the heads. (**C**) Number of steps observed for 1-4 consecutive nonalternating stepping events. (**D**) The probability of nonalternating stepping, after 0-3 consecutive nonalternating steps remains constant and agrees well with the probability calculated from the decay constants of alternating and nonalternating steps (31.7%). Due to the finite temporal resolution of the experiment, stepping of the heads occurring within one data point of each other was excluded from data analysis. (**D-E**) The average dwell time and step size of 1-3 consecutive steps (mean ± s.e.m.), respectively.

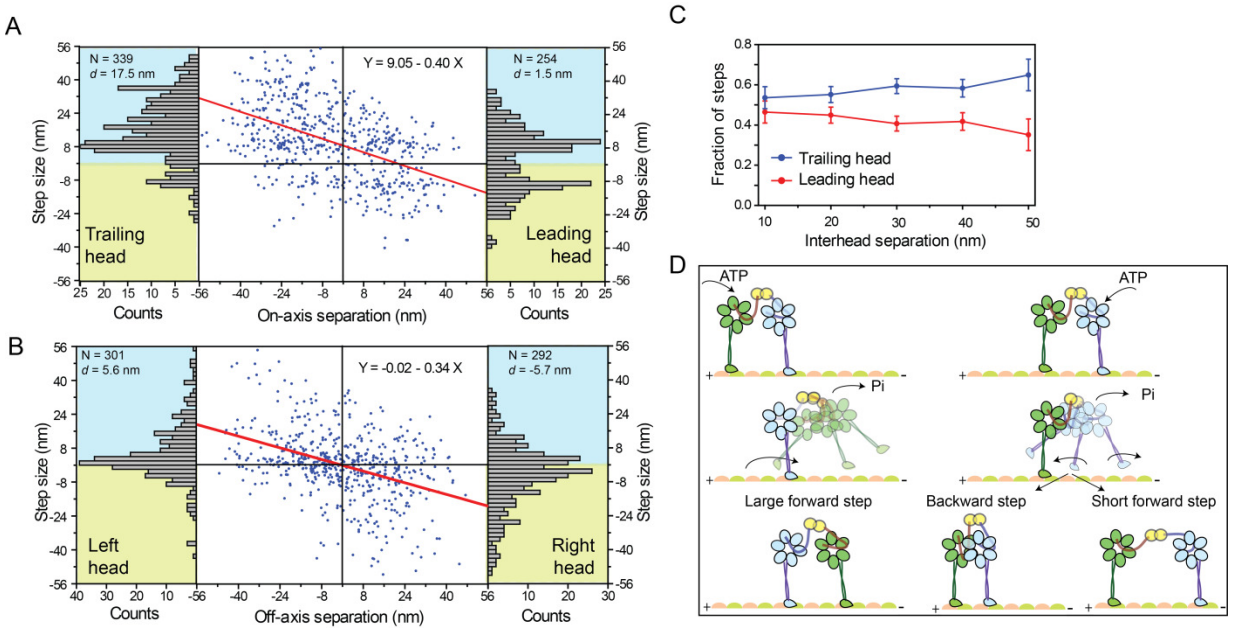


Figure. 2.6 (**A**) The on-axis step size (blue dots) of GST-Dyn$_{331kD}$ decreases linearly (red line) as a function of interhead separation and is biased forward by 9.1 ± 0.6 nm. The leading head takes shorter (d = 1.5 nm) steps with more frequent (p_{BW} = 0.45) backward steps, compared to the trailing head (d = 17.5 nm, p_{BW} = 0.14) (bar graphs). (**B**) Off-axis step sizes show a linear dependence on interhead separation without a bias to move towards the right (positive) or left (negative). (**C**) Fraction of the steps taken by the leading and trailing heads at different interhead separations (mean ± s.e.m.). (**D**) Tethered excursion model for the dynein stepping mechanism. Either the leading or trailing head can hydrolyze ATP and release from the microtubule. A diffusional search of the trailing head (green) is biased forward by interhead tension and the linker swing, resulting in a large forward step. In contrast, linker swing and tension bias the diffusion of the leading head (blue) in opposing directions, resulting in either a backward step or a short forward step.

The heads of native dynein also moved independently and their stepping behavior varied as a function of interhead separation, similar to GST-Dyn$_{331kD}$ (figs. 2.7-2.8). The results show that the tail domain is not involved in interhead coordination.

Our results show that dynein's stepping mechanism is different from processive kinesins and myosins. The stepping motion of these motors is driven by the powerstroke of the bound head, which moves the trailing head forward. For dynein, I propose a tethered excursion model (Fig. 2.6D), in which a conformational change that produces the minus-end bias occurs in the unbound head. Either head can bind ATP at the AAA1 site, followed by its release from the microtubule (Imamula et al., 2007). The linker undergoes a minus-end directed priming stroke upon ATP hydrolysis (Roberts et al., 2009, 2012), which moves its MTBD forward. The large and flexible linker allows the released head to diffuse over a wide area, resulting in both large interhead separations and variable step sizes.

The heads experience intramolecular tension at large separations, and the powerstroke of the bound head may occasionally trigger the release of the other head. In fact, I observed that the stepping probability of the trailing head increased at large separations (Fig. 2.6C). This result is consistent with force-induced movement of dynein, which requires less force when it is pulled towards the minus-end (Gennerich et al., 2007). In addition, tension can bias the diffusional search of the tethered head toward the bound head, preventing further extension of the dimer (Fig. 2.6D).

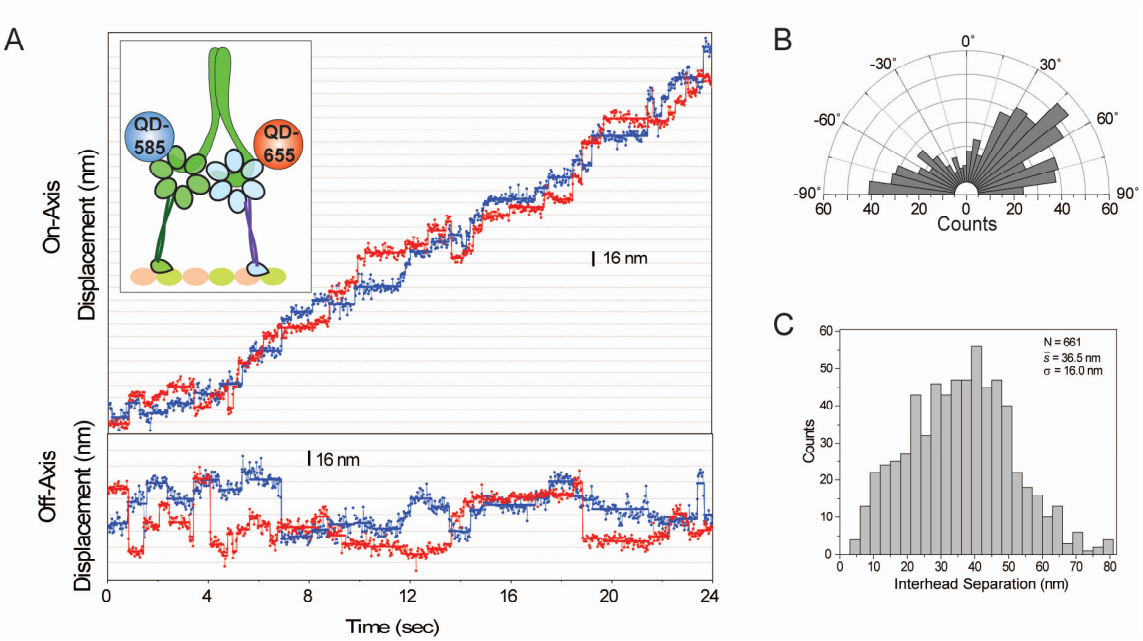


Figure 2.7. Stepping behavior of a native dynein motor. (**A**) Stepping trace of a native dynein labeled with QD-585 (blue) and QD-655 (red) shows that the heads move independently of each other during processive runs, similar to that of tail-truncated GST-dimer of dynein (GST-Dyn$_{331kD}$). (**B**) Histogram of the angles between the interhead separation vector (from trailing head to the leading head) and microtubule long axis. The leading head prefers to be located on the right hand side relative to the trailing head. (**C**) The heads are separated by 36.5 ± 16.0 nm on average. The average separation of native dynein is larger than that of GST-Dyn$_{331kD}$ (d = 30.4 ± 11.5 nm), possibly due to the larger separation of the heads allowed by the longer linker domain of the native dynein.

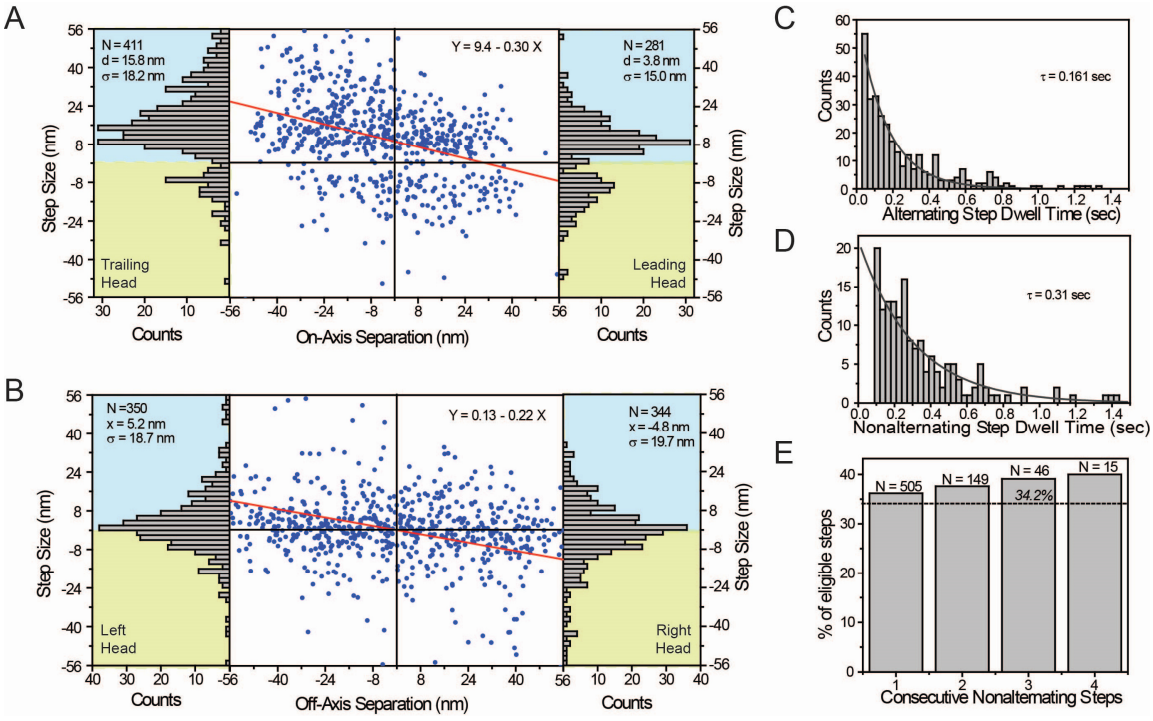


Figure 2.8. Stepping behavior of native dynein depends on interhead separation, similar to GST-Dyn$_{331kD}$. (**A**) The on-axis step size (blue dots) decreases linearly (red line) as a function of interhead separation and is biased forward by 9.4 ± 0.5 nm. The leading head takes shorter (d = 3.8 nm) steps with more frequent (p_{BW} = 0.34) backward steps, compared to the trailing head (d = 15.8 nm, p_{BW} = 0.16) (bar graphs). (**B**) Off-axis steps show a linear dependence on interhead separation without any bias (0.13 ± 0.53 nm) in the right (positive) or left (negative) directions. On average, the right head takes a ~5 nm step towards the left and *vice versa* (bar graphs). Dependence of the average step size in a native dynein head is less sensitive to interhead separation, compared to GST-Dyn$_{331kD}$ (0.30 vs. 0.38 in on-axis and 0.22 vs. 0.27 in off-axis). This difference may be due to the fact that intramolecular tension between the heads is a function of the length and flexibility of the linker domains. Native dynein, which has a longer linker, may be less sensitive to the extension of the dimer, compared to that of the tail-truncated artificial dimer of GST-Dyn$_{331kD}$. (**C**) Histogram of dwell times between the alternating-head steps of native dynein. Data fits well (R^2 = 0.94) to a single exponential (black line) with a decay constant of 0.161 ± 0.008 sec/step. (**D**) Histogram of dwell times between consecutive steps by the same head (nonalternating steps), before the other head takes a step (exponential decay constant: 0.31 ± 0.03 sec/step, R^2 = 0.83). The ~2-fold difference between the stepping rates of nonalternating and alternating steps favors alternating stepping of the heads. (**E**) The probability of nonalternating stepping, after 0-3 consecutive nonalternating steps remains constant and agrees well with the probability calculated from the decay constants of alternating and nonalternating steps (34.2%).

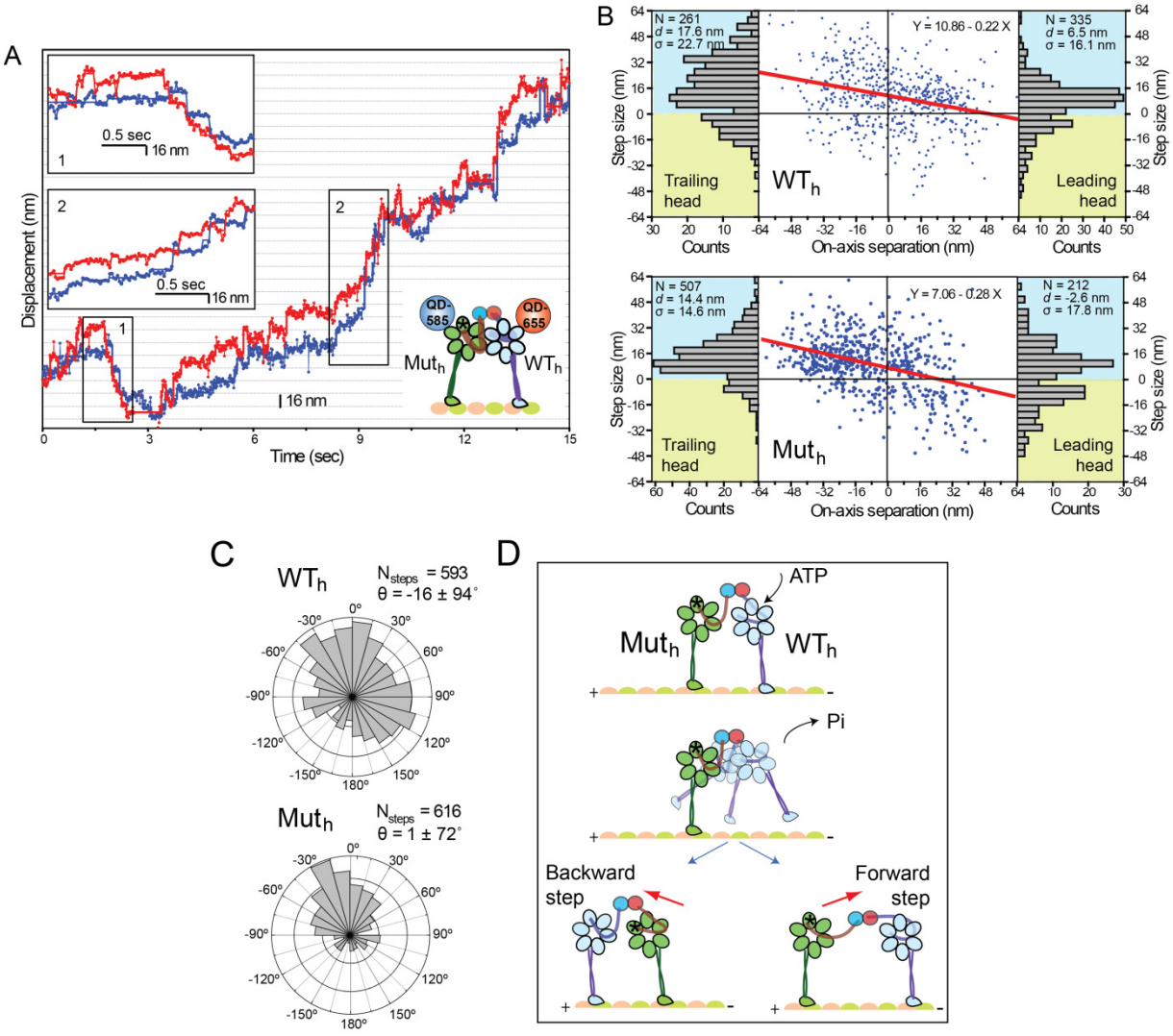


Figure. 2.9. (**A**) Stepping trace of the WT$_h$\Mut$_h$ heterodimer. Mut$_h$ and WT$_h$ were labeled with QD-585 (blue trace) and QD-655 (red trace), respectively. WT$_h$ mostly remains in the lead during a short backward run (insert 1) and a long forward run (insert 2). (**B**) The on-axis step size decreases linearly (red line) with increased interhead separation and is biased forward by 10.9 ± 0.8 nm for WT$_h$ and 7.1 ± 0.7 nm for Mut$_h$. Step size histograms (bar graphs) show that d_{WT} = 6.5 nm whereas d_{Mut} = -2.6 nm in the lead. (**C**) Histogram of the angles between interhead separation and stepping vectors of Mut$_h$ and WT$_h$. (**D**) Model for WT$_h$\Mut$_h$ processivity. ATP binding to WT$_h$ triggers its release from the microtubule and the subsequent diffusional search is biased forward by the powerstroke of the WT$_h$ linker. The weakly-attached Mut$_h$ moves towards WT$_h$ under linker tension.

The tethered excursion model suggests that a single force-generating head in a dynein

dimer can both take a step and drag an inactive head forward. I tested the motility of a heterodimeric dynein with one wild-type head (WT_h) and one mutant head lacking the ability to hydrolyze ATP at the AAA1 domain (Mut_h) (Cho et al., 2008; Reck-Peterson et al., 2006). Mut_h cannot undergo a powerstroke (Kon et al., 2005) and is weakly associated with the microtubule (Imamula et al., 2007). The WT_h\Mut_h heterodimer moved processively towards the microtubule minus-end (Fig 2.9A). WT_h was found in the lead 66% of the time. Similarly, during occasional short (4-5 steps) backward runs, WT_h remained in the leading position toward the plus end.

Mut_h exhibited different stepping characteristics in both the leading and trailing positions (Fig. 2.9B) than WT_h. The on-axis step size of Mut_h had reduced (7.1 ± 0.7 nm) minus-end directed bias, compared to WT_h (10.9 ± 0.8 nm). The probability of Mut_h being in the lead decreased as interhead separation increased (<25% at 30+ nm separations, Fig. 2.10), and Mut_h was more likely to step backward from the lead (d = -2.6 nm, p_{BW} = 0.44) (Fig. 2.9B). The average step size and stepping rate of Mut_h were similar to those of WT_h (Fig 2.8). Mut_h stepping was mostly directed toward WT_h, whereas the direction of WT_h stepping was largely independent of the position of Mut_h (Fig. 2.9C).

Thus, dynein motility does not require allosteric communication between the AAA1 sites, and only one force-generating head is sufficient for processive movement. WT_h usually remains in the lead and drives forward movement. The detachment of Mut_h from the microtubule can be facilitated by ATP binding to its AAA1 site (Imamula et al., 2007). Alternatively, Mut_h can release under tension generated through the powerstroke of WT_h. Since Mut_h lacks the ability to generate a powerstroke, its step size is mainly biased towards the WT_h under tension (Fig. 2.9).

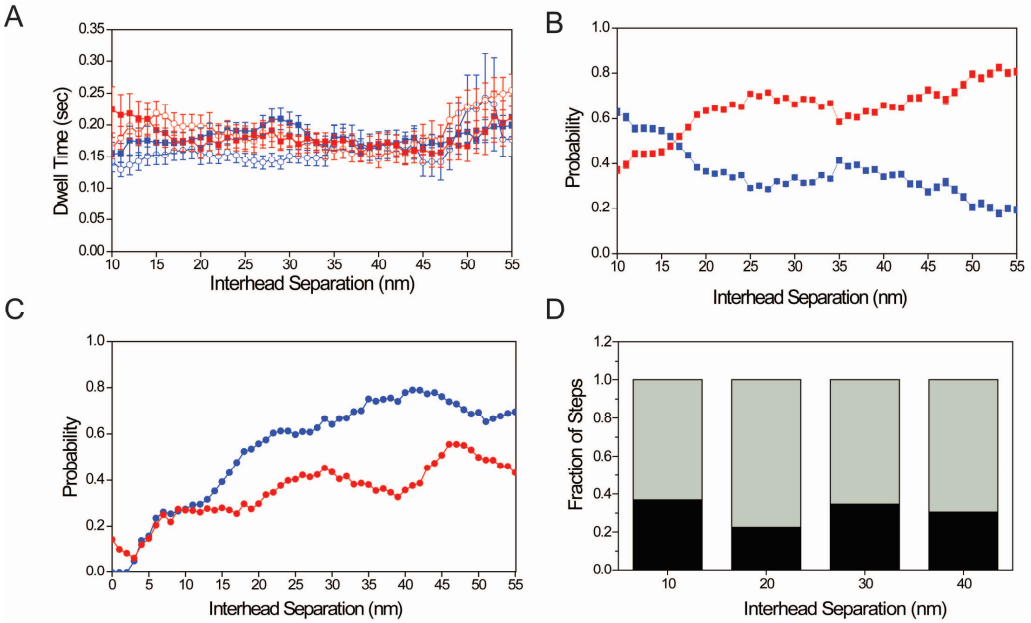


Figure 2.10. Stepping behavior of the WT_h/Mut_h heterodimer as a function of interhead separation. (**A**) Average dwell time vs. the interhead separation for WT_h (red) and Mut_h (blue), from either the leading (open circles) or trailing (closed squares) positions (10 nm sliding window average). Stepping rates of the two heads remain the same regardless of which head is in the lead. (**B**) The probability of the WT_h (red) and Mut_h (blue) being found in the leading position as a function of interhead separation. (**C**) The probability of the WT_h (red) and Mut_h (blue) taking a step towards the other head as a function of interhead separation. (**D**) Prior to Mut_h moving to the leading position, the fraction of steps taken by Mut_h in the forward direction (light gray) vs. WT_h in the backward direction (black) as a function of interhead separation.

Our results challenge established views of motor processivity that require coordination between the mechanochemical cycles of the heads. Kinesin (Clancy et al., 2011; Yildiz et al.,

2008) and myosin (Nishikawa et al., 2010) motility rely on mechanical and chemical gating mechanisms that allow the leading head to stay bound to its track while the trailing head moves forward. Dynein clearly moves by a different mechanism. I see no evidence of strict gating that keeps the heads out of phase. Processivity requires two heads to be physically connected (Reck-Peterson et al., 2006) to prevent detachment of the motor when one of the heads steps forward. It is possible that simultaneous detachment of both heads is stochastic. Dynein's high duty ratio (Shima et al., 2006) may allow the motor to take many steps before dissociation. Processivity in the absence of gating is also achieved by multiple monomeric kinesins (Furuta et al., 2013; Kamei et al., 2005) and engineered dimeric motors that have poor mechanochemical communication between the heads (Liao et al., 2009; Thoresen and Gelles, 2008; Yildiz et al., 2008).

2.4 Materials Methods, and Supplemental Data

2.4.1 Protein Expression, Labeling and Purification

The expression and purification of a native *S. cerevisiae* cytoplasmic dynein motor, tagged with GFP at the N-terminal tail and with DHA (Promega) at the C-terminal head (GFP-Dyn_{471kD}-DHA) was previously achieved (Reck-Peterson et al., 2006). Non-processive monomers of Dyn_{331kD}, encoding a.a. 1219-4093, were artificially dimerized by fusing their linkers to glutathione s-transferase (GST) at the N-terminus (Reck-Peterson et al., 2006). *In vitro* motility assays demonstrated that GFP-GST-Dyn_{331kD} moves processively with a similar speed to that of full-length dynein (Reck-Peterson et al., 2006). To specifically label dynein with fluorophores or biotin, a 26kDA DHA domain (Promega) was genetically encoded at either the C-terminal head domain or the N-terminal tail domain (Reck-Peterson et al., 2006). Heterodimeric dynein mutants were prepared by replacing the N-terminal GST tag with FRB and FKBP12 domains that dimerize in the presence of rapamycin . Monomeric dynein bearing a single point mutation (Mut_h, a glutamic acid to a glutamine point mutation (E1849Q) in the Walker B motif of AAA1) (Cho et al., 2008; Shima et al., 2006) was a generous gift of R.D. Vale.

All dynein constructs were purified using IgG beads and TEV protease cleavage, as described previously(Reck-Peterson et al., 2006). For one-color tracking assays, the homodimeric Dyn_{331kD} constructs were labeled with 10 μM HaloTag-biotin during protein purification. The excess ligand was removed while the dynein was attached to the IgG sepharose affinity column. The FKBP12-Dyn_{331kD}-DHA monomer (WT_h) was prepared by labeling with 10 μM HaloTag biotin as well. The FRB-$AAA1_{E/Q}Dyn_{331kD}$-DHA monomer (Mut_h) was prepared without any labeling.

2.4.2 Microscope

An objective-type total internal reflection fluorescence (TIRF) microscope was set up, using a Nikon Ti-E Eclipse inverted fluorescence microscope equipped with a perfect focusing system and 100X 1.49 N.A. Plano Apo oil immersion TIRF objective (Nikon). A 488 nm diode-pumped solid-state laser (Coherent Sapphire, 500 mW) was used for quantum dot (QD) and GFP excitation. In two-color experiments, QD-585 and QD-655 fluorescence was split into two channels (Q630LP dichroic mirror, Chroma) and imaged separately on the same CCD chip using an Optosplit II image splitter (Cairn Instruments). QD-585 and QD-655 signals were filtered

through 585/40 and 655/40 bandpass emission filters (Semrock), respectively, to reduce crosstalk between the two fluorescent channels to below 1%. One-color tracking measurements were recorded with a fast acquisition electron-multiplied charge-coupled device (EM-CCD) camera (Ixon EM^+, 128x128 pixels, Andor Technology) with an effective pixel size of 160 nm after magnification. Two-color data were collected with a 512x512 pixel EM-CCD camera (Andor Technology) with an effective pixel size of 106 nm.

2.4.3 One-Color QD Labeling and Motility Assays

One-color motility assays were performed on sea urchin axonemes (Gibbons and Fronk, 1979) non-specifically adsorbed to glass coverslips. The glass surface was then pre-blocked with 1 mg/mL casein in dynein assay buffer (DLB; 80 mM HEPES pH 7.4, 1 mM EGTA and 2 mM $MgCl_2$, 10% glycerol). Biotinylated GFP-GST-Dyn_{331kD}-DHA was flowed in at ~1 nM concentration to sparsely coat axonemes (determined by imaging the GFP fluorescence). After 1 minute, unbound motors were washed with 40 µl DLB buffer containing 1 mg/ml casein. Streptavidin-coated QD-655s were flowed in at 200 nM concentration and reacted with dynein for 2 minutes. Dynein motors were labeled after they were attached to axonemes to prevent aggregation on multivalent QD probes. Comparison of the number of GFP spots versus QD spots on axonemes in separate fluorescent channels showed that ~10% of dynein molecules are labeled with a QD under these conditions (data not shown). Streptavidin-QD labeling was highly specific as I did not observe any binding of QD to non-biotinylated dynein motors in motility assays (data not shown). The sample was imaged in the presence of DLB containing 5-12 µM ATP, 1 mg/ml casein, an ATP regeneration system (2 mM phosphoenolpyruvate and 0.1 mg/ml pyruvate kinase). 2% β-mercaptoethanol was also added to reduce QD blinking (Rasnik et al., 2006). To clearly identify dynein stepping in one-color assays, temporal resolution of image acquisition was increased to 2 msec while retaining nanometer localization. Labeling dynein with a QD did not substantially affect the motile properties of the motor based on motor run lengths and velocities (Reck-Peterson et al., 2006).

2.4.4 Two-Color QD Labeling

For two-color tracking measurements, homodimeric motors (GST-Dyn_{331kD}-DHA or GFP-Dyn_{471kD}-DHA) were labeled with HaloTag-coated QDs, which are significantly smaller than commercially available streptavidin-coated QDs (Table S1). Amino-coated QD-655 and QD-585 (Invitrogen) were reacted with HaloTag-SEO4 ligand (Promega) at ~1000-fold excess for 2-4 hours at room temperature in DLB buffer. The reaction was quenched by addition of 20 mM Tris pH 7.4 (15 min), and the from free label was removed using 20 KDa molecular weight cut-off spin concentrators four times prior to labeling. 50 nM dynein motors were reacted for 15 minutes with a mixture of excess (1-5 µM) HaloTag-coated QD-585 and QD-655 prior to introduction to the flow chamber. HaloTag-coated QD labeling was highly specific to the DHA domain inserted at the C-terminus of the motor, as we did not observe binding of these QDs to dynein without a DHA domain (data not shown). Since the observed dual-labeling efficiency was < 10% for microtubule-bound dynein motors in the presence of excess QD, no crosslinked aggregates were expected under these conditions. Furthermore, fluorescence images of both QDs exhibited complete blinking and uniform intensity in each fluorescent channel, strongly indicating that single QD-585 and QD-655 were attached to the dimer.

For the WT_h/Mut_h heterodimer experiments, WT_h was labeled with biotinylated HaloTag ligand during the purification step. The heterodimer was first constructed by a mixture of equimolar (1 µL each of 50 nM) amounts of WT_h-biotin and unlabeled Mut_h in the presence of 200 nM rapamycin for 10 minutes, prior to labeling with QDs (Reck-Peterson et al., 2006). 100 nM rapamycin was maintained in all solutions. To rule out the possibility that the experiment may select a small fraction of homodimers that might form in the sample, I verified that processive movement was not observed when only FRB- or FKBP12-tagged motors were introduced to the flow chamber. The mixture of FRB- and FKBP12-tagged motors started to move processively after Rapamycin addition. In addition, different labeling chemistries were used to attach different colors of QDs to FRB- and FKBP12-tagged dynein monomers. Mut_h and WT_h-biotin were labeled specifically with 100-fold excess of HaloTag-coated QD-585 and streptavidin-coated QD-655, respectively. The reaction with the QDs was allowed to proceed for 15 minutes. Biotin was added to 1mM to the motor-QD mixture immediately prior to addition to sample chamber to prevent surface attachment of streptavidin-coated QDs to biotin-BSA.

2.4.5 Two-Color Motility Assays

Two-color tracking assays were performed on surface-immobilized microtubules. The coverslips were coated with 1 mg/ml biotin-BSA and then treated with 1 mg/ml streptavidin. Porcine tubulin (1:20 of biotin-tubulin to unconjugated tubulin) was polymerized in the presence of 10 µM taxol in BRB80 buffer (80 mM PIPES, 1mM $MgCl_2$ 1mM EDTA, 10% glycerol, pH 6.8) (SCHIFF et al., 1979) and immobilized onto the streptavidin-coated flow chamber. Unbound microtubules were washed off with excess BRB80 buffer. Dynein-QD complexes were flowed onto the microtubules in DLB containing 1 mg/ml casein.

For the homodimeric dynein experiments, moving dyneins were imaged in the presence of 7 µM ATP, 20 mM phosphoenolpyruvate, 0.1 mg/mL pyruvate kinase (Roche), and 1% β-mercaptoethanol. Movies of dual-labeled dyneins were acquired at 30 msec temporal resolution (k_{step} = 0.06 steps/frame). For the heterodimeric dynein experiments, images were acquired at 15 msec temporal resolution in the presence of 40 µM ATP (k_{step} = 0.07 steps/frame). Dual-labeled moving spots were further analyzed for step size measurements.

2.4.6 Image Registration

To precisely measure the relative positions of QD-585 and QD-655, the two fluorescence channels were registered with respect to each other. Potential sources of error in these measurements include the positional offset, rotational and magnification differences between the two channels, irregularities in the CCD chip (*28*), local spherical aberrations in the optical system and chromatic aberrations (Churchman et al., 2005, 2006). Chromatic aberrations can be corrected if the same (or isospectral) set of probes are used in image registration and data collection. The relative distortions between the two channels were corrected using custom routines implemented in LabVIEW (National Instruments), MATLAB (The Mathworks), and Python using the SciPy package. A metallic film sample decorated with 180 nm nanoholes was translated in 20 nm increments in x and y axes by a piezoelectric nanopositioner (P527.3CD, Physik Instruments), ensuring subpixel coverage of the entire CCD surface. In a separate experiment, the sample was moved randomly in the *xy* plane by a micropositioning stage (MicroStage-20E Mad City Labs) for 5000 frames to achieve coverage of the CCD surface and similar results were obtained. The sample

was imaged under brightfield illumination synchronously with translation using custom image acquisition software written in LabVIEW. These images were processed to map the spot centers (0.8 nm localization accuracy) of the nanoholes from one half of the CCD to the other.

Primary maps from nanoholes were calculated as follows: The CCD surface was broken into 25-100 cells. A map of each cell was constructed using that cell's colocalizations and a polynomial transformation. Individual cells were connected using splines to make a continuous map of the entire CCD surface using nanoholes. Fig. 2.3 shows that the two fluorescent channels were registered with an average error of 2.53 nm. Second order corrections were determined by imaging and localizing custom-made dual-labeled fluorescent probes to avoid chromatic aberration. Second order maps of the entire CCD surface were constructed from the primary map, using ~10,000-100,000 fluorescent colocalizations and polynomial transformation only.

For Cy3 and Cy5 imaging assays, 100 µl of 0.2% (weight/volume) 200-nm diameter non-fluorescent amino polystyrene beads (Invitrogen) were labeled with a mixture of 10 µl of 4 mM Cy3 and 4 mM Cy5 NHS-ester. The brightness of these beads were >100 fold higher than that of single Cy3 and Cy5 probes, indicating that each bead is coated with hundreds of fluorescent dyes (data now shown). Coverslips were sparsely decorated with surface-immobilized Cy3/Cy5 beads. As a control, I scanned the CCD chip for 10 microns either in the horizontal or vertical directions, by taking 100 nm steps with a motorized stage (MadCity Labs, Microstage 20E). Matching fluorescent spots in Cy3 and Cy5 channels were fit to a 2D Gaussian. The two channels were registered to ~ 5 nm precision using a different set of Cy3/Cy5 beads within the same sample. Localization and calculation of offsets were performed using MATLAB and Python. The position of a single bead in Cy3 and Cy5 channels colocalize to within 0-4 nm in both x and y directions throughout the entire scan. The fluctuations in distance measurements were in the range of 6-8 nm, largely due to the localization error. These measurements were repeated using a different set of beads (scans 1-13) at different locations and directions on the CCD surface to verify that the mapping technique can reliably measure the distance between the two fluorophores throughout the entire CCD chip.

I have also tested our ability to measure the distance between Cy3 and Cy5 dye molecules using our mapping method (Fig. 2.4). 57 bp duplex DNA, labeled with Cy3 and Cy5 dyes on each of the 5' ends was purchased (IDT DNA). 5 nM DNA was non-specifically attached to a glass coverslip coated with 1 mg/ml polylysine in TE buffer with magnesium (10 mM Tris, 1 mM EDTA, 1 mM $MgCl_2$, pH 7.50). The surface was washed with 100 µL of TE with magnesium. The dual-labeled oligonucleotides were excited with 633 and 532 nm lasers and imaged at 500 msec temporal resolution. The two fluorescent channels were registered as described above. Localization error for each Cy3-Cy5 pair were calculated separately and only the pairs localized within 5 nm standard error of the mean were included in the data analysis.

For QD-585 and QD-655 imaging assays, QD-655 amino were coated with excess of Rhodamine Red-X NHS-ester (Invitrogen), which is iso-spectral to QD585 in 550-610 nm bandwith of the emission filter. The QD655-RhodamineX probes were used as a fiducial marker that appears in both QD585 and QD655 channels, which can be registered with 3 nm accuracy. Single dual-QD labeled DNA complexes were scanned across large areas on the CCD surface to test whether large variations in distance measurements between different QD-DNA complexes is due to poor image registration in parts of the CCD surface. Individual dual-QD DNA complexes with significantly different mean inter-QD distance, were selected and scanned at different parts of the CCD. The standard deviation of the magnitude of the inter-QD vector (r) of a single QD-DNA complex was 7-10 nm, which is significantly lower than the 18 nm standard deviation of

distance measurements of 50 QD-DNA molecules. The angle of the inter-QD separation to horizontal was also highly conserved during the scan, the standard deviation of the angle of the vector was within 10-20°.

I have performed distance measurements of single DNA polymers labeled with QD585 on one end and QD655 at the other end. The expected length of the DNA polymer is 18.3 nm. The diameters of QD probes were measured as 17 nm and 21 nm, respectively (Table 2.1). Therefore, I expect the center-to-center distance between the two QDs to be ~37 nm, assuming that central locations of QDs is along the same line with DNA. The average end-to-end distance of dual QD labeled DNA molecules was 34 ± 18 nm.

2.4.7 Step Size Analysis

The QD position was determined by Fluorescence Imaging with One Nanometer Accuracy (FIONA) (Yildiz et al., 2003), using a two-dimensional Gaussian fitting algorithm in MATLAB. The standard deviation of the center of the Gaussian fit, which represents the position of the QD center when dynein motors dwell between steps varied. The average error was 4 nm for the homodimer and 4.4 nm for the WT_h/Mut_h heterodimer. These fluctuations were higher than that of surface immobilized QDs 1-3 nm (SD) under the same experimental and imaging conditions. Therefore, the experimental noise in our assay is mostly inherent to the fluctuation of the dynein motor on microtubules, rather than photon shot noise.

The one-color traces were fit using a step finding algorithm (Kerssemakers et al., 2009), using a least-squares minimization. All of the analyzed traces were visually examined for the goodness of the fit. Minimum detectable step size was set to 3 nm. Typically, more than 20 steps can be detected from a single run. The two-color traces were fit in a two-dimensional plane (significant deviation in either axis constitutes a step) (Nishikawa et al., 2010). To ensure our ability to detect individual steps taken by dynein in two-color tracking assays (7 μM ATP, 30 ms temporal resolution), I have compared the two color step sizes with that of one-color measurements performed at ~10 fold faster image acquisition rate per dynein step (5-12 μM ATP, 2 ms per frame, Fig. 2.1 and 2.2). Average forward step sizes of one-color (10.6 nm) and two-color WT homodimer (12.0 nm) measurements are in good agreement with each other.

2.4.8 Interhead Distance Measurements

To reliably measure interhead separation of a dynein dimer, I used organic dyes (~1 nm across), which are significantly smaller than QDs. GST-Dyn_{331kD}-DHA dynein was labeled for 30 minutes with a mixture of Cy5-HaloTag and Cy3-HaloTag reagent. The Cy3- and Cy5-HaloTag reagent was prepared by reaction of a 1 mM Cy3- or Cy5-NHS ester (GE Healthcare) with 100 μM HaloTag-SEO4 reagent (Promega) for 2 hours, followed by quenching with 10 mM Tris, pH 8.0. The labeled dynein was flowed onto surface-immobilized microtubules. 1 mM ATP was added for 10-30 sec to allow dynein to adopt a relevant stepping conformation. Under these conditions, I observed > 90% of the motors moving processively along microtubules (data not shown). The flow chamber was then washed with 200 μl DLB to remove ATP and free label. 1 mM AMP-PNP (a non-hydrolysable ATP analogue) was then flowed in to tightly attach motors to the microtubules (Imamula et al., 2007). Static dynein motors were imaged by 532 and 633 nm laser excitation (Coherent Inc.) in TIRF mode. Each spot was localized and mapped using the software and equipment described above. To exclude dynein motors that are nonspecifically adhered to the glass

surface, I have only analyzed microtubules that are labeled with four or more labeled dynein motors.
In dynein interhead separation measurements, I calculated the average position of each head per dwell location. Since the average dwell time of dynein was equivalent to acquisition of 10 frames in our imaging conditions, standard error of the mean per QD position was equal to 1.4 nm. Therefore, I estimated that the error in interhead separation measurements was ~3.7 nm, which including the localization errors of both QDs and the registration error.

2.4.9 Dynamic Light Scattering Measurements

Dynamic light scattering (DLS) measurements of QD size were conducted on a Malvern Zetasizer Nano. QDs were diluted to 20-40 nM in PBS (10 mM sodium phosphate pH 7.4, 137 mM NaCl, 3 mM KCl) and filtered through a 0.2 µm syringe filter immediately prior to measurement. The count rates were typically in the range of 150-300 kcps. Five consecutive runs of 3 minutes were averaged for each experiment and three experiments were conducted for each QD sample. Data were fit by volume weighting using the built-in software. The sizes are reported in Table 2.1.

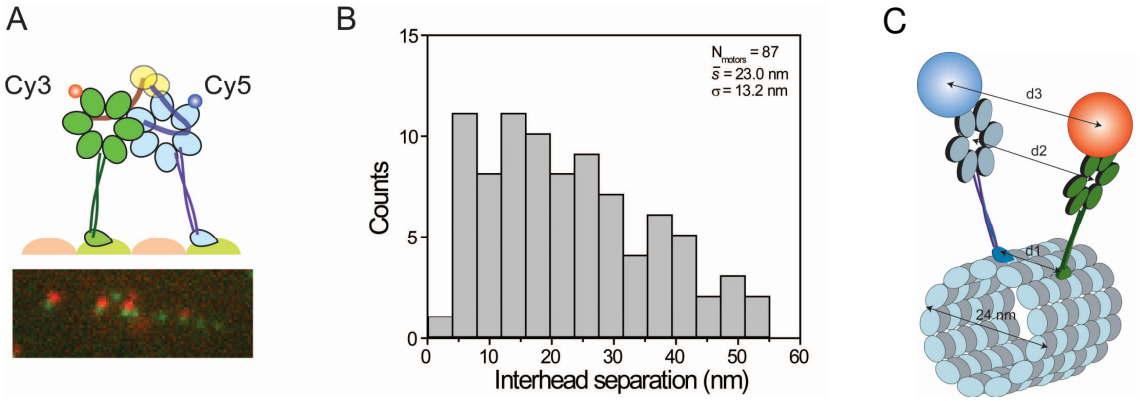


Figure 2.11. Measurement of the interhead separation using small organic dyes. (**A**) Interhead separation was measured between C-terminal Cy3 and Cy5 dyes on a GST-Dyn_{331kD} construct (top) after immobilizing motors on a microtubule in the apo state (bottom, Cy3: green, Cy5:red). (**B**) The fluorescent images of 87 dual-labeled dynein molecules were analyzed, using the image registration protocol. Mean interhead distance (23.0 ± 13.2 nm) is significantly shorter than the measured distances from QD-labeled dynein dimers (28.4± 10.7 nm, Figure 2A). (**C**) Diagram of a dual QD-labeled dynein on a microtubule shows that the off-axis distance between the two QDs (d_3) overestimates the actual off-axis distance between the heads (d_2) which is also larger than the off-axis distances between the two microtubule binding domains (d_1). This is due to the cylindrical shape of the microtubule filament (24 nm diameter). QD size may not significantly affect the on-axis distance if the heads are oriented parallel to each other and are separated by more than ~12 nm.

Table 2.1. Sizes of the QDs used in high resolution tracking assays. The diameter of QDs were measured by dynamic light scattering measurements. Correlograms were fit using Zetasizer instrument software using the "by volume" weighting. See Supplemental Methods for details.

Quantum Dot		**Size (mean ± SD)**
585-NH_2-HaloTag		17.2 ± 1.5 nm
655-NH_2-HaloTag		20.6 ± 4.5 nm
655-Streptavidin		22.1 ± 1.6 nm

CHAPTER 3. INVESTIGATING THE ROLE OF LINKER TENSINON IN DYNEIN MOTILITY USING TWO-COLOR FLUORESCENCE

3.1 Summary

In Chapter 2, I used a novel two-color fluorescence assay to elucidate the stepping mechanism of cytoplasmic dynein (DeWitt et al., 2012). While dynein appears to be a largely uncoordinated stepper, I also found evidence of residual coordination in the stepping pattern. In particular, the trailing head was more likely to take a step than the trailing head (Fig 2.4), and alternating steps were more likely than non-alternating steps (Fig 2.5).

These characteristics, along with changes in step size (Fig 2.6), appear only at high interhead separations, suggesting that tension on the flexible linker between the heads may play a role. Specifically, the altered stepping probability at high interhead separation suggests that the leading head may be gated (prevented from taking a step) at certain configurations. In this chapter, I further explore this residual coordination using two-color studies on mutants of dynein that are predicted to have altered linker tension behavior. By inserting a flexible linker between the two heads, I observe an almost complete loss of coordination, indicating that the coordination seen previously is not required for robust motility *in vitro* (Yildiz et al., 2008).

I compare this un-coordinated motility to the motility of a heterodimer wherein one head that cannot bind or hydrolyze ATP, and is rigidly attached to the MT, and one wild-type (WT) head (Imamula and Kon, 2007). The mutant head can only step through forced-unbinding from the MT, generated through tension generated by the WT head. Therefore, I expect increased tension on the linker in this mutant. Consistent with the decreased stepping probability of the leading head seen in Chapter 2, the WT head appears to be gated head in many configurations of the motor. However, this gating is relieved when the WT head is immediately behind the mutant head. Taken together, these data indicate that linker tension can gate the heads under certain configurations of the motor, but that abrogation of this gating pathway is not detrimental to dynein motility.

3.2 Introduction

While most organisms contain a wide variety of plus end-directed kinesin motors, most cells contain only a single cytoplasmic dynein heavy chain gene (Roberts et al., 2013). In order to carry out dynein's many functions within cells, dynein exhibits two kinds of flexibility. It is structurally flexible: it takes a wide variety of step sizes (Reck-Peterson et al., 2006). The two heads in the large dynein homodimer remain widely separated during stepping, and do not adopt the compact configuration of the kinesins (DeWitt et al., 2012; Yildiz et al., 2004a). In the previous chapter, I showed how dynein steps through a largely uncoordinated "tethered excursion mechanism (Fig 2.6D). Dynein is also functionally flexible: cytoplasmic dynein participates in many different activities, including transport of cargoes and organelles, positions and migration of the nucleus, and positioning of spindle microtubules during mitosis (Kardon and Vale, 2009; Roberts et al., 2013; Vallee et al., 2004). However, the relationship between dynein's structural flexibility and its functional flexibility are only beginning to be understood (Huang et al., 2012; McKenney et al., 2010; Roberts et al., 2013).

In Chapter 2, I showed that dynein steps predominantly through an uncoordinated stepping mechanism (DeWitt et al., 2012). However, several results indicated that a certain amount of

coordinated behavior was still present. Specifically, dynein was more likely to take alternating steps than non-alternating steps (Fig. 2.5), and the probability of the leading head taking step was less than the probability of the trailing head taking a step, especially when the heads were widely separated (Fig. 2.6C) (DeWitt et al., 2012; Qiu et al., 2012). It remains unclear to what extent linker tension affects the stepping rate, and whether tension is important to robust motility. I hypothesize that the coordinated activity was a result of tension, and a gating mechanism is not required for processive motility.

3.3 Two-Color Experiment on a Dynein with Reduced Linker Tension

To study the effects of altered tension on stepping, I employed the two-color fluorescence assay with increased temporal resolution to unambiguously identify steps (DeWitt et al., 2012). The linker tension was reduced by inserting a flexible GS_{48} linker between the heads of the WT-like construct employed in chapter 2 (Dyn_{331kDa}) (DeWitt et al., 2012; Gennerich et al., 2007; Reck-Peterson et al., 2006). This insert acts as a soft spring between the heads, reducing the tension at a given separation, compared to Dyn_{331kDa}. This construct ("GS dynein") has an identical velocity to WT dynein (Frank Cleary, data not shown). Despite identical overall motility properties, I hypothesized that the GS motor lacks the gating of the heads at high interhead separation, and has a low tendency to take non-alternating steps. To analyze the effects of reduced tension in more detail, I conducted two-color experiments at identical conditions for both Dyn_{331kDa} ("WT dynein") and Dyn_{331kDa}-GS_{48} ("GS dynein").

I applied the two-color mapping assay at 5 msec temporal resolution and 7.5 μM ATP. The results are shown in Fig. 3.1. As seen previously, both the leading and trailing heads can take a step (Fig. 3.1b, 3.1c), in contrast to kinesin, where only the trailing head steps (Yildiz et al., 2004a). The step size along the MT-axis decreases by ~0.4 nm for every 1 nm of separation towards the MT minus end (Fig. 3.1c). Despite the addition of a long flexible GS insert, both WT and GS heads show very similar overall relationship between separation and step size (Fig. 3.1c).

The dwelling locations of the two heads during stepping are shown in Figs. 3.1e and 3.1f. While the WT motor is dwelling between steps, the leading head is more likely to be found to the right of the trailing head, while looking towards the MT minus end. In contrast, the GS insert has no preferred angular dwelling location. Thus while the MT-axis stepping behavior of the two motors is very similar, the GS insert linker is much more pliable in the off-axis direction, limiting its ability to position the heads relative to each other. Consistent with this interpretation, the two heads remain a similar distance apart on average, but the GS more frequently accesses both longer and shorter interhead distances with greater frequency (Fig. 3.1f). These results show that the linker structure of dynein has indeed been altered by the GS insert. Therefore, robust motility and stepping behavior does not depend substantially on linker tension.

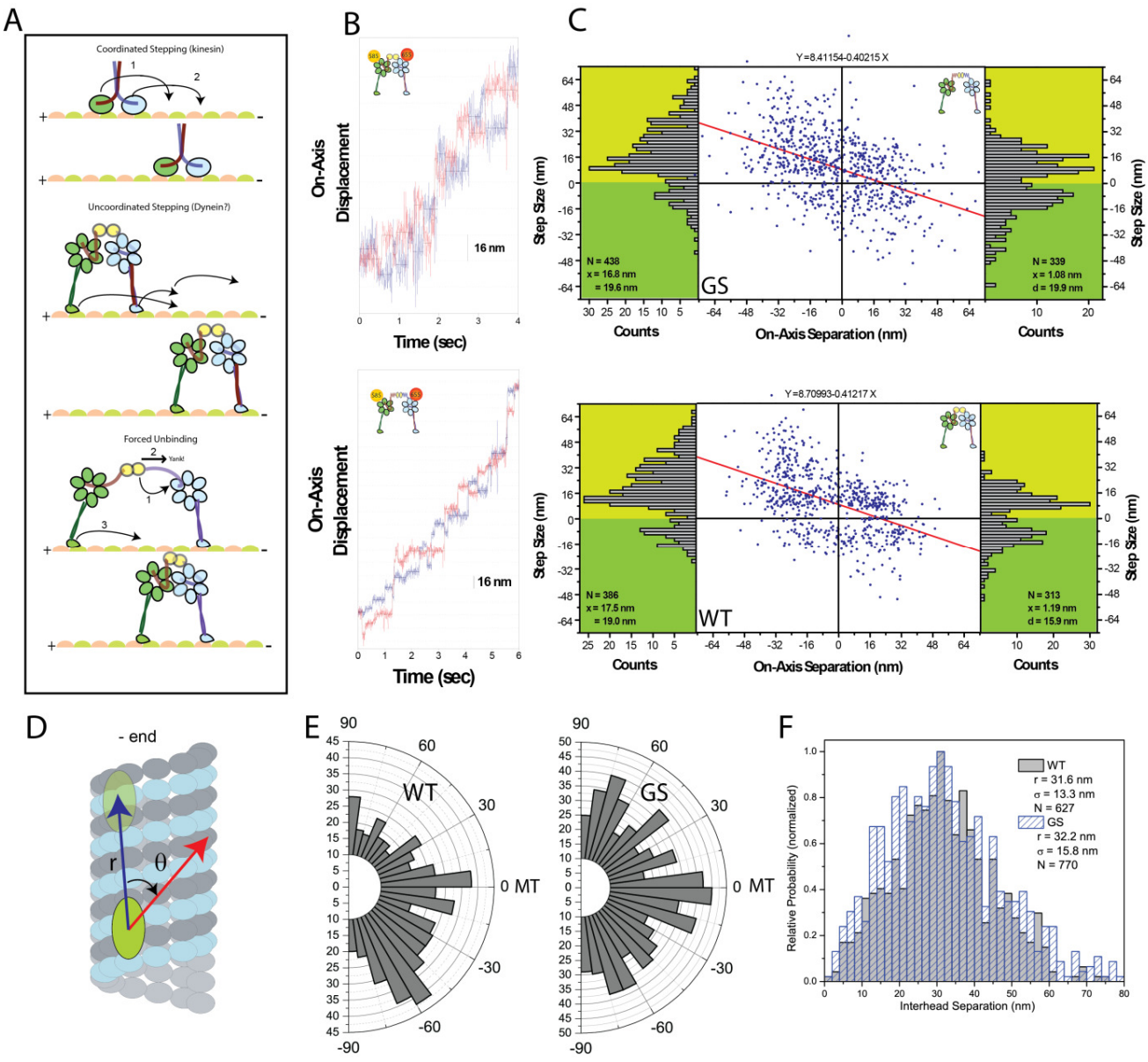


Figure 3.1. Two-color properties of the GS-insert dynein, compared to WT dynein. A) Conventional kinesin takes coordinated steps. The goal of this study is to first determine how much dynein can coordinate its steps, and whether that coordination is important to motility. Conversely, it is possible that a head can be pulled off the MT through force. B) Example traces from the two-color experiments on WT and GS-insert dynein. The heads are labeled with different-colored quantum dots, and overlaid using two-color registration. C) The stepping behavior of WT and GS-insert dynein are similar, but GS motor accesses a broader distribution of head-head separations. Both show a decrease in average step size with on-axis separation. D) The orientation of the two heads during a dwell can be expressed as an angle from the leading to the trailing head, and a distance between the two heads. E) The leading head of the WT motor has a tendency to dwell to the right of the trailing head, relative to the MT minus end. The GS-insert dynein lacks this tendency. F) The distribution of separations between the two heads is broader for the GS-insert dynein than for the WT dynein. These data indicate the GS-insert has added flexibility to the linker without altering overall stepping behavior.

Does this change in linker tension alter the extent to which the heads coordinate release from the microtubule? Turning to the release times of the two constructs, some interesting differences emerge (Fig. 3.2). While the leading head in WT steps frequently, it steps increasingly less frequently compared to the trailing head as the two heads become more widely separated (Fig. 3.2a) (DeWitt et al., 2012; Qiu et al., 2012)). This decrease, not substantial to begin with, is almost completely absent in the GS construct, consistent with reduced tension-gating between the heads.

Despite the overall uncoordinated character of dynein stepping, alternating steps were more likely than non-alternating steps (Fig. 3.2b). The dwell time distributions of alternating and non-alternating steps of WT dynein bear out this difference (Fig. 3b top versus bottom). Across the entire dataset, alternating steps are significantly more likely than non-alternating steps, even if short dwell times are eliminated from analysis. In contrast, the GS construct does not show any bias between alternating and non-alternating steps, indicating that the GS insert in the linker removed this behavior without affecting motility (Fig. 3.2b). GS dynein appears to step purely through the "tethered excursion" mechanism described in Chapter 2.

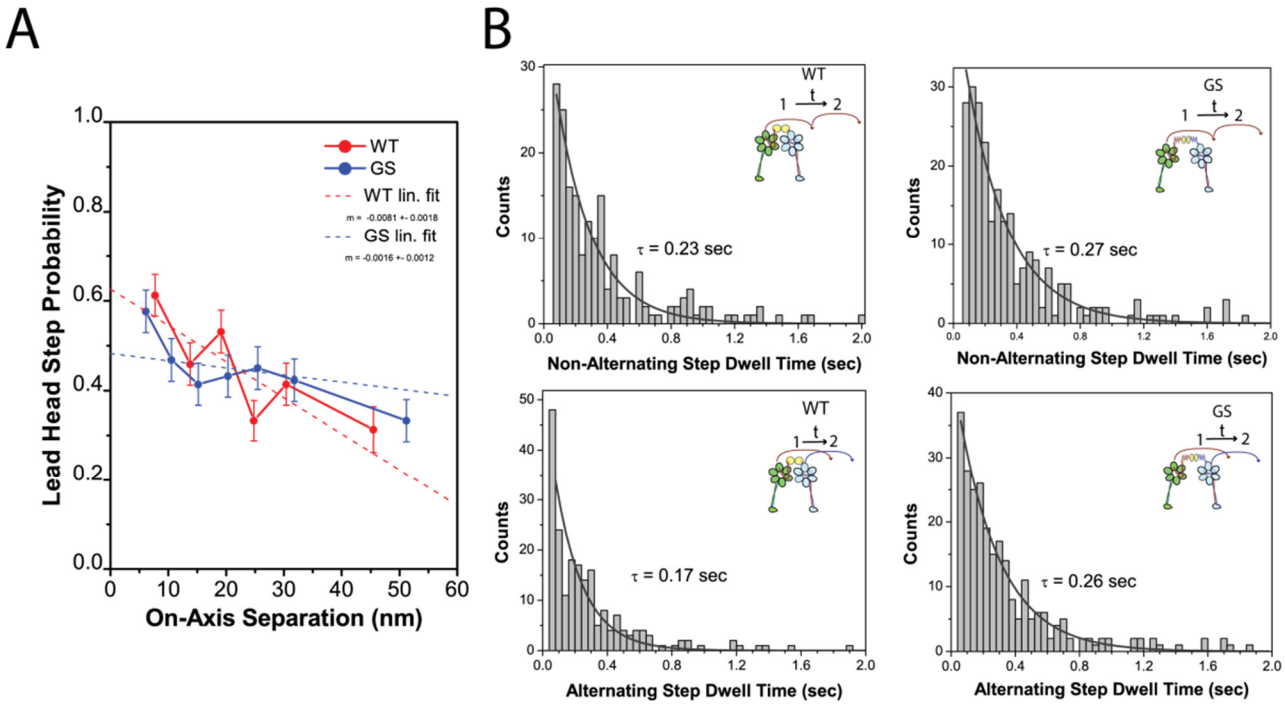


Figure 3.2 The GS insert dynein lacks coordination. A) Fraction of steps taken by the leading head versus on-axis separation between the leading and trailing heads. Solid lines: binned averaged data. Dashed lines are linear fit to the raw data. Note that leading head in the GS motor is nearly equally likely to step as the trailing head, regardless of separation. B) Histograms of dwell times between alternating steps and non-alternating (same head stepping) steps. The WT motor is less likely to take non-alternating steps, while the GS motor is as likely to take non-alternating as alternating steps.

3.4 Two-Color Experiment on a Dynein with Increased Linker Tension

The results from the GS dynein tracking experiment suggested that partial coordination can be removed when linker tension is reduced, and vice versa. To address this, I constructed a heterodimer of a WT head and a head lacking the ability to bind ATP at the primary site of hydrolysis ($AAA1_{K/A}$). This mutation completely abolishes dynein motility in a homodimeric context (Kon et al., 2004), and forms a persistent tightly bound state in a monomeric context (Imamula and Kon, 2007). In contrast to the GS construct, where the ability of one head to alter the release of the other is limited, the mutant head of this construct can only step when pulled off of the tubule by the active WT head. It is possible that the presence of the inactive head forces the WT head into conformations with high linker tension owing to the difficulty of pulling the mutant head off the track. Therefore, if tension can get one of the heads, than we expect configuration-dependent gating of the WT head.

To investigate this, I use a similar two-color assay to measure the stepping of both head simultaneously (Fig. 3). The heterodimer was tracked with a two-color assay at 15 msec time resolution in saturating (1 mM) ATP (Fig. 3.3a). The construct was substantially slower than QD-labeled WT construct (Frank Cleary, data not shown). The step sizes vary with MT on-axis separation in a matter similar to the WT and GS dyneins (Fig. 3.3b), although the WT head is found in the leading position 72% of the time (Fig. 3.3c). Instead, slowing is mostly due to gating of the WT head (Fig. 3.3d). Although the WT head steps more frequently than the mutant head (Fig. 3.3d), it steps much less frequently than a one head of a WT dynein (8 s^{-1}, (Cho et al., 2008)), measured in a separate experiment at 2 msec time resolution.

If the WT head is gated by linker tension, than the gating should be configuration should be configuration-dependent. The stepping rates of the two heads vs. separation are presented in Fig. 3.3e. When the WT head is widely separated from the mutant head, its stepping rate is very low, while when the WT head is found immediately behind the mutant head, its stepping rate increases to approach that of a WT homodimer (Fig. 3.3e).

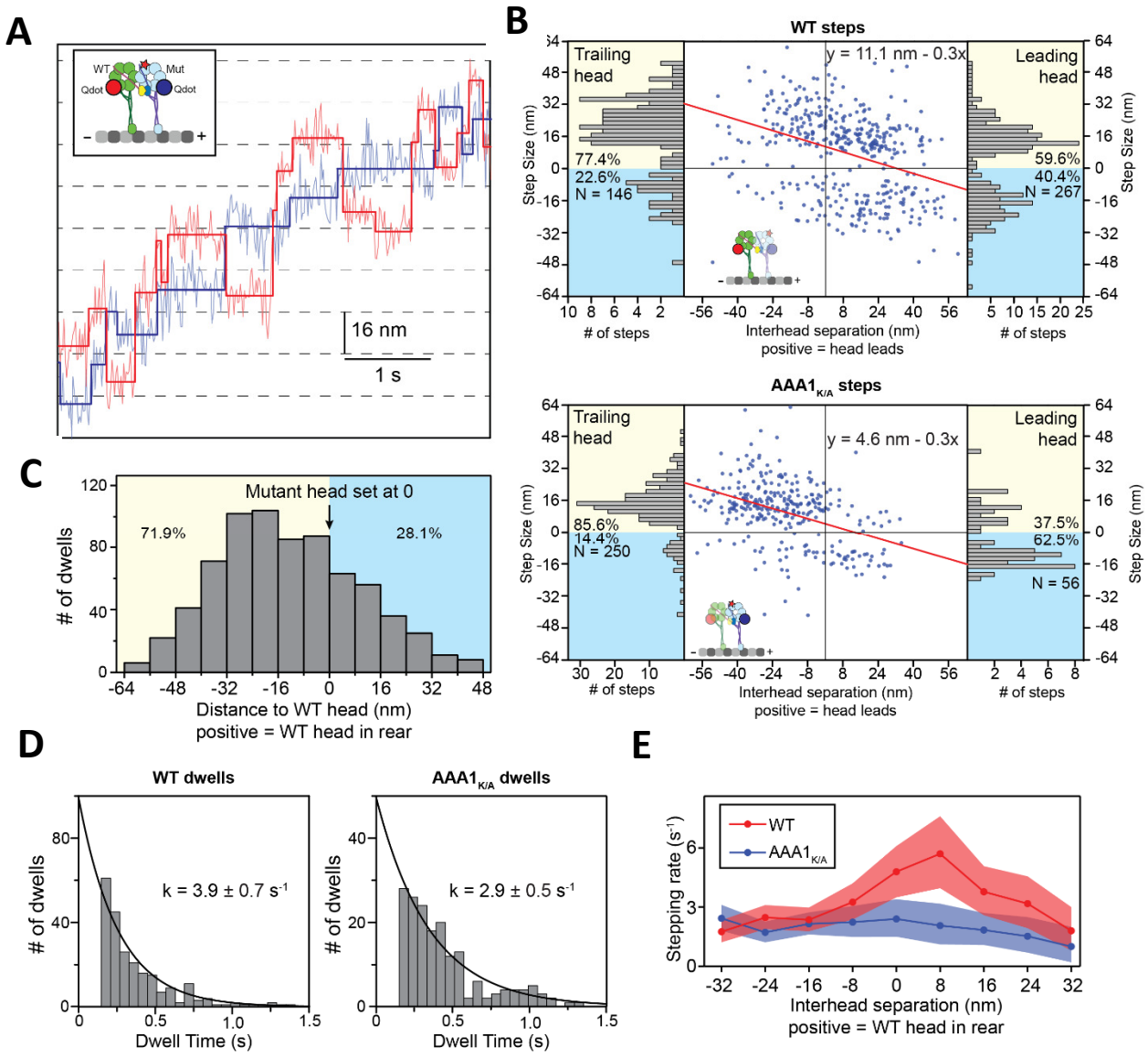


Figure 3.3. Tension gating of a dynein is observed at high interhead separations in a motile dimer. (a) A representative trace showing simultaneous tracking of $AAA1_{K/A}$/WT stepping properties with two colors of quantum dots at saturating (1 mM) ATP. (b) Both heads take smaller steps when they release the MT in the leading position, similar to WT dynein. (c) The $AAA1_{K/A}$ head remains in the trailing position 71.9% of the time and takes mostly backward steps when stepping from the leading position (62.5%). (d) Histogram of the dwell time between steps of the WT (left) or $AAA1_{K/A}$ (right) head, independent of the action of the other head, with exponential fit (± 95% confidence interval). (e) Stepping rates of the WT and $AAA1_{K/A}$ heads as a function of interhead separation (shaded region is the 95% CI). The WT head steps more frequently when it is positioned close to the $AAA1_{K/A}$ head, and is otherwise as a similar rate to the $AAA1_{K/A}$ head, indicating that the WT head is gated at high interhead separations.

3.5 Conclusion

Combining the results of the WT, GS, and heterodimer experiments, it is clear that tension affects the partial coordination of the motor. I propose that at close-in conformations, linker tension is low, and both heads are free to step. At more extended conformations, the heads become gated. The trailing head is more likely to step, and tends to step by being pulled off the MT (Fig. 3.4). Evidence for forced unbinding favoring the rear head comes from optical trap experiments performed in parallel with this study (Frank Clearly, unpublished).

These data raise the possibility that dynein may step through two different pathways. In one pathway, tension along the linker pulls either head off the MT track, resulting in an ATP-independent step. The second pathway resembles the "tethered excursion" model from our previous work (DeWitt et al., 2012). In this model, ATP may bind to either head, causing release from the MT (Imamula and Kon, 2007; Kon et al., 2009). This head releases from the MT, and undergoes a minus end-directed priming stroke (Roberts et al., 2009). Release of hydrolysis products regenerates the pre-powerstroke, tightly bound state.

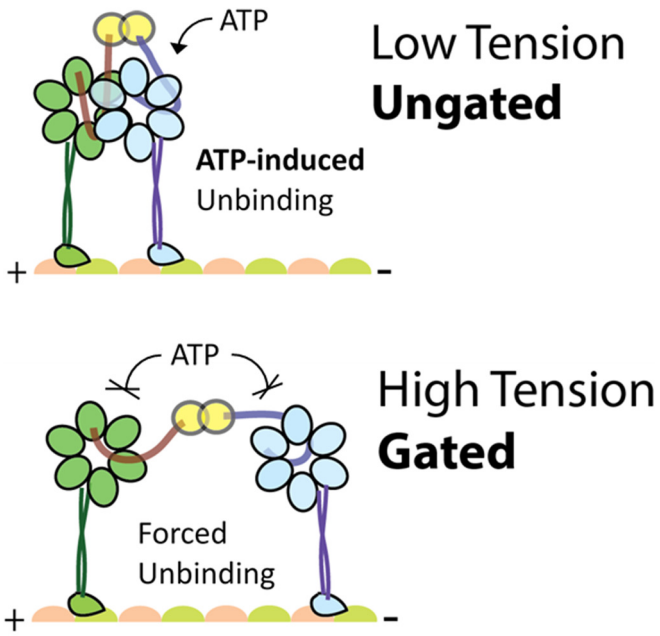


Figure 3.4. Tension on the linker gates the motor at high interhead separation. At low separations, tension through the linker is reduced, and the heads are ungated; ATP can efficiently direct MT unbinding. At high separations, the tension through the linker is high, and the heads are gated. Instead, the heads step through forced unbinding, which favors the rear head.

3.6 Materials and Methods

3.6.1 Cloning, Molecular Biology, and Protein Purificiation

The $Dyn1_{331kD}$-GS_{48} construct was provided by Frank Cleary, and will be discussed in more detail elsewhere (Cleary, DeWitt, et al, unpublished). Briefly, the HALO- $Dyn1_{331kD}$ used in the studies described in Chapter 2 (DeWitt et al., 2012) was converted to HALO- $Dyn1_{331kD}$-GS_{48} by first generating an acceptor strain to the $Dyn1_{331kD}$ N-terminus by knocking in a URA gene, and plating transformants on medium lacking uracil. Knock-in of $Dyn1_{331kD}$ -GS_{48} N-terminus DNA was accomplished by transformation and subsequent plating on minimal media containing 5'-FOA to counter-select for transformants lacking URA. The final construct resembled the $Dyn1_{331kD}$ GST homodomer used in Chapter 2, bearing a C-terminal HALO tag for directed attachment of HaloTag ligands, including HaloTag quantum dots (see below), followed by the $Dyn1_{331kD}$ minimal motor. At the N-terminus, the construct bore the GS_{48} flexible linker, a GFP, and the GST homodimerization domain.

The $Dyn1_{331kD}$-$AAA1_{K/A}$/ $Dyn1_{331kD}$ heterodimer was constructed from two monomeric strains: a "WT" strain bearing an N-terminal FRB domain, described elsewhere (Banaszynski et al., 2005; DeWitt et al., 2012; Reck-Peterson et al., 2006), and a $AAA1_{K/A}$ (K840A at the Walker A loop of the WT FKBP- $Dyn1_{331kD}$-HALO construct) mutant construct bearing and N-terminal FKBP domain. This construct, also provided by Frank Cleary, was constructed using the same acceptor strain used for the $AAA1_{E/Q}$ mutant characterized in Chapter 2, and was otherwise identical. Both strains bore a C-terminal HALO.

$Dyn1_{331kD}$-GS_{48} was purified in a manner identical to WT dynein, as described (DeWitt et al., 2012; Reck-Peterson et al., 2006). Monomeric FKBP-$AAA1_{K/A}$ and FRB-WT were prepared identically as well except the WT monomer was labeled with 10 μM Biotin HaloTag for 1 hr during purification. After purification, all constructs were further purified using MT bind-and-release to select for functional protein (Reck-Peterson et al., 2006; Yildiz et al., 2008), resulting in 200-400 μL of 200-500 nM dynein per 2L of yeast culture for use in single-molecule assays.

3.6.2 Microscope and Imaging

Experiments were conducted in the same microscope as described in Chapter 2, using a 488 diode-pumped solid-state laser for QD TIRF illumination.

The WT and GS homodimer were imaged using the same QD585/QD655 pair used for the study in Chapter 2 (Life Technologies). Briefly, the fluorescence was split using an OptoSplit (Cairn Scientific) containing a 605 dcxr beam splitter, a 585/40 bandpass filter (for QD585) and a 655/40 bandpass filter (for QD655) (Chroma). To achieve high time resolution imaging, a Hammamatsu OrcaFLASH sCMOS camera was used. Data was collected at 5 msec time resolution.

To image the WT/$AAA1_{K/A}$ heterodimer, a QD565/QD655 pair was used. The fluorescence was split by the same method, except a 580/60 filter was used to collect the QD565 emission. Because lower time resolution was desired, a 512x512 Andor Ixon EMCCD camera was used (DeWitt et al., 2012). Data was collected at 15 msec resolution.

To image WT dynein labeled with a single QD655 at high time resolution, I used the same setup as for the two-color experiments, but only the QD655 channel was used. Data was collected at 2 msec time resolution.

3.6.3 Two-Color QD Labeleing and Motility Assays

Samples of GS and WT homodimeric dynein were prepared for two-color imaging essentially as described in Chapter 2 (DeWitt et al., 2012). 1 µL of ~500 nM dynein was labeled with a ~0.5 µL each of ~5 µM QD585-HaloTag and QD655-HaloTag, for ~10 minutes. QDots were coated with HaloTag-NHS ester as described in Chapter 2 (DeWitt et al., 2012). 10 µL ~10 nM labeled dimers were flowed onto surface-immobilized MTs, prepared as described (DeWitt et al., 2012). Imaging on immobilized MTs was performed using DLBC buffer (80 mM HEPES pH 7.4, 1 mM EGTA and 2 mM $MgCl_2$, 10% glycerol), 1mg/mL Casein) with ATP regeneration and 10 mM β-mercaptoethanol as described in Chapter 2. Images from the sCMOS camera were collected at 5 msec frame time, in the presence of 7.5 µM ATP. Generally, ~300 mW laser power was used to achieve sufficiently bright imaging.

Samples of the WT/$AAA1_{K/A}$ heterodimer were prepared for two-color imaging similarly to the WT/$AAA1_{E/Q}$ heterodimer described in the Chapter 2 (DeWitt et al., 2012). Briefly, 1 µL each of ~500 nM WT and $AAA1_{K/A}$ heterodimers were dimerized with 1 µL 600 nM rapamycin in DLB for 5 minutes. 1 µL of the dimerization mixture was subsequently reacted with 1 µL of Streptavidin-coated QD655 and 1 µL HaloTag-coated QD565. ~10 nM labeled heterodimers were flowed onto immobilized MTs prepared and imaged as deseribed in Chapter 2 (DeWitt et al., 2012), in the presence of 1 mM (saturating) ATP.

3.6.3 Image Registration

Two-color images were registered using the technique outlined in detail in Chapter 1 and Chapter 2 (DeWitt et al., 2012). These chapters contain detailed protocols, and a more elaborate discussion of potential sources of registration error and how best to avoid them. Chapter 2 contains details on the microscope setup and software as well.

Briefly, after movies were collected as described above, two maps were constructed. A primary map was constructed from scanning of sub-diffraction nanoholes, imaged using brightfield illumination. Diffraction-limited spots arising from these nanoholes were localized to ~1 nm accuracy and paired. Pairs were used to construct a map that relates a point in one fluorescent channel to the other.

Primary maps from nanoholes were calculated as described (DeWitt et al., 2012) and as follows: The CCD surface was broken into 25-100 cells. A map of each cell was constructed using that cell's colocalizations and a polynomial transformation. Individual cells were connected using splines to make a continuous map of the entire CCD surface using nanoholes. Second order corrections were determined by imaging and localizing custom-made dual-labeled fluorescent probes to avoid chromatic aberration. Second order maps were constructed from the primary map, using ~10,000-100,000 fluorescent colocalizations and polynomial transformation. When a subset of localizations were reserved, they could be re-mapped to ~3 nm accuracy (Churchman et al., 2005; DeWitt et al., 2012). A second-order map was constructed from probes that were isospectral to the QDot pairs used. For the WT and GS experiments, this was the Rhodamine Red X-QD655 conjugate described previously. ~1 nM fiducials were imaged in DLB with trolox, PCA, and PCD (Aitken et al., 2008; DeWitt et al., 2012; Rasnik et al., 2006). For the WT/$AAA1_{K/A}$ heterodimer, a Cy3-QDot 655 conjugate was prepared in a similar manner by reacting ~1 mM Cy3 NHS with ~8 µM QDot 655-NH_2 (Life Technologies) for ~3 hours in DLB, followed by purification by spinning through a 30k MWCO spin filter (Millipore, Inc.). Imageing of these novel new fiducials

was performed in an identical manner as previously. Generally, a 0.2-0.5 second exposure was used, and aimaged through a 532 nm laser at 10-50 mW power, to collect ~5000 colocalized spots. For this study, spots from the second-order fiducials were picked and localized using the Insight Software package (Huang et al., 2008; Rust et al., 2006), while spots for fiducials from the first order map were picked and localized with custom-written software (DeWitt et al., 2012). Once compiled, colocalizations from first- and second-order maps were used to generate a final map, that could be directly applied to the traces from the two-color motility assays described above.

3.6.4 Two-Color Data Analysis

QD positions in each channel were determined using fluorescence tracking as described (DeWitt et al., 2012; Reck-Peterson et al., 2006; Yildiz and Selvin, 2005), using a two-dimensional Gaussian trakcing algorithm in MATLAB. Tracking algorithms are discussed in more detail in Chapter 1. The average errors were 5 nm for the WT and GS homodimers (imaged at 5 msec), and 3 nm for the WT/AAA1$_{K/A}$ heterodimer.

The traces were overlaid using the maps generated as described above, then aligned using principle component analysis. Steps were identified using a newly developed Schwartz Information Criterion (SIC)-based algorithm, that determines the number of steps in the trace using fluctuation analysis, and then fits the traces to a stepping function with that number of steps (Kalafut and Visscher, 2008). All steps were then verified by eye, including the presence of sideways steps, which were all added in manually.

3.6.5 One-Color Motility Assays and Data Analysis

To collect the step size and dwell time of cytoplasmic dynein at saturating ATP, extremely high spatiotemporal resolution is required. I used 2 msec time resolution and very high incident 488 nm illumination for this purpose (~500-1000 mW).

Samples were prepared otherwise identically to one-color tracking samples from head-labeled dyneins in Chapter 2 (DeWitt et al., 2012). Briefly, the same Dyn1$_{331kD}$ ("WT dynein") as was used for the two-color experiment was used in this assay, and it was labeled in the same manner, except on the QD655-HaloTag was used. This WT-QD655 conjugate was immobilized on sea urchin axonemes as described (DeWitt et al., 2012; Reck-Peterson et al., 2006) and imaged using the sCMOS camera at 2 msec time resolution in the presence of 1 mM ATP. Resulting traces were fit using the SIC step finder to extract dwell times and step sizes, presented in Fig. 3.4.

CHAPTER 4. THE AAA3 DOMAIN OF CYTOPLASMIC DYNEIN ACTS AS A "SWITCH" TO FACILITATE MT RELEASE

4.1 Summary

The work presented in Chapters 2 and 3 uncovered the basic stepping mechanism of cytoplasmic dynein. Missing from these studies is the role of the auxiliary ATPase sites in the motor head. I address this role here.

Unlike other cytoskeletal motors, the motor domain of dynein is composed of multiple ATPase subunits. AAA1 serves as the primary site for ATP hydrolysis and powers motility and force generation. AAA3 is also essential for robust motility, but its precise role in dynein's mechanochemical cycle remains unknown. Here, I show that dynein mutants defective in AAA3 ATPase activity do not release from the MT, and loss of AAA3 function makes MT release rate-limiting. Using single-molecule enzyme inhibition, I show that the AAA3 domain hydrolyzes nucleotide approximately 15 times slower than AAA1; therefore the two sites do not coordinate during stepping. These results show that AAA3 acts as a "switch" to regulate dynein motility, and suggest mechanisms of biophysical re-purposing of dynein by adaptor proteins such as LIS1.

4.2 Introduction

Despite performing similar tasks, cytoplasmic dynein and kinesin share several key differences. The two motors do not share a common ancestor in eukaryotes. The dynein heavy chain gene is very large (~500 MDa in some species, compared to <100 kDa for most kinesins). Perhaps not by not by coincidence, most cell have only a single dynein heavy chain gene, responsible for a wide variety of tasks in cell division and cargo transport (Roberts et al., 2013; Vallee et al., 2012). In contrast, cells have many kinesin genes, one for each task. Attachment of diverse cargoes is controlled by a multitude of adaptor proteins which primarily bind to the tail domain of dynein, which is dispensible for motility (DeWitt et al., 2012; Gennerich et al., 2007; Reck-Peterson et al., 2006). In contrast, alteration of dynein's biophysical properties is accomplished by regulatory proteins such as LIS1, NUDE and the dynactin complex, which directly bind to the motor domain and alter its biophysical properties (Kardon and Vale, 2009; McKenney et al., 2010; Vallee et al., 2012).

At the core of the 1.2 MDa dynein complex lies a homodimer of two ~500 kDa dynein heavy chains, which contain catalytic and mechanical elements required for motility (Mocz and Gibbons, 2001; Reck-Peterson et al., 2006; Toba et al., 2006). The heavy chain consists of an N-terminal dimerization and cargo-binding domain, connected through a long flexible linker to a pseudo-hexameric AAA+ (ATPases associated with various cellular activities) domain, with six non-identical AAA domains (AAA1-AAA6). Between AAA4 and AAA5 there protrudes a long (~15 nm) coiled-coil stalk, bearing a small globular MT-binding domain (MTBD) (Burgess et al., 2003) (Fig. 4.1A).

Conformational changes in the distal MTBD and linker domains that drive motility arise from ATP hydrolysis-dependent conformational changes within the AAA+ ring. A major source of confusion is the role of the six AAA domains (Fig. 4.1a). Of these, only AAA1, AAA2, AAA3, and AAA4 can bind nucleotide, while AAA5 and 6 do not have the conserved Walker A and B motifs required for ATP hydrolysis (Kon et al., 2004, 2012). AAA1 is the primary site of ATP hydrolysis (Kon et al., 2012). ATP binding to AAA1 induces MT release via helix sliding within

the coiled-coil stalk (Gibbons et al., 2005; Imamula et al., 2007; Kon et al., 2009). ATP hydrolysis at AAA1 induces linker undocking, or the "priming stroke" (Kon et al., 2005; Roberts et al., 2009), followed by re-binding to the MT and re-docking of the linker via a "power stroke" (Roberts et al., 2009, 2012), which is proposed to generate force required for dynein motility (Gennerich et al., 2007; Roberts et al., 2009, 2013).

The role of the other AAA domains remains unclear. ATPase mutations to AAA2 and 4 have a minor effect on the velocity and processivity of dynein (Cho et al., 2008; Kon et al., 2004). In contrast, AAA3 is essential for robust motility, and is well conserved in cytoplasmic dyneins, but not in axonemal dyneins (Andrew Carter, personal communication). Mutations to either ATP binding or hydrolysis at AAA3 reduce motor velocity more than 10-fold (Cho et al., 2008; Kon et al., 2004) and show defects in AAA1-generated linker swing (Kon et al., 2005). AAA3 mutants strongly localize to MT *in vivo* (Silvanovich et al., 2003) and slowly release from in the presence of ATP *in vitro* (Imamula et al., 2007). Despite being a vital secondary ATP hydrolysis site in cytoplasmic dynein, the precise role of the AAA3 domain within dynein's mechanochemical cycle remains unclear (Imamula et al., 2007; Kon et al., 2012).

In this study, I tested whether ATP hydrolysis at AAA3 is required to generate each step, or plays a regulatory role in dynein motility. Using MT-stimulated ATPase and single-molecule motility assays, I show that an active AAA3 site is required for AAA1-dependent control of cyclic MT attachment anddetachment cycle during processive motility. To analyze coordination between the AAA1 and AAA3 nucleotide cycles, I tracked individual dynein motors in the presence of saturating ATP and various concentrations of a slowly-hydrolyzable ATP analog, ATPγS. The density of analog-induced pauses increased with analog concentration. By analyzing the density of pauses versus analog concentration, I determined that a dynein dimer has two sites, one on each monomer, which must bind ATPγS to initiate a pause. Surprisingly, ATP-binding mutants of AAA3 are insensitive to ATPγS, indicating that pausing is initiated by analog binding to AAA3 only, and not AAA1. In the presence of equimolar ATP and ATPγS, a heterodimeric dynein with only one AAA3 site takes many successive fast steps between long pauses. This result shows that AAA3 does not hydrolyze ATP in concert with AAA1 to drive dynein stepping, as AAA1 can direct many rapid steps before AAA3 can be re-inhibited. Instead, it acts as a switch, allowing AAA1-directed MT release when "on" and preventing it when "off", depending on its nucleotide state.

4.3 Results

4.3.1 AAA3 Lifts an "MT Gate" to Robust Motility

Previous studies showed that ATP binding and hydrolysis mutants of AAA3 show dramatically increased run time despite >10 fold decreased velocity (Cho et al., 2008; Kon et al., 2004). These changes in dynein motility may be related to their strong MT affinity and the inability of AAA1 to control detachment from MTs. To test this, MT affinity was reduced by increasing the salt (KCl) concentration, and measured the velocity of both wild-type and AAA3 mutant motors. I used a minimal processive dynein from *S. cerevisiae* (GST-Dyn1$_{331kD}$, referred to as WT in this chapter), which is truncated at the N-terminus and artificially dimerized with glutathione S-transferase (GST). This motor has nearly identical motile properties to full-length dynein (DeWitt et al., 2012; Reck-Peterson et al., 2006). ATP binding to AAA3 was blocked by a point mutant in the Walker A loop of the AAA3 nucleotide binding site (AAA3$_{K/A}$) (Imamula et al., 2007; Kon et al., 2004).

I labeled the motors with a tetramethylrhodamine (TMR) dye at the N-terminus and monitored their motility along surface-immobilized microtubules using total internal reflection fluorescence (TIRF) microscopy. The velocity and run length of the motors was determined at 0-200 mM KCl (Figs. 4.1A, 4.1B, and 4.2), which reduces the affinity of dynein for MTs. I found that the velocity of WT dynein increased by ~20% with a small amount (20 mM) of added KCl, but the velocity decreased back to no-salt levels at higher (>75 mM) concentrations (Fig. 4.1A and 4.1C). In contrast, the velocity of $AAA3_{K\text{-}A}$ monotonically increased with added salt. At 150 mM KCl, the velocity (42 nm/s) was 2.5-fold greater, compared to the no-salt condition (14 nm/s) (Figs. 4.1B and 4.1D). These data indicate that MT detachment is rate-limiting in the absence of a functional AAA3 domain, but not in WT dynein. Run lengths for both WT and $AAA3_{K\text{-}A}$ decreased with added salt, consistent with reduced MT affinity (Fig. 4.2).

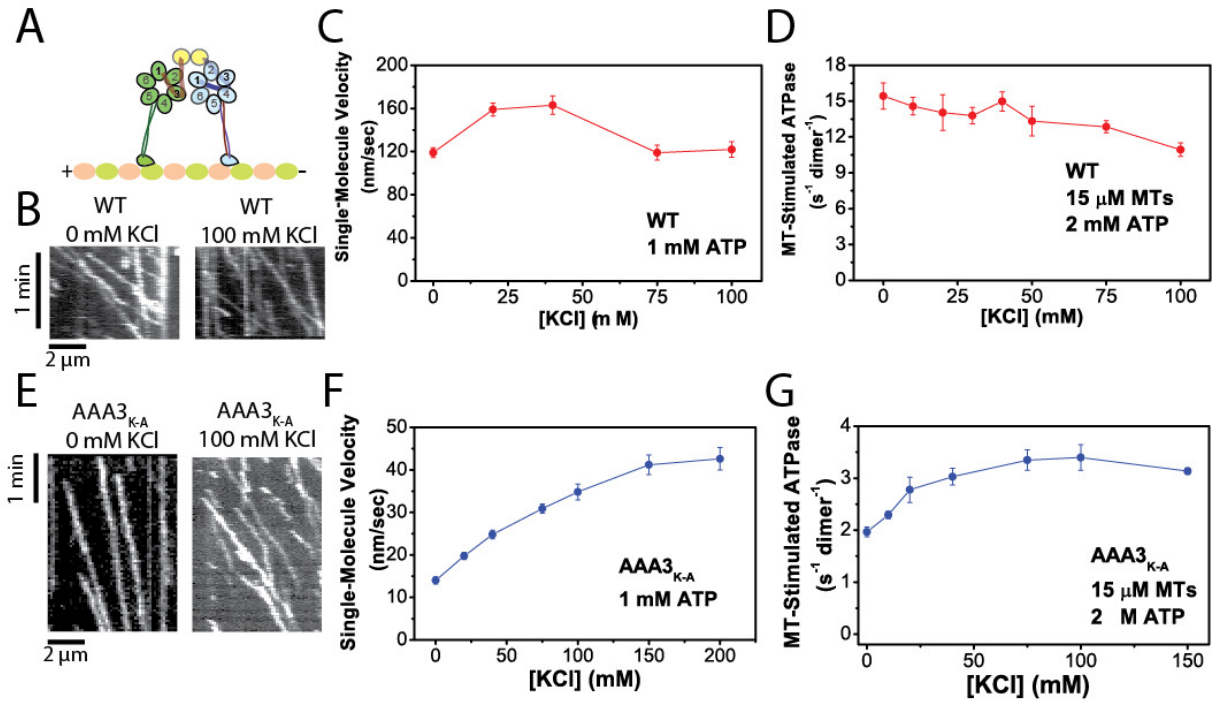


Figure 4.1. ATP binding mutants at AAA3 are gated by MT release. A) Schematic of Cytoplasmic dynein. Hydrolysis at AAA1 is strictly required for motility, while AAA3 Walker mutations are drastically slower than WT. B) Kymographs of tetramethylrhodamine (TMR)-labeled WT dynein. C) Single-molecule velocity of WT dynein in the presence of 1 mM ATP and 0-100 mM KCl. Velocity is measured using TMR-labeled dynein and kymography. The velocity is not substantially affected by salt, which reduces MT affinity. D) MT stimulated ATPase of WT dynein vs. added KCl. ATPase decreases slightly as MT affinity is decreased with added salt. E) Kymographs of $AAA3_{K\text{-}A}$ showing marked increase in velocity at high KCl concentration. F) Velocity of $AAA3_{K\text{-}A}$ ATP binding vs. added KCl. The $AAA3_{K\text{-}A}$ mutant velocity increases ~2.5-fold in the presence of added KCl, indicating that MT release is rate-limiting. G) MT-stimulated ATPase of $AAA3_{K\text{-}A}$ dynein vs. added KCl. ATPase increases by ~50% with added KCl, indicating that hydrolysis at AAA1 is also gated by MT release.

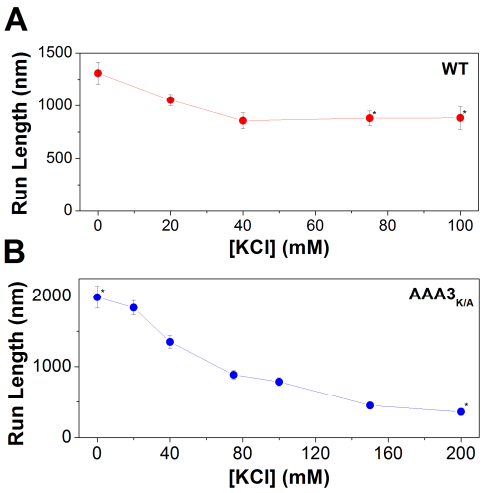


Figure 4.2. Run lengths of WT and $AAA3_{K/A}$ dynein vs. added KCl. See main text for experimental details. "*" indicates approximate value. A) Run length of WT decreases with added salt. Limited ability to measure very short, fast runs ("*") increases observed run lengths. B) Run length of $AAA3_{K/A}$ dynein with added salt. Very long-lived and very short-lived runs were difficult to measure accurately.

Mutations that inhibit nucleotide binding or hydrolysis at AAA3 also decrease the MT-stimulated ATPase rate of dynein, indicating that the rate of ATP hydrolysis at AAA1 is affected by AAA3 (Cho et al., 2008; Kon et al., 2004). This would occur if both sites coordinate directly to generate full-WT stepping; mutations at AAA3 will inhibit AAA1 hydrolysis as well. Alternately, the hydrolysis cycle of AAA1 may stalled or slowed down indirectly, because AAA1 cannot control the release of dynein from the MT in the absence of an active AAA3 domain. To examine this, I measured the MT-stimulated ATPase of WT and $AAA3_{K\text{-}A}$ dynein in the presence of added KCl and saturating MTs (Figs. 4.1E, 4.1F, and 4.3). Added salt increases the $K_{M(MT)}$ by up to 8-fold for WT dynein and 19-fold for $AAA3_{K/A}$ dynein, consistent with decreased MT affinity with added salt (Fig. 4.3).

The $AAA3_{K/A}$ mutant MT-stimulated ATPase increased with added KCl by 42%, from 2 $sec^{-1}dimer^{-1}$ to 3.4 $sec^{-1}dimer^{-1}$ at 100 mM added KCl, while the ATPase rate of WT decreased by 27%. The increase observed for the $AAA3_{K/A}$ mutant is consistent with AAA1 gating by MT-detachment. Disruption of the AAA3 hydrolysis cycle disrupts MT detachment, which in turn slows down hydrolysis at AAA1. As the "MT gate" is lifted with added salt, AAA1 hydrolysis speeds up, resulting in increased velocity of the $AAA3_{K/A}$ mutant.

Reducing the MT affinity of $AAA3_{K/A}$ with salt does not increase the velocity (42 nm/sec) and ATP hydrolysis rate (3.4 $s^{-1}dimer^{-1}$) up to that of WT (120 nm/sec and 15 $s^{-1}dimer^{-}1$, respectively) for WT with no salt before processivity was lost (Figs. 4.1 and 4.2). This can be explained by the fact that dynein requires proper timing of strong and weak MT affinity orchestrated with the force generation cycle for full WT motility. In comparison, salt addition reduces MT affinity in all nucleotide states, hence results in partial recovery in dynein motility before processivity is lost.

These results show that AAA3 gates AAA1 via control of release from the MT. However, it is not clear whether AAA3 and AAA1 coordinate directly to do so.

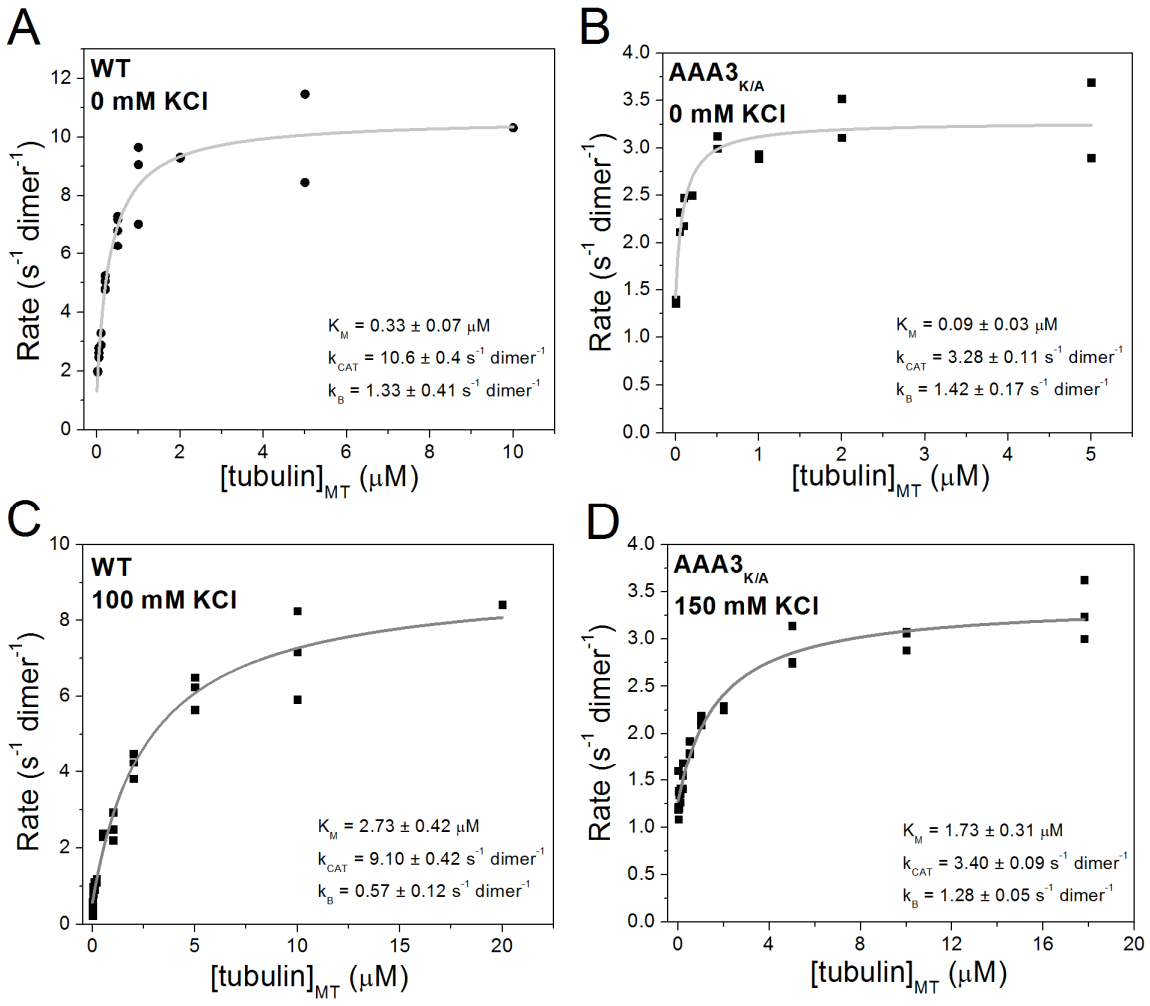


Figure 4.3. ATPase vs MT concentration ([tubulin]$_{MT}$) for WT and AAA3$_{K/A}$ dynein at no salt and high salt is consistent with reduced MT affinity at high salt. A) ATPase vs MT concentration for WT dynein with no added salt. B) ATPase vs MT concentration for AAA3$_{K/A}$ dynein with no added salt. C) ATPase vs MT concentration for WT dynein with 100 mM added KCl, the maximum amount used in motility and ATPase assays. C) ATPase vs MT concentration for AAA3$_{K/A}$ dynein with 150 mM added KCl, the maximum amount used in motility and ATPase assays.

4.3.2 ATPγS-Induced Pausing Behavior of WT Dynein

I next investigated the role of AAA3 in dynein's mechanochemical cycle. In order to distinguish whether the ATP hydrolysis at AAA3 coordinates with AAA1 per step of dynein, I conducted single-molecule enzyme inhibition assays using a slowly-hydrolyzable ATP analog, ATPγS in motility assays (Chemla et al., 2005; Sen et al., 2013). WT dynein was labeled with a bright quantum dot to track the motility of single motors at high resolution for several minutes without photobleaching (DeWitt and Yildiz 2014), in the presence of saturating (1 mM) ATP. The addition of 0-100 μM ATPγS reduced the overall velocity of the motors and the traces of single molecule show that the movement was interrupted by transient pauses (Fig. 4.4A).

As the concentration of ATPγS increased, both the frequency (Fig. 4.4A-C) and duration (Fig. 4.3D) of pausing increased. For each concentration of ATPγS tested, the pause density (PD) was calculated in a model-free manner by splitting each trace into 50 nm bins, and calculating the time spent by the motor in each bin, which is related to the velocity (Fig. 4.4B top, Fig. 4.5). A histogram of these dwell times has two distinct populations, both of which are exponentially

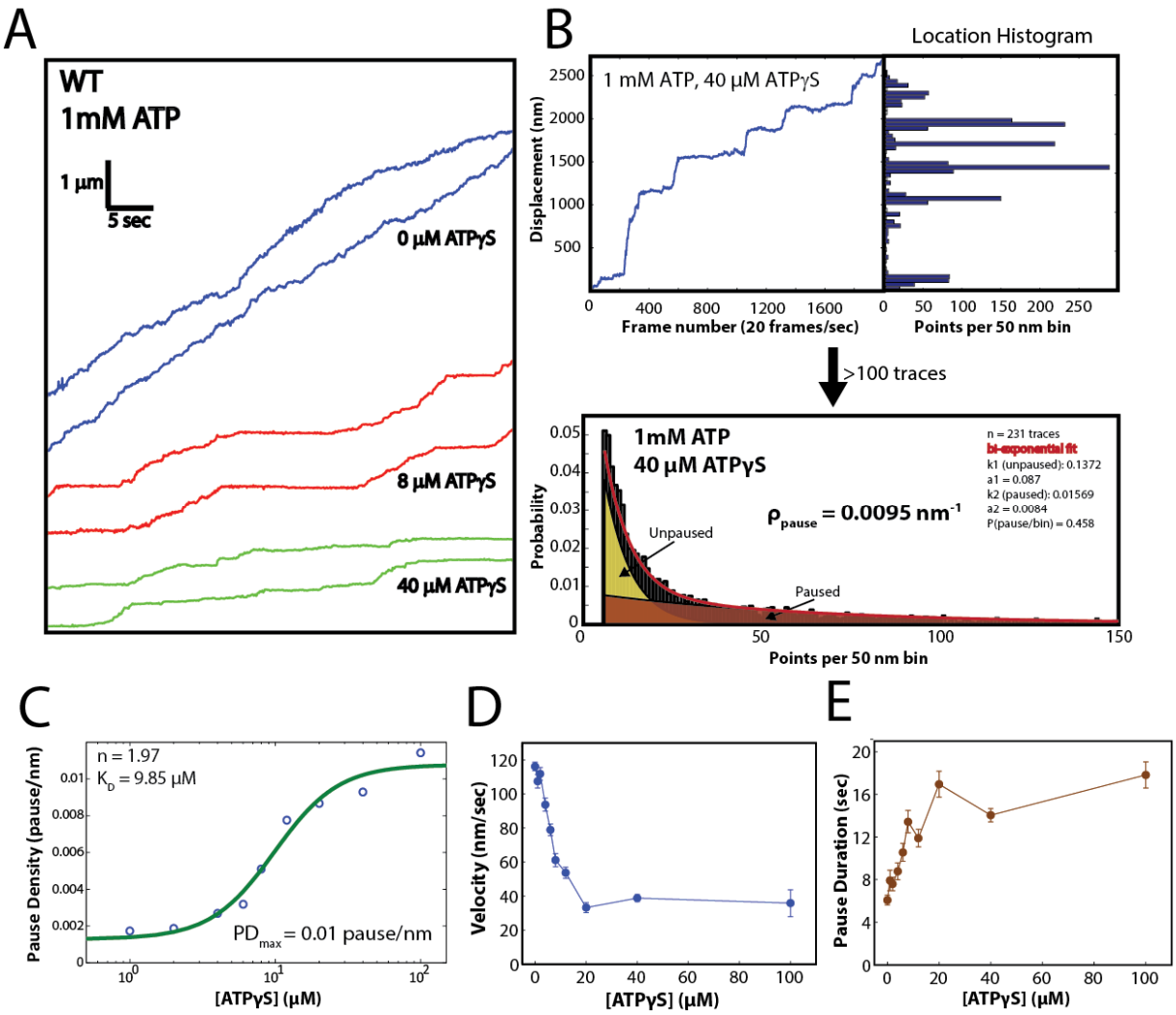


Figure 4.4. Single-molecule enzyme inhibition of WT dynein indicates that dynein must bind two inhibitors to pause motility, and that the site of inhibition is distinct from the site of stepping. A) Representative traces fluorescent tracking traces of WT dynein in the presence of 1 mM ATP and varying amounts of ATPγS inhibitor. As the ATPγS concentration increases, the frequency of analog-induced pauses increases. B) Calculation of pause density (pause/nm) from single-molecule traces. Each of >100 traces are sliced along the displacement axis, and the number of datapoints in each bin are binned into a histogram. The pause density can be calculated by fitting this histogram to a biexponential function, as the area under the curve representing the paused population. C) Semi-log plot of pause density vs ATPγS concentration fit to the Hill equation for inhibitor binding. The hill coefficient of 2 is consistent with single-site inhibition on two uncoordinated heads. The PD_{MAX} of 0.01 pause/nm indicates that at saturating ATPγS dynein still will walk an average of 100 nm between pauses. D) Velocity vs ATPγS concentration. The velocity saturates at a relatively high velocity compared to AAA1 or AAA3 mutants. E) Pause Duration vs ATPγS concentration.

distributed: a "fast" population, and a "paused" population (Fig. 4.4B bottom, Fig. 4.5). This population shows clear saturation behavior at relative low (>20 µM) ATPγS concentrations (Fig. 4.5). The area under each curve was used to estimate the pause density (PD), including the pauses that are too brief to be observed directly (Sen et al., 2013).

To extract the binding parameters of ATPγS to dynein, a plot of PD versus ATPγS concentration (Fig. 4.4C) was fit by a modified Hill Equation (Chemla et al., 2005; Moffitt et al., 2009; Sen et al., 2013). The fit resulted in the Hill coefficient (n = 1.97), suggesting that 2 ATPγS molecules must bind to initiate a pause in dynein motility (Chemla et al., 2005; Sen et al., 2013). The dissociation constant (K_d) of ATPγS for WT dynein is 9.6 µM, indicating that analog binding at the site of inhibition is fully saturated at 100 µM. The maximum pause density of the motor, PD_{MAX}, is 0.01 pause/nm. In other words, the motor travels on average 100 nm between subsequent pauses. Given dynein's average step size of 6 nm(DeWitt et al., 2012; Reck-Peterson et al., 2006), dynein takes ~15 steps on average between pausing events at saturating analog concentrations.

The velocity of the motor does not saturate near 0 nm/s (Fig. 4.4D), but instead only slows

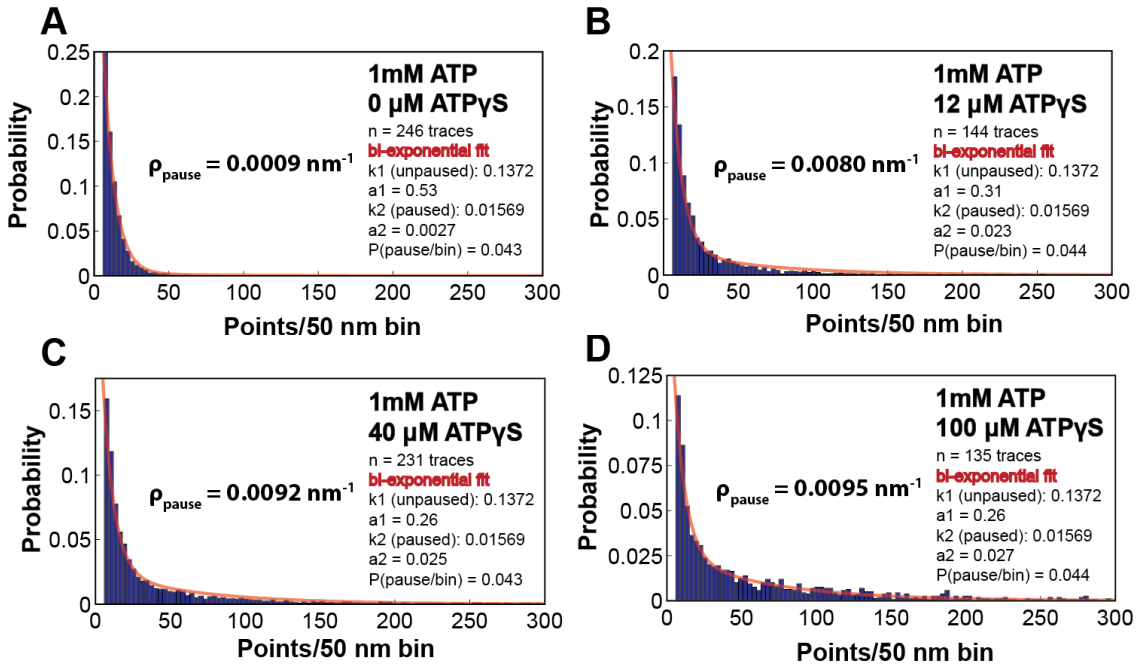


Figure 4.5. Histograms of the number of data points (acquired at 20 points/s) spent by the motor in 50 nm bins under different nucleotide conditions. When the motor is in a "fast" state, few points are found in each bin (large peak near 0 points/bin). When the motor is in a "paused" state, many points are found in a bin (long tail in the presence of ATPγS). When the paused population is saturated, a significant subpopulation of fast motors is still observed, indicating the presence of at least two long-lived states ("fast" and "paused") at saturation. Histograms are fit with a biexponential function. The amplitudes (a1 and a2) are used to calculate the size of the "paused" bin population (P(pause/bin)), which is proportional to the pause density (ρ_{pause}). See experimental procedures for analysis details. A) Points/bin histogram for 1 mM ATP, 0 µM ATPγS. The paused population is nearly non-existent. B) Points/bin histogram for 1 mM ATP, 12 µM ATPγS. There is a significant sub-population of paused motors. C) Points/bin histogram for 1 mM ATP, 40 µM ATPγS. D) Points/bin histogram for 1 mM ATP, 100 µM ATPγS. Despite a 2.5-fold increase in inhibitor, the pause density is not substantially increased over the 40 µM condition, indicating that the inhibitor nearly saturating.

4-fold to 30 nm/s (Fig. 4.4E). This finding, along with the low PD_{MAX}, suggests that when analog is saturating, the motor can still take long runs of fast motility. The low PD_{MAX} and non-zero velocity at saturation suggest that inhibition is not occurring at the site of stepping (AAA1), but must instead occur elsewhere.

4.3.3 ATPγS Specifically Inhibits the AAA3 Site

Pausing behavior, which is generated by binding of two ATPγS molecules to a dynein dimer, could arise from two possible causes: First, ATPγS can inhibit either of the AAA1 and AAA3 sites on each head with nearly equal probability, and the two sites coordinate (inhibiting one inhibits both). Second, ATPγS may preferentially bind to one site on both heads to induce a

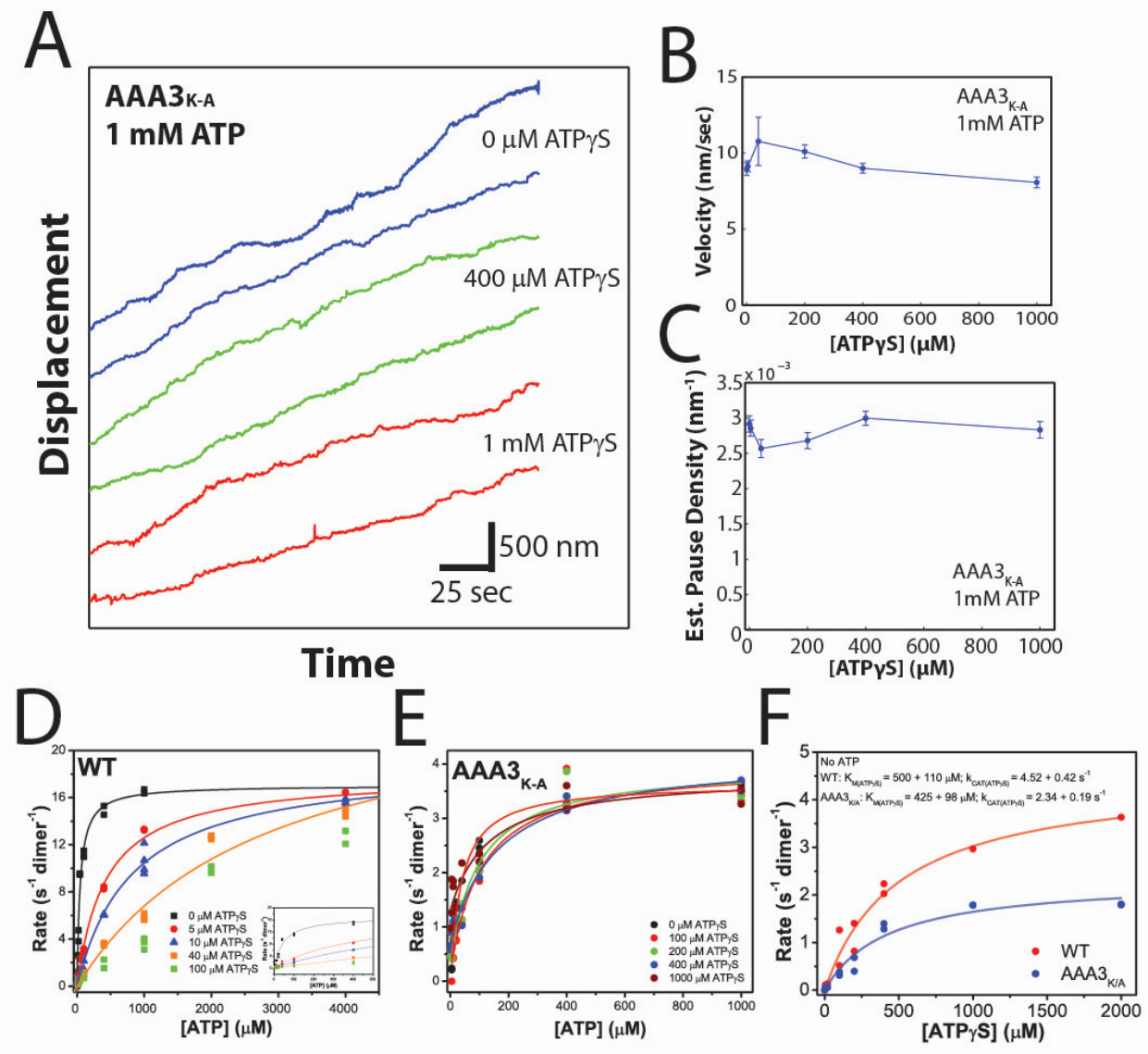


Figure 4.6. The $AAA3_{K/A}$ ATP binding mutant is insensitive to ATPγS. A) Representative tracking traces of Quantum Dot 655-tagged $AAA3_{K-A}$ dynein in the presence of high concentrations of ATPγS. B) Velocity of $AAA3_{K-A}$ dynein vs ATPγS concentration. C) Estimated pause density of $AAA3_{K-A}$ dynein vs ATPγS concentration, using a 5 nm/sec threshold. D) ATPγS induces dramatic increases in K_M of WT dynein, but no changes in k_{cat}, consistent with competitive inhibition. E) ATPγS does not inhibit $AAA3_{K-A}$ dynein. F) Hydrolysis of ATPγS in the absence of ATP. ATPγS is efficiently hydrolyzed by both constructs, but has weak affinity, consistent with poor inhibition of AAA1.

pause. In order to identify which sites are inhibited by ATPγS, I repeated the single molecule inhibition assays using the $AAA3_{K/A}$ mutant homodimer (Fig. 4.4A). Pause behavior was measured

at saturating ATP and 0-1000 μM ATPγS In the presence of 1 mM ATP with a $AAA3_{K/A}$ dynein homodimer (Fig. 4.6A). Surprisingly, I found that the velocity and pause density of these mutants were entirely unaffected by ATPγS at all concentrations tested (Figs. 4.6B and 3C). The results suggest that AAA1, which is the only remaining site necessary for motility in the $AAA3_{K/A}$ mutant, is insensitive to ATPγS. Therefore, ATPγS specifically inhibits AAA3 and both AAA3 sites in a dimer need to be inhibited to initiate a pause.

I confirmed this result in bulk using ATPase assays (Figs. 4.6D and 4.6E, and Table 1). I measured the apparent K_M and k_{cat} of WT and $AAA3_{K/A}$ dynein in response to 0-100 μM (for WT) or 0-1000 μM (for $AAA3_{K/A}$) ATPγS. I saw strong competitive inhibition of WT dynein at low analog concentrations. The K_M shifts from 46 μM in the absence of ATPγS to 694 μM in the presence of 10 μM ATPγS, while k_{cat} remains largely unaffected (17.0 s^{-1} vs. 16.5 s^{-1}). Measurement of k_{cat} is complicated by the extremely high K_M at elevated analog concentration (Table 1). As expected, $AAA3_{KA}$ is largely insensitive to ATPγS at concentrations of up to 1 mM, except for a comparatively minor shift in K_M. This shift will not affect motility at the 1 mM ATP concentration used in the single-molecule assays.

I also measured hydrolysis of ATPγS of WT and $AAA3_{KA}$ in the absence of ATP Fig. 4.6F). The hydrolysis rate of ATPγS is relatively fast at saturation (1.7 s^{-1} for $AAA3_{KA}$ and 3.4 s^{-1} for WT dynein), and the $K_{M(ATP\gamma S)}$ is ~10-fold higher than $K_{M(ATP)}$ for both constructs (400-500 μM $K_{M(ATP\gamma S)}$ vs. ~40 μM $K_{M(ATP\gamma S)}$) . These data suggest that hydrolysis of ATPγS is occurring at AAA1. Given the high K_M and high k_{cat}, it is apparent that ATPγS is a poor inhibitor of AAA1, with low affinity, and a short residence time.

Table 1. Summary of WT and $AAA3_{K-A}$ dynein enzymological properties in the presence of ATPγS.

Dynein	**[ATPγS] (μM)**	**$K_{M(App)}$**	**$k_{cat(app)}$**	**$v_{ATP\gamma S}$**
WT	0	46.2 ± 4.9	17.0 ± 0.5	--
	5	434 ± 49	17.5 ± 0.8	--
	10	694 ± 92	16.5 ± 1.1	--
	40	730 ± 150	10.3 ± 1.1	--
$AAA3_{K-A}$	0	38.4 ± 3.2	3.65 ± 0.08	0 (fixed)
	100	106 ± 36	4.00 ± 0.29	0.14 ± 0.20
	200	101 ± 25	3.99 ± 0.21	0.38 ± 0.13
	400	165 ± 40	4.18 ± 0.23	0.69 ± 0.09
	1000	130 ± 75	3.80 ± 0.18	1.31 ± 0.18

4.3.4 AAA3 and AAA1 Do Not Coordinate Their Hydrolysis Cycles

Our observation that ATPγS specifically inhibits AAA3, but not AAA1, provides a unique ability to investigate the role of AAA3 in dynein's stepping cycle. The low PD at saturating ATPγS concentration (0.01 pause/nm) for the WT homodimer (Fig. 4.4C) suggests that the AAA3 domain does can only be re-inhibited for every 15 steps of the motor (assuming ~6 nm per step), and therefore does not coordinate with AAA1. However, further analysis is complicated by the fact that WT has two sites of inhibition. The distribution of velocities of WT at different ATPγS concentrations suggests that inhibition is three-state (Fig. 4.7), dynein velo spectra).

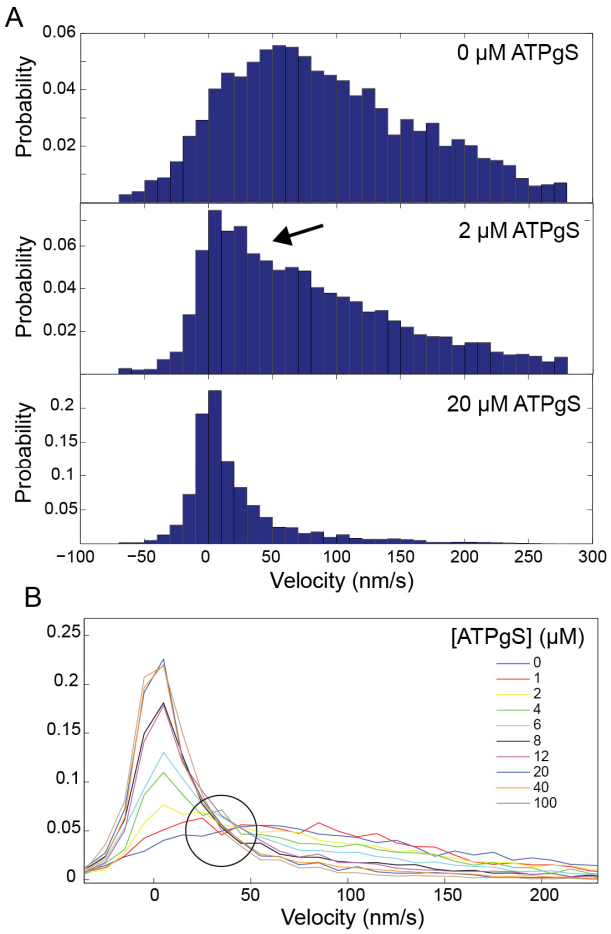


Figure 4.7. WT dynein shows signs of complex (>2 state) inhibition by ATPγS. A) Histograms of velocities for 1 mM ATP and 0, 2, and 20 µM ATPγS. As the analong concentration increases, the velocity decreases. Note the presence of an intermediate population of motors in the 2 µM ATPγS case (arrow). B) Overlay of normalized velocity histograms at all tested concentrations of ATPγS. The histograms do not intersect in a single "isosbestic point", which indicates that pausing of WT by ATPγS is >2 state. Given the Hill coefficient of ATPγS binding (n =1.97), WT dynein inhibition is likely 3-state (0-2 analogs bound to the motor).

To test our hypothesis, I measured the ATPγS-induced pausing behavior of a minimally processive dynein construct which has only one AAA+ ring (Fig. 4.8). The construct is a heterodimer of a WT monomer and a chimeric protein containing a seryl tRNA synthetase (SRS) domain fused to a dynein stalk-MTBD (SRS-WT heterodimer). The SRS domain holds the stalk-MTBD in a tight MT-binding conformation(Gibbons et al., 2005; Kon et al., 2009). This heterodimer is motile moving at 40% of the speed of the WT homodimer, similar to the speed of a WT/AAA1$_{E/Q}$ ATP heterodimer(DeWitt et al., 2012). Detailed characterization of this construct will be published elsewhere (Cleary *et. al.* unpublished). Since one of the heads was replaced with an inert protein, the SRS-WT heterodimer has only one AAA1 and one AAA3 site. If inhibition by ATPγS only occurs through the AAA3 domain, then this construct is expected to show simple two-state pausing behavior. If the AAA3 hydrolysis cycle is significantly slower than AAA1, the heterodimer should take extended fast runs between pauses, even at saturating ATPγS, and show signs of two-state inhibition. I labeled the WT head with a QDot, and tracked the motility of these constructs at 1 mM ATP and 0-100 µM ATPγS (Fig. 4.8A). As the concentration of analog increases, the motor slows (Fig. 4E) due to long pauses, similar to WT dynein (Figs. 4.8A, 4.8B).

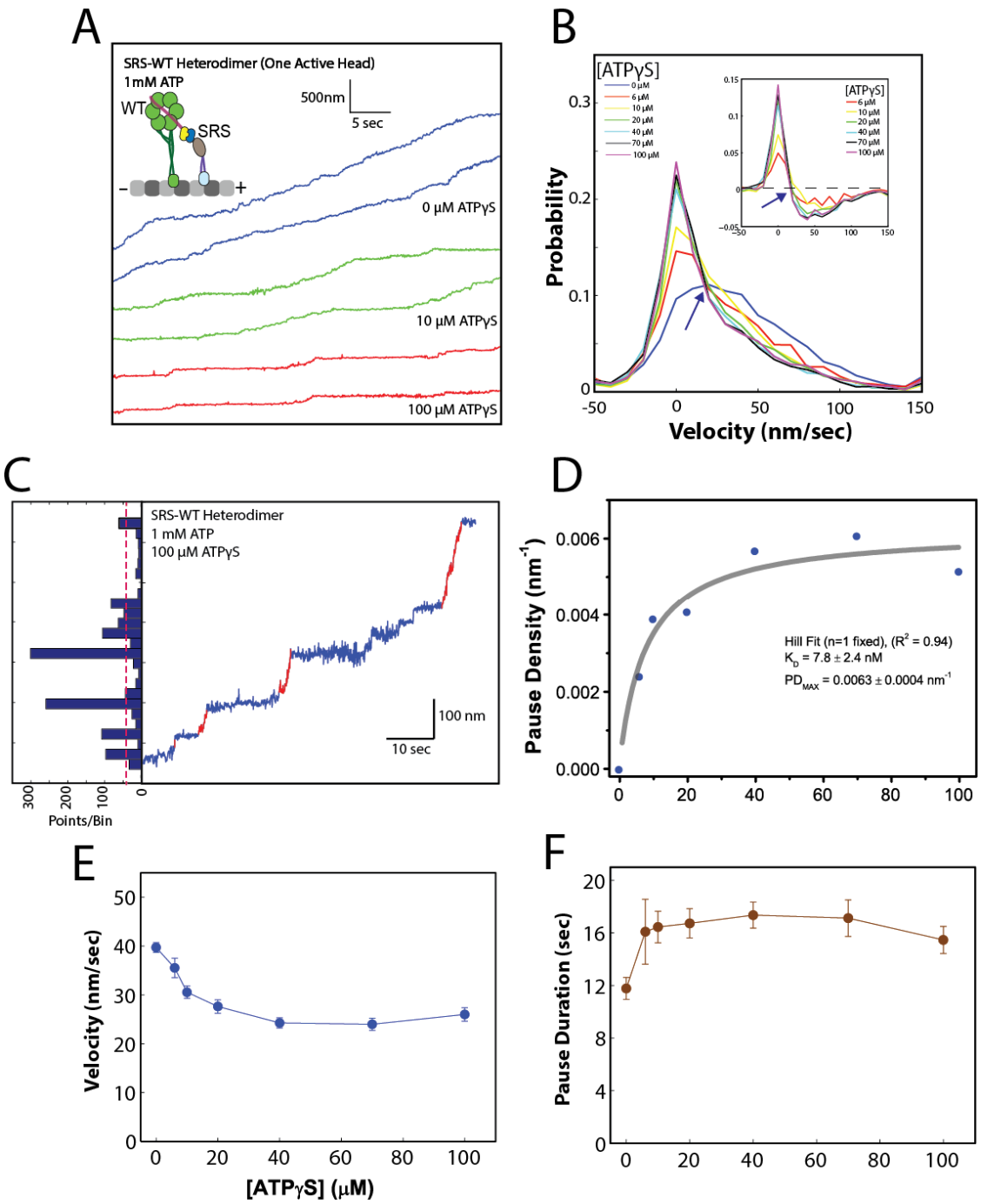


Figure 4.8 WT-SRS heterodimers with only one head (and a single AAA3 domain) show two-state pausing behavior in the presence of 1 mM ATP and varying ATPγS. These heterodimers can step rapidly for ~25 steps between pauses. A) Representative traces of Quantum Dot 655-tagged SRS-WT heterodimers in the presence of 0, 10, and 100 µM ATPγS. B) Velocity histograms over 1 second segments of the traces. Note the "isosbestic point" (blue arrows) in both the velocity histograms, and the velocity histograms with the 0 µM ATPγS histogram subtracted (inset), consistent with a simple two state transition from a "paused" to an "un-paused" state. C) Representative trace at 100 µM (saturating) ATPγS. Long runs of rapid stepping, as determined using a 15 nm/s velocity threshold, are shown in red. D) Hill fit of pause density vs ATPγS concentration. The pause density saturates at 0.0063 pause/nm. E) Velocity vs ATPγS concentration. F) Pause duration vs vs ATPγS concentration, calculated using a 15 nm/s velocity threshold.

As expected, the inhibition appeared to be a two-state. To illustrate this, I overlaid normalized histograms of motor velocity at different ATPγS concentrations (Fig. 4B). These "velocity spectra" intersect at a single "isosbestic point", indicating that inhibition is a two-state process (from a ~40 nm/s "fast" state to a ~0 nm/s "slow" state), consistent with specific inhibition of the lone remaining AAA3 site. Fitting of the pause density, calculated in a manner similar to WT, gives a PD_{MAX} of 0.0063 pause/nm (Fig. 4.8D). In other words, the motor pauses on average once every 153 nm, which corresponds to 25 steps. This is evident from traces of single motors at 100 μM (saturating) ATPγS (Fig. 4.8C). The motor embarks on fast runs for many steps between long-lived pausing events. These data are consistent with our hypothesis that AAA3 and AAA1 do not coordinate. AAA1 is already known to hydrolyze one ATP for every step of the motor, while AAA3 only hydrolyzes one nucleotide for every 25 steps (Cho et al., 2008; Imamula et al., 2007; Kon et al., 2004).The pause duration remains constant at all ATPγS concentrations tested (Fig. 4.8F), indicating that exit from a pause is a one-step process, due to release of the single bound analog.

4.3.5 ATP Hydrolysis at AAA3 is Slower Than Hydrolysis at AAA1

As a final confirmation that the AAA1 and AAA3 domains cycle at different rates, I analyzed pausing and motility at lower ratios of ATP:ATPγS. If AAA3 does not coordinate with AAA1 and hydrolyzes ATP much more slowly, fast runs between pauses should still be observed at very high ATPγS:ATP ratios . Conversely, if AAA3 hydrolyzes an ATP at every step of the motor, I expect to see on average of 1 step between the pauses in these conditions. I analyzed the pausing behavior at 200 μM ATP, 100 μM ATPγS (2:1 ATP:ATPγS, Fig. 5A) and 100 μM ATP, 100 μM ATPγS (1:1 ATP:ATPγS, 4.9B) to test this hypothesis. In both conditions the traces of single motors showed long runs (>10 fast steps) between pauses. In addition, the velocity, while reduced (Fig 4.9D), is substantially greater than the ~0 nm/s low speed peak of the "paused" population at 1 mM ATP (Fig. 4.9B). Selection of a 15 nm/s velocity threshold for "fast" motility indicated that the fast runs extend over 20 steps even at 1:1 ATP:ATPγS (Fig. 4.9D). Fast motility events remain frequent enough to contribute significantly to motility (0.03 and 0.02 pause/s for 2:1 and 1:1 ATP: ATPγS respectively, Fig. 4.9E). These results provide direct evidence that the AAA3 hydrolyzes ATP at a much slower rate than the stepping rate of dynein.

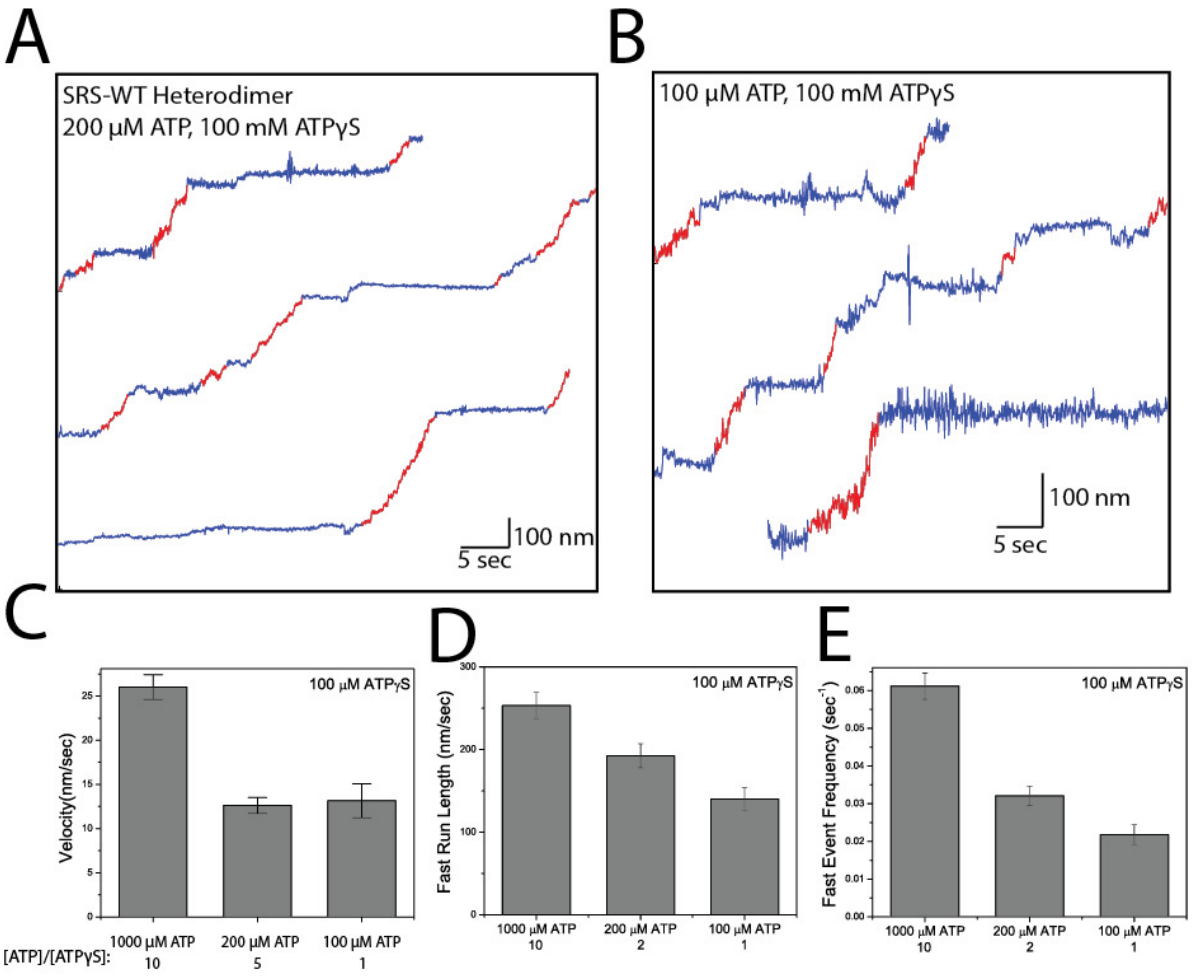


Figure 4.9. The SRS-WT heterodimer takes long runs between inhibitor-induced pauses, even at saturating inhibitor. A) Representative traces of Quantum Dot 655-tagged SRS-WT heterodimers in the presence of 200 µM ATP and 100 µM ATPγS. Long runs (>10 nm/s) are shown in red. B) Representative traces of Quantum Dot 655-tagged SRS-WT heterodimers in the presence of 100 µM ATP and 100 µM ATPγS. Long runs (>10 nm/sec) are shown in red. C) Velocity of SRS-WT heterodimers in the presence of 100 µM ATPγS and 1000-100 µM ATP. D) Lengths of runs of "fast" (>15 nm/sec) motility at 100 µM ATPγS and 1000-100 µM ATP. Fast runs were hand-picked using a >15 nm/sec threshold. The fast run length remains high (>100 nm) even at 1:1 ATP: ATPγS ratio. E) Frequency of "fast" motility events at 100 µM ATPγS and 1000-100 µM ATP.

4.4 Discussion

In this Chapter, I used single-molecule fluorescence and bulk enzymology to illuminate the role of AAA3 in dynein's mechanochemical cycle. AAA3 is decoupled from the motor, and acts as a quasi-static "switch" that allows or prevents AAA1-directed MT release. . MT release is rate-limiting when nucleotide binding is disrupted at AAA3 and this "MT gate" is lifted when MT affinity is decreased with added KCl. Single-molecule enzyme inhibition experiments with a slowly-hydrolyzable ATP analog, ATPγS, were used to elucidate coordination between AAA1 and AAA3. Analog addition resulted in transient pauses in dynein motility. Analysis of the pause density indicated that WT dynein must bind one ATPγS per head of the dimer, consistent with uncoordinated heads (DeWitt et al., 2012). AAA3 mutants of dynein are insensitive to ATPγS,

therefore the analog inhibits dynein by selectively binding the AAA3 domain, a result confirmed using ATPase assays. I conclude that one ATPγS must bind to each AAA3 site in the homodimer to initiate a pause. To investigate coordination between the AAA1 and AAA3 domains, the experiment was repeated with a heterodimeric dynein with a single AAA3 site. I found that inhibition of this heterodimer was clearly two-state, and long runs were frequent, even at near-equimolar analog, a result predicted from the WT experiment. Since the motor can take many fast steps before AAA3 is re-inhibited, I conclude that AAA3 does not coordinate with the site of primary hydrolysis at AAA1. Instead, AAA3 must exist in a long-lived post-hydrolysis state to allow AAA1 to direct release of the motor from the MT.

Evidence for the lack of coordination between the two sites was also evident in the WT inhibition experiment (Figs. 4.4 and 4.5). The PD_{MAX} for WT is 0.01 pause/nm or 100 nm between pauses (Fig. 4.4C). This implies that the motor can take 15 steps on average between pauses, similar to the 25 steps between pauses seen for the SRS/WT heterodimer. From the AAA3 experiment, it is apparent that ATPγS only inhibits at AAA1. Given this, if the AAA3 hydrolysis rate were similar to AAA1, the velocity of the WT motor should saturate near the velocity of the AAA3 mutant. However, WT velocity saturates at 35 nm/s, ~3-fold faster than the $AAA3_{K/A}$ and ~6-fold faster than a AAA3 ATP-hydrolysis mutant reported in the literature (~5 nm/s) (Cho et al., 2008). Therefore, it appears that AAA3 hydrolyzes nucleotide much slower than AAA1 in the WT motor as well as in the WT/SRS heterodimer, and the sites do not coordinate. However, AAA1 hydrolysis is still linked to the presence of an intact AAA3 domain, as demonstrated in Fig. 4.1.

I propose a "switch" model for the role of the AAA3 domain in the dynein mechanochemical cycle (Fig. 4.10). In the apo or ATP-bound state (mimicked by AAA3 ATP-binding and hydrolysis mutants), AAA1 cannot allosterically direct MT release through the ring (Cho et al., 2008; Kon et al., 2004, 2012). MT attachment in turn slows hydrolysis at AAA1, resulting in slow motility and persistent MT attachment. After hydrolyzing ATP at AAA3, the "switch" is on, and the allosteric circuit connects AAA1 to the distal sites of MT release. This "switch on" post-hydrolysis state (either ADP-P_i or ADP) persists for an average of ~15 steps of the motor, during which AAA1 can effectively direct MT release, which in turn allows the motors to move at full speed(Roberts et al., 2013). Eventual release of products at AAA3 turns the "switch" off until the next nucleotide cycle.

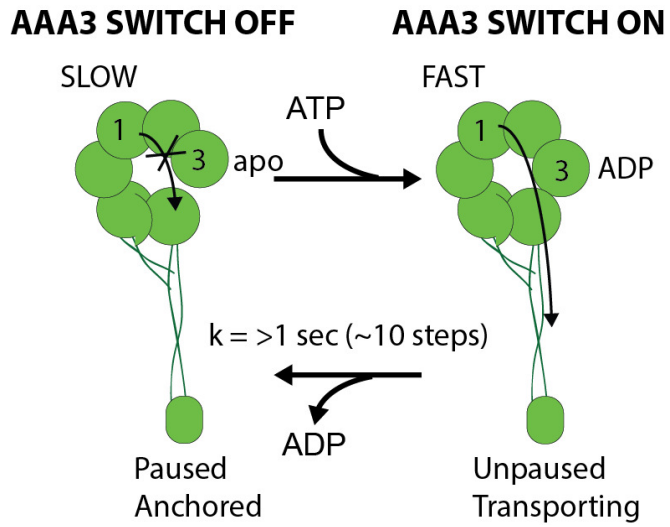


Figure 6. AAA3 acts as a "switch" to allow AAA1-directed MT release and robust motility. In the apo state, communication through the ring by AAA1 to the MTBD is blocked, possibly through altered ring conformation or conformational flexibility at AAA3. After ATP binding and subsequent hydrolysis the ADP- or ADP-P_i-bound AAA3 domain is competent to transmit allosteric MT release signals from AAA1.

A possible clue for the structural basis of the AAA3 switch comes from crystal structures of dynein and other AAA motors (Carter et al., 2011; Glynn et al., 2009; Kon et al., 2012; Lee et al., 2003; Schmidt et al., 2012; Zhang et al., 2000). In these motors, allosteric communication across the ring is believed to be driven by coupled rigid-body motions of the subunits. In dynein, it has been proposed that these motions originate with a ring-closing event at AAA1 (Carter et al., 2011; Schmidt et al., 2012). In this work, I find that AAA1 has a very low affinity for ATPγS, consistent with the open conformation seen in the crystal structures. It is possible that nucleotide-induced ring closing initiates a conformational change across the ring to the stalk-MTBD. This change requires a semi-flexible AAA3 domain, which only exists when AAA3 is in the post-hydrolysis state, the same state that is resistant to ATPγS inhibition.

Our model has implications for the role of the AAA3 site in dynein's cellular function. Dynein switches between a fast and slow motility based upon the nucleotide state of AAA3. It is possible that this switch can be regulated by external factors that specifically interact with the dynein motor domain. One clue comes from studies of the dynein adaptor protein LIS1, which binds to the AAA+ ring near AAA3 (Huang et al., 2012; McKenney et al., 2010). The LIS1-dynein complex also shows persistent MT attachment and bears a strong resemblance in its velocity to AAA3 mutants (Huang et al., 2012; McKenney et al., 2010). Interestingly, a similar phenotype can also be recapitulated by mutating the "sensor" arginine of AAA4 that reaches into the AAA3 ATP binding pocket (Huang et al., 2012). I speculate that the communication between the AAA1 site and the MTBD is mediated by AAA3 and that this communication may be blocked by LIS1 binding. LIS1 binding may this allosteric pathway either by blocking the accass of a nucleotide to AAA3 or by decoupling the conformational changes within the ring required for switching of the MTBD from a high-affinity to the low affinity state (Huang et al., 2012; Zhuang et al., 2007). This regulatory mechanism could potentially repurpose dynein from a cargo transporter, which requires the ability to synchronize the MT attachment/detachment cycle with force generation for robust motility, to an anchor, which requires stable attachment of the motor to a MT (Kardon and Vale, 2009; Yi et al.).

Further work is required to study the conformational changes within the AAA+ ring as a function of the nucleotide state of AAA3 and how dynein-associated proteins such as LIS1 or NUDE/NUDEL affect the dynamics of these, or to elucidate the mechanism of action of dynein-specific drugs such as ciliobrevin (Firestone et al., 2012; Huang et al., 2012; Markus et al., 2012; McKenney et al., 2010). The single-molecule approaches used here to elucidate the role of AAA3 can be readily applied to these questions as well.

4.5 Materials and Methods

4.5.1 Cloning and Molecular Biology

An N-terminal truncated *S. cerevisiae* cytoplasmic dynein gene (*DYN1*) encoding amino acids 1219-4093 (predicted molecular weight 331 kD, referred to as $Dyn1_{331kD}$) was used as a template for mutagenesis(Reck-Peterson et al., 2006). $Dyn1_{331kD}$ was artificially dimerized through an N-terminal GST tag (GST-$Dyn1_{331kD}$). N-terminal fusion proteins bearing either an N-terminal GFP and C-terminal HaloTag (Promega Biosciences) or an N-terminal HaloTag only (GFP-GST-$Dyn1_{331kD}$-HALO and HALO-GST-$Dyn1_{331kD}$) have both been shown to move at similar velocity and processivity to that of native yeast dynein (DeWitt et al., 2012; Reck-Peterson et al., 2006). I refer to these GFP-and HALO- tagged motor only as "WT" dynein in the main text, and describe the specific labeling strategies in detail here.

S. cerevisae expressing GST-homodimers based upon GFP-GST-$Dyn1_{331kD}$-HALO bearing a $AAA3_{K/A}$ (K1694A in GFP-GST-$Dyn1_{331kD}$-HALO) mutation that disrupts ATP binding were constructed by URA knock-in using standard PCR techniques and yeast transformation, followed by verification of proper insertion with colony PCR.

For the "SRS-WT" heterodimer, I used an *S. cerevisae* straing expressing a monomeric "WT"-like dynein construct bearing an N-terminal FRB domain in place of GST, as well as a C-terminal HaloTag (FRB- $Dyn1_{331kD}$-HALO), that had been constructed for a previous study (Reck-Peterson et al., 2006). This was paired with an *E. coli* BL21 strain expressing a chimeric "SRS" construct bearing a dynein stalk-MTBD, held in a tight binding 85:82 stalk registry, and a C-terminal FKBP domain from a pET42a vector (FKBP-$SRS_{85:82}$). The full description of and characterization of this construct is described elsewhere (Cleary *et. al.,* unpublished).

4.5.2 Protein Expression, Purification and Labeling

Dynein proteins were expressed in yeast and purified as described (Reck-Peterson et al., 2006). WT and $AAA3_{K/A}$ dynein were further purified by microtubule bind-and-release before use (DeWitt et al., 2012; Reck-Peterson et al., 2006; Yildiz et al., 2004a). Purified protein was stored in DLB (30 mM HEPES pH 7.2, 2 mM $MgCl_2$, 1 mM EGTA, 10% glycerol). Expression and purification of SRS-MTBD was carried out from *E.coli,* as described (Gibbons et al., 2005).
For measurement of single-molecule velocity in response to salt, WT dynein containing a C-terminal HaloTag were labelled with 10μM TMR HaloTag ligand (Promega) for 1 h on ice during the protein preparation, prior to washing of the IgG beads (GE Healthcare).

4.5.3 Microscope and Imaging

Single-molecule motility assays were performed on a custom-built objective-type total internal reflection fluorescence (TIRF) microscope, equipped with an inverted microscope body (Nikon Ti-Eclipse) with perfect focusing system, 1.45 NA 60X microscope objective (Nikon, TIRF Plan Apochromat). The sample was illuminated with 488 nm and 532 nm solid state lasers (Coherent) to image QDots and TMR, respectively. TMR-dynein was imaged to record the velocity of WT and $AAA3_{K/A}$ in response to added KCl. Movies of TMR-dynein were recorded with a 0.5-2 second exposure time under ~2 mW 532 nm laser exposure through a 580/60 bandpass emission filter. For high-resolution tracking of QDot-labeled dyneins in response to added ATPγS, ~100 mW 488 laser was used, with a 50 msec exposure time for QDot-labeled WT and WT-SRS

heterodimer and 50-100 msec exposure time for QDot-labeled $AAA3_{K/A}$ homodimer. QDot-dynein was imaged through a 655/40 bandpass emission filter. All movies were recorded using a water-cooled Hamamatsu ORCA-Flash4.0 sCMOS camera, and manufacturer software.]

4.5.4 Single-Molecule Motility Assays

Motility assays were performed largely as described (Reck-Peterson et al., 2006; Yildiz et al., 2004a). In all cases, sea urchin axonemes were immobilized on a glass coverslip in a flow camber constructed with double sided tape. The chamber washed with 15 µl of DLB (30 mM HEPES pH 7.2, 2 mM $MgCl_2$, 1 mM EGTA, 10% glycerol), followed by 15 µl of DLBC (DLB with 1 mg/ml casein, 2 mM DTT). 100-500 pM dynein was then perfused into the chamber in DLBC and allowed to bind to the axonemes for 1 minute. The flow cell was then washed with 45 µl DLBC (3 15 µl washes) followed by 20 µl of imaging buffer carrying the appropriate salt and nucleotide condition (see below).

4.5.5 Velocity of WT and $AAA3_{K/A}$ Dynein in Response to Salt

To measure the velocity of WT and $AAA3_{K/A}$ in response to salt, TMR-dynein slides were prepared and imaged as described above, and imaged in the presence of DLBC with 0-200 mM KCl, 25 mM PCA and 0.35 mg/ml PCD for oxygen scavenging (Aitken et al., 2008), 0.6 mM Trolox for triplet quenching (Rasnik et al., 2006), 2 mM phosphoenolpyruvate and 0.1 mg/mL pyruvate kinase to regenerate ATP, and 1 mM ATP. Velocities were measured using kymography. Because high salt reduces the affinity of dynein for the MT, the dynein concentration perfused into the sample was increased as necessary.

4.5.6 High-Resolution Tracking of WT, $AAA3_{K/A}$ Dynein Homodimers and WT/SRS Dynein Heterodimers in the Presence of ATPγS

To measure the pause behavior of WT and $AAA3_{K/A}$ dynein in the presence of ATPγS, 1 µL of dynein was pre-labeled with QDot 655. For WT dynein, 1 µL ~2 µM QDot 655 was labeled with 1 µL ~500 nM dynein (HALO-GST-$Dyn1_{331kD}$) for 10 minutes prior to dilution in DLBC and perfusion into the axoneme sample chamber. For $AAA3_{K/A}$, 1 µL ~1 µM anti-GFP antibody-coated QDot 655 was mixed with 1 µL ~500 nM mutant dynein (which has an N-terminal GFP). HaloTag ligand coated QDot 655 was prepared from HaloTag NHS (Promega) and amino-PEG QDot 655 as described (DeWitt et al., 2012). Anti-GFP QDot 655 was prepared with polyclonal rabbit anti-GFP and carboxy-coated QDot 655 using EDC crosslinking according to the manufacturer's protocol (Life Technologies).

To measure the pause behavior of the WT/SRS dynein heterodimer in the presence of ATPγS, heterodimers were constructed by mixing 1 µL of ~500 nM FRB- $Dyn1_{331kD}$-HALO was mixed with 1 µL of ~5 µM FKBP-$SRS_{85:82}$, 2 µL of 600 nM rapamycin to induce FRB-FKBPheterodimerization (Banaszynski et al., 2005; Kliegman et al., 2013), and 2 µL of DLB for 5 minutes. 2 µL of this mixture was labeled with 1 µL of HaloTag ligand-coated QDot 655 to label the heterodimer at the dynein C-terminus. Labeling continued for 10 minutes prior to dilution and perfusion into an axoneme sample chamber.

In all cases, QDot dynein was imaged as described above in an imaging buffer consisting of DLBC with 10 mM β-mercaptoethanol to prevent blinking (Hohng and Ha, 2004), 2 mM

phosphoenolpyruvate and 0.1 mg/mL pyruvate kinase to regenerate ATP, 100-1000 μM ATP, and 0-1000 μM ATPγS.

4.5.7 Pause and Fast Run Behavior Data Analysis

Pause density of dynein in the presence of ATPγS was calculated using a novel method as described in the text, based upon previously published methods (Sen et al., 2013). Movies of moving QDot-labeled dynein were tracked using a custom-written Gaussian mask algorithm. Resulting traces were aligned and reviewed (by removal of terminal pause events) using MATLAB (The Mathworks). To calculate pause density, the MT-axis component of each trace was binned into 50 nm segments (Fig 2B, top). The heights of bins (in datapoints) from >100 traces were used to construct a histogram of bin heights (Fig 2B, bottom). These histograms had a distinctly bi-exponential character, and the exponential portion was fit to a sum of two exponentials. $\rho_{bin} = \frac{a_2/k_2}{a_1/k_1 + a_2/k_2}$

where k_1 and k_2 describe the decreased probability of observing a given number of datapoints per bin for a totally un-paused and totally paused motor, respectively. The k_1 and k_2 values were fixed by iteratively fitting the most extreme ATPγS concentrations' histograms. In this context the pause density in pause/bin is given by the ratio of the areas underneath the two curves:

And so the pause density in nm^{-1} is given by

$$\rho_{nm} = \rho_{bin}/(bin\ size)$$

The pause density can be fit to a variant of the Hill Equation:

$$f = PD_{MIN} + \left(\frac{PD_{MAX} - PD_{MIN}}{1 + \left(\frac{K_D}{[ATP\gamma S]} \right)^n} \right)$$

In this context, K_D is the dissociation constant for ATPγS, PD_{MAX} is the pause density of saturating ATPγS, PD_{MIN} is the basal pause density (no ATPγS), and n is the number of ATPγS molecules that must bind to generate a pause (Chemla et al., 2005; Moffitt et al., 2009; Sen et al., 2013).

The velocity was calculated by dividing the total distance traveled by the time elapsed for an edited trace. The pause duration was calculated by counting the total number of data points in consecutive distance bins with a velocity through the bin less than a fixed threshold (<15 nm/sec for WT, <10 nm/sec for the WT/SRS heterodimer).

To characterize periods of fast motility for the WT/SRS heterodimer at 10:1, 2:1, and 1:1 ATP:ATPγS at 100 μM ATPγS, it was necessary to pick fast runs by hand. Datapoints in consecutive distance bins corresponding to fast motility (>10 nm/sec) were plotted, and approximate beginning and end indices were selected by hand. Hand-selected fast runs are plotted in Fig 5A and 5B. From these, the length of fast motility was calculated. The fast event frequency was calculated as the total number of fast events picked divided by the total distance traveled by all the traces at each nucleotide condition.

4.5.7 ATPase Assays

ATPase assays were carried out broadly as described, according to manufacturer's recommendations (EnzCheck Phosphate Assay, Life Technologies, and (Reck-Peterson et al., 2006)). A typical ATPase reaction consisted of DLB with 2-5 nM dynein (stock concentration determined using A495 of EGFP and ε_{EGFP} = 55,000 cm^{-1} M^{-1}), 200 nM MESG, 1 U/mL PNPase, 2 mM DTT, polymerized taxol-stabilized MTs with tubulin concentration as indicated, and ATP,

ATPγS, and 0-200 mM KCl as indicated in the text. Total reaction volumes were 100-150 µL per sample. Rates of P_i generation were measured using a plate reader set to record A360 at 60 second intervals against a buffer-only blank, and the maximum reasonable rate was selected. Rate in mOD/min was converted to turnover number (s^{-1} $dimer^{-1}$) using phosphate standards in similar buffer conditions.

MTs were prepared using standard techniques. Briefly, 3.5 mg/mL purified bovine tubulin in BRB80 (80 mM PIPES pH 6.8, 1mM $MgCl_2$, 1 mM EGTA) was polymerized by addition of 1 mM GTP, followed by stepwise addition of 1/10 vol each of 4 µM, 40 µM, and 400 µM paclitaxel (taxol) at 5 minute intervals. MTs were pelleted at >50,000 x g and resuspended in DLB prior to use in ATPase assays.

$K_{M(MT)}$ in the presence and absence of salt (Fig. 4.3) was calculated by fitting of rate vs ATPase at indicated salt concentrations with a single site basal ATPase equation (Kon et al., 2004):

$$k_{obs} = \frac{(k_{cat} - k_{basal})[MT]}{K_M + [MT]} + k_{basal}$$

MT-stimulated ATPase of dyneins in the presence of varying amounts of KCl were calculated by simple subtraction of simulataneously-measured k_{basal}. $K_{M(ATP)}$ in the presence of varying ATPγS was measured by fixing k_{basal} (ATPγS hydrolysis) at zero for all WT dynein conditions, and $AAA3_{K/A}$ dynein with no ATPγS.

REFERENCES

Agrawal, A., Deo, R., Wang, G.D., Wang, M.D., and Nie, S. (2008). Nanometer-scale mapping and single-molecule detection with color-coded nanoparticle probes. Proc Natl Acad Sci U S A *105*, 3298–3303.

Aitken, C.E., Marshall, R.A., and Puglisi, J.D. (2008). An oxygen scavenging system for improvement of dye stability in single-molecule fluorescence experiments. Biophys. J. *94*, 1826–1835.

Altman, R.B., Terry, D.S., Zhou, Z., Zheng, Q., Geggier, P., Kolster, R.A., Zhao, Y., Javitch, J.A., Warren, J.D., and Blanchard, S.C. (2012). Cyanine fluorophore derivatives with enhanced photostability. Nat. Methods *9*, 68–71.

Antelman, J., Wilking-Chang, C., Weiss, S., and Michalet, X. (2009). Nanometer distance measurements between multicolor quantum dots. Nano Lett. *9*, 2199–2205.

Asbury, C.L., Fehr, A.N., and Block, S.M. (2003). Kinesin moves by an asymmetric hand-over-hand mechanism. Science *302*, 2130–2134.

Ashkin, A., Dziedzic, J.M., Bjorkholm, J.E., and Chu, S. (1986). Observation of a single-beam gradient force optical trap for dielectric particles. Opt. Lett. *11*, 288.

Balci, H., Ha, T., Sweeney, H.L., and Selvin, P.R. (2005). Interhead distance measurements in myosin VI via SHRImP support a simplified hand-over-hand model. Biophys. J. *89*, 413–417.

Banaszynski, L.A., Liu, C.W., and Wandless, T.J. (2005). Characterization of the FKBP.rapamycin.FRB ternary complex. J. Am. Chem. Soc. *127*, 4715–4721.

Bartko, A.P., Xu, K., and Dickson, R.M. (2002). Three-dimensional single molecule rotational diffusion in glassy state polymer films. Phys Rev Lett *89*, 026101.

Betzig, E., Patterson, G.H., Sougrat, R., Lindwasser, O.W., Olenych, S., Bonifacino, J.S., Davidson, M.W., Lippincott-Schwartz, J., and Hess, H.F. (2006). Imaging intracellular fluorescent proteins at nanometer resolution. Science *313*, 1642–1645.

Bobroff, N. (1986). Position measurement with a resolution and noise-limited instrument," Rev. Sci. Instrum.57(6), 1152 –1157(1986). Rev. Sci. Instrum. *57*, 1152–1157.

Braslavsky, I., Amit, R., Jaffar Ali, B.M., Gileadi, O., Oppenheim, A., and Stavans, J. (2001). Objective-type dark-field illumination for scattering from microbeads. Appl. Opt. *40*, 5650–5657.

Burgess, S.A., Walker, M.L., Sakakibara, H., Knight, P.J., and Oiwa, K. (2003). Dynein structure and power stroke. Nature *421*, 715–718.

Burghardt, T.P., and Axelrod, D. (1981). Total internal reflection/fluorescence photobleaching recovery study of serum albumin adsorption dynamics. Biophys J *33*, 455–467.

Carter, A.P., Garbarino, J.E., Wilson-Kubalek, E.M., Shipley, W.E., Cho, C., Milligan, R. a, Vale, R.D., and Gibbons, I.R. (2008). Structure and functional role of dynein's microtubule-binding domain. Science *322*, 1691–1695.

Carter, A.P., Cho, C., Jin, L., and Vale, R.D. (2011). Crystal structure of the dynein motor domain. Science *331*, 1159–1165.

Cheezum, M.K., Walker, W.F., and Guilford, W.H. (2001). Quantitative comparison of algorithms for tracking single fluorescent particles. Biophys J *81*, 2378–2388.

Chemla, Y.R., Aathavan, K., Michaelis, J., Grimes, S., Jardine, P.J., Anderson, D.L., and Bustamante, C. (2005). Mechanism of force generation of a viral DNA packaging motor. Cell *122*, 683–692.

Cho, C., Reck-Peterson, S.L., and Vale, R.D. (2008). Regulatory ATPase sites of cytoplasmic dynein affect processivity and force generation. J. Biol. Chem. *283*, 25839–25845.

Churchman, L.S., Okten, Z., Rock, R.S., Dawson, J.F., and Spudich, J.A. (2005). Single molecule high-resolution colocalization of Cy3 and Cy5 attached to macromolecules measures intramolecular distances through time. Proc. Natl. Acad. Sci. U. S. A. *102*, 1419–1423.

Churchman, L.S., Flyvbjerg, H., and Spudich, J.A. (2006). A non-Gaussian distribution quantifies distances measured with fluorescence localization techniques. Biophys. J. *90*, 668–671.

Clancy, B.E., Behnke-Parks, W.M., Andreasson, J.O.L., Rosenfeld, S.S., and Block, S.M. (2011). A universal pathway for kinesin stepping. Nat. Struct. Mol. Biol. *18*, 1020–1027.

Corrie, J.E., Brandmeier, B.D., Ferguson, R.E., Trentham, D.R., Kendrick-Jones, J., Hopkins, S.C., van der Heide, U.A., Goldman, Y.E., Sabido-David, C., Dale, R.E., et al. (1999). Dynamic measurement of myosin light-chain-domain tilt and twist in muscle contraction. Nature *400*, 425–430.

DeWitt, M.A., Chang, A.Y., Combs, P.A., and Yildiz, A. (2012). Cytoplasmic dynein moves through uncoordinated stepping of the AAA+ ring domains. Science *335*, 221–225.

Dunn, A.R., and Spudich, J.A. (2007). Dynamics of the unbound head during myosin V processive translocation. Nat. Struct. Mol. Biol. *14*, 246–248.

Dunn, A.R., Chuan, P., Bryant, Z., and Spudich, J.A. (2010). Contribution of the myosin VI tail domain to processive stepping and intramolecular tension sensing. Proc Natl Acad Sci U S A *107*, 7746–7750.

Enderlein, J., Toprak, E., and Selvin, P.R. (2006). Polarization effect on position accuracy of fluorophore localization. Opt Express *14*, 8111–8120.

Fernández-Suárez, M., Baruah, H., Martínez-Hernández, L., Xie, K.T., Baskin, J.M., Bertozzi, C.R., Ting, A.Y., Fernandez-Suarez, M., and Martinez-Hernandez, L. (2007). Redirecting lipoic acid ligase for cell surface protein labeling with small-molecule probes. Nat Biotechnol *25*, 1483–1487.

Finer, J.T., Simmons, R.M., and Spudich, J.A. (1994). Single myosin molecule mechanics: piconewton forces and nanometre steps. Nature *368*, 113–119.

Firestone, A.J., Weinger, J.S., Maldonado, M., Barlan, K., Langston, L.D., O'Donnell, M., Gelfand, V.I., Kapoor, T.M., and Chen, J.K. (2012). Small-molecule inhibitors of the AAA+ ATPase motor cytoplasmic dynein. Nature *484*, 125–129.

Forkey, J.N., Quinlan, M.E., Shaw, M.A., Corrie, J.E.T., and Goldman, Y.E. (2003). Three-dimensional structural dynamics of myosin V by single-molecule fluorescence polarization. Nature *422*, 399–404.

Funatsu, T., Harada, Y., Tokunaga, M., Saito, K., and Yanagida, T. (1995). Imaging of single fluorescent molecules and individual ATP turnovers by single myosin molecules in aqueous solution. Nature *374*, 555–559.

Furuta, K., Furuta, A., Toyoshima, Y.Y., Amino, M., Oiwa, K., and Kojima, H. (2013). Measuring collective transport by defined numbers of processive and nonprocessive kinesin motors. Proc. Natl. Acad. Sci. U. S. A. *110*, 501–506.

Gelles, J., Schnapp, B.J., and Sheetz, M.P. (1988). Tracking kinesin-driven movements with nanometre-scale precision. Nature *331*, 450–453.

Gennerich, A., Carter, A.P., Reck-Peterson, S.L., and Vale, R.D. (2007). Force-induced bidirectional stepping of cytoplasmic dynein. Cell *131*, 952–965.

Gibbons, I.R., and Fronk, E. (1979). A latent adenosine triphosphatase form of dynein 1 from sea urchin sperm flagella. J. Biol. Chem. *254*, 187–196.

Gibbons, I.R., Garbarino, J.E., Tan, C.E., Reck-Peterson, S.L., Vale, R.D., and Carter, A.P. (2005). The affinity of the dynein microtubule-binding domain is modulated by the conformation of its coiled-coil stalk. J. Biol. Chem. *280*, 23960–23965.

Glynn, S.E., Martin, A., Nager, A.R., Baker, T. a, and Sauer, R.T. (2009). Structures of asymmetric ClpX hexamers reveal nucleotide-dependent motions in a AAA+ protein-unfolding machine. Cell *139*, 744–756.

Gordon, M.P., Ha, T., and Selvin, P.R. (2004). Single-molecule high-resolution imaging with photobleaching. Proc Natl Acad Sci U S A *101*, 6462–6465.

Ha, T., Enderle, T., Ogletree, D.F., Chemla, D.S., and Weiss, S. (1996). Probing the interaction between two single molecules: Fluorescence resonance energy transfer between a single donor and a single acceptor. Proc. Natl. Acad. Sci. *93*, 6264–6268.

Ha, T., Glass, J., Enderle, T., Chemla, D.S., and Weiss, S. (1998). Hindered Rotational Diffusion and Rotational Jumps of Single Molecules. Phys. Rev. Lett. *80*, 2093–2096.

Hohng, S., and Ha, T. (2004). Near-complete suppression of quantum dot blinking in ambient conditions. J. Am. Chem. Soc. *126*, 1324–1325.

Horio, T., and Hotani, H. (1986). Visualization of the dynamic instability of individual microtubules by dark-field microscopy. Nature *321*, 605–607.

Howarth, M., Takao, K., Hayashi, Y., and Ting, A.Y. (2005). Targeting quantum dots to surface proteins in living cells with biotin ligase. Proc Natl Acad Sci U S A *102*, 7583–7588.

Howarth, M., Liu, W., Puthenveetil, S., Zheng, Y., Marshall, L.F., Schmidt, M.M., Wittrup, K.D., Bawendi, M.G., and Ting, A.Y. (2008). Monovalent, reduced-size quantum dots for imaging receptors on living cells. Nat Methods *5*, 397–399.

Hua, W., Chung, J., and Gelles, J. (2002). Distinguishing inchworm and hand-over-hand processive kinesin movement by neck rotation measurements. Science *295*, 844–848.

Huang, B., Wang, W., Bates, M., and Zhuang, X. (2008). Three-dimensional super-resolution imaging by stochastic optical reconstruction microscopy. Science *319*, 810–813.

Huang, J., Roberts, A.J., Leschziner, A.E., and Reck-Peterson, S.L. (2012). Lis1 acts as a "clutch" between the ATPase and microtubule-binding domains of the dynein motor. Cell *150*, 975–986.

Ikezaki, K., Komori, T., Sugawa, M., Arai, Y., Nishikawa, S., Iwane, A.H., and Yanagida, T. (2012). Simultaneous observation of the lever arm and head explains myosin VI dual function. Small *8*, 3035–3040.

Imamula, K., and Kon, T. (2007). The coordination of cyclic microtubule association/dissociation and tail swing of cytoplasmic dynein. … Natl. Acad. … *104*, 16134–16139.

Imamula, K., Kon, T., Ohkura, R., and Sutoh, K. (2007). The coordination of cyclic microtubule association/dissociation and tail swing of cytoplasmic dynein. Natl. Acad. *104*, 16134–16139.

Irving, M., Allen, T.S., Sabido-David, C., Craik, J.S., Brandmeier, B., Kendrickjones, J., Corrie, J.E.T., Trentham, D.R., and Goldman, Y.E. (1995). Tilting of the light-chain region of myosin during step length changes and active force generation in skeletal muscle. Nature *375*, 688–691.

Kaiser, C.M., Goldman, D.H., Chodera, J.D., Tinoco, I., and Bustamante, C. (2011). The ribosome modulates nascent protein folding. Science *334*, 1723–1727.

Kalafut, B., and Visscher, K. (2008). An objective, model-independent method for detection of non-uniform steps in noisy signals. Comput. Phys. Commun. *179*, 716–723.

Kamei, T., Kakuta, S., and Higuchi, H. (2005). Biased binding of single molecules and continuous movement of multiple molecules of truncated single-headed kinesin. Biophys. J. *88*, 2068–2077.

Kardon, J.R., and Vale, R.D. (2009). Regulators of the cytoplasmic dynein motor. Nat. Rev. Mol. Cell Biol. *10*, 854–865.

Kaseda, K., Higuchi, H., and Hirose, K. (2003). Alternate fast and slow stepping of a heterodimeric kinesin molecule. Nat Cell Biol *5*, 1079–1082.

Kerssemakers, J., Ionov, L., Queitsch, U., Luna, S., Hess, H., and Diez, S. (2009). 3D nanometer tracking of motile microtubules on reflective surfaces. Small *5*, 1732–1737.

Kerssemakers, J.W.J., Munteanu, E.L., Laan, L., Noetzel, T.L., Janson, M.E., and Dogterom, M. (2006). Assembly dynamics of microtubules at molecular resolution. Nature *442*, 709–712.

Kliegman, J.I., Fiedler, D., Ryan, C.J., Xu, Y.-F., Su, X.-Y., Thomas, D., Caccese, M.C., Cheng, A., Shales, M., Rabinowitz, J.D., et al. (2013). Chemical Genetics of Rapamycin-Insensitive TORC2 in S. cerevisiae. Cell Rep. *5*, 1725–1736.

Kon, T., Nishiura, M., Ohkura, R., Toyoshima, Y.Y., and Sutoh, K. (2004). Distinct functions of nucleotide-binding/hydrolysis sites in the four AAA modules of cytoplasmic dynein. Biochemistry *43*, 11266–11274.

Kon, T., Mogami, T., Ohkura, R., Nishiura, M., and Sutoh, K. (2005). ATP hydrolysis cycle-dependent tail motions in cytoplasmic dynein. Nat. Struct. Mol. Biol. *12*, 513–519.

Kon, T., Imamula, K., Roberts, A.J., Ohkura, R., Knight, P.J., Gibbons, I.R., Burgess, S. a, and Sutoh, K. (2009). Helix sliding in the stalk coiled coil of dynein couples ATPase and microtubule binding. Nat. Struct. Mol. Biol. *16*, 325–333.

Kon, T., Sutoh, K., and Kurisu, G. (2011). X-ray structure of a functional full-length dynein motor domain. Nat. Struct. Mol. Biol. *18*, 638–642.

Kon, T., Oyama, T., Shimo-Kon, R., Imamula, K., Shima, T., Sutoh, K., and Kurisu, G. (2012). The 2.8 Å crystal structure of the dynein motor domain. Nature *484*, 345–350.

Kural, C., Kim, H., Syed, S., Goshima, G., Gelfand, V.I., and Selvin, P.R. (2005). Kinesin and dynein move a peroxisome in vivo: a tug-of-war or coordinated movement? Science *308*, 1469–1472.

Lacoste, T.D., Michalet, X., Pinaud, F., Chemla, D.S., Alivisatos, A.P., and Weiss, S. (2000). Ultrahigh-resolution multicolor colocalization of single fluorescent probes. Proc Natl Acad Sci U S A *97*, 9461–9466.

Lee, S., Sowa, M.E., Watanabe, Y., Sigler, P.B., Chiu, W., Yoshida, M., and Tsai, F.T.F. (2003). The structure of ClpB: a molecular chaperone that rescues proteins from an aggregated state. Cell *115*, 229–240.

Liao, J.-C.C., Elting, M.W., Delp, S.L., Spudich, J.A., and Bryant, Z. (2009). Engineered myosin VI motors reveal minimal structural determinants of directionality and processivity. J Mol Biol *392*, 862–867.

Mallik, R., Carter, B.C., Lex, S. a, King, S.J., and Gross, S.P. (2004). Cytoplasmic dynein functions as a gear in response to load. Nature *427*, 649–652.

Markus, S.M., Kalutkiewicz, K. a, and Lee, W.-L. (2012). She1-mediated inhibition of dynein motility along astral microtubules promotes polarized spindle movements. Curr. Biol. *22*, 2221–2230.

McKenney, R.J., Vershinin, M., Kunwar, A., Vallee, R.B., and Gross, S.P. (2010). LIS1 and NudE induce a persistent dynein force-producing state. Cell *141*, 304–314.

Mocz, G., and Gibbons, I.R. (2001). Model for the motor component of dynein heavy chain based on homology to the AAA family of oligomeric ATPases. Structure *9*, 93–103.

Moerner, W.E., and Kador, L. (1989). Optical detection and spectroscopy of single molecules in a solid. Phys Rev Lett *62*, 2535–2538.

Moffitt, J.R., Chemla, Y.R., Aathavan, K., Grimes, S., Jardine, P.J., Anderson, D.L., and Bustamante, C. (2009). Intersubunit coordination in a homomeric ring ATPase. Nature *457*, 446–450.

Mortensen, K.I., Churchman, L.S., Spudich, J.A., and Flyvbjerg, H. (2010). Optimized localization analysis for single-molecule tracking and super-resolution microscopy. Nat Methods *7*, 377–381.

Müllner, F.E., Syed, S., Selvin, P.R., Sigworth, F.J., and Mullner, F.E. (2010). Improved hidden Markov models for molecular motors, part 1: basic theory. Biophys J *99*, 3684–3695.

Nicastro, D., Schwartz, C., Pierson, J., Gaudette, R., Porter, M.E., and McIntosh, J.R. (2006). The molecular architecture of axonemes revealed by cryoelectron tomography. Science *313*, 944–948.

Nishikawa, S., Arimoto, I., Ikezaki, K., Sugawa, M., Ueno, H., Komori, T., Iwane, A.H., and Yanagida, T. (2010). Switch between large hand-over-hand and small inchworm-like steps in myosin VI. Cell *142*, 879–888.

Ohmachi, M., Komori, Y., Iwane, A.H., Fujii, F., Jin, T., and Yanagida, T. (2012). Fluorescence microscopy for simultaneous observation of 3D orientation and movement and its application to quantum rod-tagged myosin V. Proc Natl Acad Sci U S A *109*, 5294–5298.

Okten, Z., Churchman, L.S., Rock, R.S., and Spudich, J.A. (2004). Myosin VI walks hand-over-hand along actin. Nat Struct Mol Biol.

Ori-McKenney, K.M., Xu, J., Gross, S.P., and Vallee, R.B. (2010). A cytoplasmic dynein tail mutation impairs motor processivity. Nat. Cell Biol. *12*, 1228–1234.

Pertsinidis, A., Zhang, Y., and Chu, S. (2010). Subnanometre single-molecule localization, registration and distance measurements. Nature *466*, 647–651.

Qiu, W., Derr, N.D., Goodman, B.S., Villa, E., Wu, D., Shih, W., and Reck-Peterson, S.L. (2012). Dynein achieves processive motion using both stochastic and coordinated stepping. Nat Struct Mol Biol *19*, 193–200.

Rasnik, I., McKinney, S.A., and Ha, T. (2006). Nonblinking and long-lasting single-molecule fluorescence imaging. Nat. Methods *3*, 891–893.

Reck-Peterson, S., Yildiz, A., and Carter, A. (2006). Single-molecule analysis of dynein processivity and stepping behavior. Cell *126*, 335–348.

Rice, S., Lin, a W., Safer, D., Hart, C.L., Naber, N., Carragher, B.O., Cain, S.M., Pechatnikova, E., Wilson-Kubalek, E.M., Whittaker, M., et al. (1999). A structural change in the kinesin motor protein that drives motility. Nature *402*, 778–784.

Roberts, A.J., Numata, N., Walker, M.L., Kato, Y.S., Malkova, B., Kon, T., Ohkura, R., Arisaka, F., Knight, P.J., Sutoh, K., et al. (2009). AAA+ Ring and linker swing mechanism in the dynein motor. Cell *136*, 485–495.

Roberts, A.J., Malkova, B., Walker, M.L., Sakakibara, H., Numata, N., Kon, T., Ohkura, R., Edwards, T.A., Knight, P.J., Sutoh, K., et al. (2012). ATP-driven remodeling of the linker domain in the dynein motor. Structure *20*, 1670–1680.

Roberts, A.J., Kon, T., Knight, P.J., Sutoh, K., and Burgess, S.A. (2013). Functions and mechanics of dynein motor proteins. Nat. Rev. Mol. Cell Biol. *14*, 713–726.

Rust, M.J., Bates, M., and Zhuang, X. (2006). Sub-diffraction-limit imaging by stochastic optical reconstruction microscopy (STORM). Nat Methods *3*, 793–795.

Sase, I., Miyata, H., Corrie, J.E.T., Craik, J.S., and Kinosita Jr., K. (1995). Real time imaging of single fluorophores on moving actin with an epifluorescence microscope. Biophys. J *69*, 323–328.

SCHIFF, P.B., FANT, J., and HORWITZ, S.B. (1979). Promotion of microtubule assembly in vitro by taxol. Nature *277*, 665–667.

Schmidt, H., Gleave, E.S., and Carter, A.P. (2012). Insights into dynein motor domain function from a 3.3-Å crystal structure. Nat. Struct. Mol. Biol. *19*, 492–7, S1.

Schnitzer, M.J., and Block, S.M. (1995). Statistical kinetics of processive enzymes. Cold Spring Harb Symp Quant Biol *60*, 793–802.

Sen, M., Maillard, R.A., Nyquist, K., Rodriguez-Aliaga, P., Pressé, S., Martin, A., and Bustamante, C. (2013). The ClpXP Protease Unfolds Substrates Using a Constant Rate of Pulling but Different Gears. Cell *155*, 636–646.

Shima, T., Imamula, K., Kon, T., Ohkura, R., and Sutoh, K. (2006). Head-head coordination is required for the processive motion of cytoplasmic dynein, an AAA+ molecular motor. J. Struct. Biol. *156*, 182–189.

Shimozawa, T., Yamagata, K., Kondo, T., Hayashi, S., Shitamukai, A., Konno, D., Matsuzaki, F., Takayama, J., Onami, S., Nakayama, H., et al. (2013). Improving spinning disk confocal microscopy by preventing pinhole cross-talk for intravital imaging. Proc Natl Acad Sci U S A *110*, 3399–3404.

Silvanovich, A., Li, M.-G., Serr, M., Mische, S., and Hays, T.S. (2003). The third P-loop domain in cytoplasmic dynein heavy chain is essential for dynein motor function and ATP-sensitive microtubule binding. Mol. Biol. Cell *14*, 1355–1365.

Smith, A.M., and Nie, S. (2008). Minimizing the hydrodynamic size of quantum dots with multifunctional multidentate polymer ligands. J Am Chem Soc *130*, 11278–11279.

Sosa, H., Peterman, E.J.G., Moerner, W.E., and Goldstein, L.S.B. (2001). ADP-induced Rocking of the Kinesin Motor Domain Revealed by Single-Molecule Fluorescence Polarization Microscopy. Nat. Str. Biol. *8*, 540–544.

Svoboda, K., and Block, S.M. (1994). Force and velocity measured for single kinesin molecules. Cell *77*, 773–784.

Svoboda, K., Schmidt, C.F., Schnapp, B.J., and Block, S.M. (1993). Direct observation of kinesin stepping by optical trapping interferometry. Nature *365*, 721–727.

Syed, S., Snyder, G.E., Franzini-Armstrong, C., Selvin, P.R., and Goldman, Y.E. (2006). Adaptability of myosin V studied by simultaneous detection of position and orientation. EMBO J. *25*, 1795–1803.

Thompson, R.E., Larson, D.R., and Webb, W.W. (2002). Precise Nanometer Localization Analysis for Individual Fluorescent Probes. Biophys. J. *82*, 2775–2783.

Thoresen, T., and Gelles, J. (2008). Processive movement by a kinesin heterodimer with an inactivating mutation in one head. Biochemistry *47*, 9514–9521.

Toba, S., Watanabe, T.M., Yamaguchi-Okimoto, L., Toyoshima, Y.Y., and Higuchi, H. (2006). Overlapping hand-over-hand mechanism of single molecular motility of cytoplasmic dynein. Proc Natl Acad Sci U S A *103*, 5741–5745.

Tokunaga, M., Kitamura, K., Saito, K., Iwane, A.H., and Yanagida, T. (1997). Single Molecule Imaging of Fluorophores and Enzymatic Reactions Achieved By Objective-Type Total Internal Reflection Fluorescence Microscopy. Biochem. Biophys. Res. Commun. *235*, 47–53.

Toyoshima, Y.Y., Kron, S.J., and Spudich, J.A. (1990). The myosin step size: measurement of the unit displacement per ATP hydrolyzed in an in vitro assay. Proc Natl Acad Sci U S A *87*, 7130–7134.

Tsygankov, D., Serohijos, A.W.R., Dokholyan, N. V, and Elston, T.C. (2009). Kinetic models for the coordinated stepping of cytoplasmic dynein. J. Chem. Phys. *130*, 025101.

Vale, R.D., Reese, T.S., and Sheetz, M.P. (1985). Identification of a novel force-generating protein, kinesin, involved in microtubule-based motility. Cell *42*, 39–50.

Vale, R.D., Funatsu, T., Pierce, D.W., Romberg, L., Harada, Y., and Yanagida, T. (1996). Direct observation of single kinesin molecules moving along microtubules. Nature *380*, 451–453.

Vallee, R.B., Williams, J.C., Varma, D., and Barnhart, L.E. (2004). Dynein: An ancient motor protein involved in multiple modes of transport. J. Neurobiol. *58*, 189–200.

Vallee, R.B., McKenney, R.J., and Ori-McKenney, K.M. (2012). Multiple modes of cytoplasmic dynein regulation. Nat. Cell Biol. *14*, 224–230.

Vogelsang, J., Kasper, R., Steinhauer, C., Person, B., Heilemann, M., Sauer, M., and Tinnefeld, P. (2008). A reducing and oxidizing system minimizes photobleaching and blinking of fluorescent dyes. Angew Chem Int Ed Engl *47*, 5465–5469.

W. J. Moberly Chan, D. P. Adams, M. J. Aziz, G. Hobler, and T. Schenkel (2007). Fundamentals of Focused Ion Beam Nanostructural Processing: Below, At, and Above the Surface. Mater. Res. Soc. MRS Bull. *32*.

Warshaw, D.M., Kennedy, G.G., Work, S.S., Krementsova, E.B., Beck, S., and Trybus, K.M. (2005). Differential labeling of myosin V heads with quantum dots allows direct visualization of hand-over-hand processivity. Biophys J *88*, L30–2.

Yi, J.Y., Ori-McKenney, K.M., McKenney, R.J., Vershinin, M., Gross, S.P., and Vallee, R.B. High-resolution imaging reveals indirect coordination of opposite motors and a role for LIS1 in high-load axonal transport .

Yildiz, A., and Selvin, P.R. (2005). Fluorescence imaging with one nanometer accuracy: application to molecular motors. Acc Chem Res *38*, 574–582.

Yildiz, A., Forkey, J.N., McKinney, S. a, Ha, T., Goldman, Y.E., and Selvin, P.R. (2003). Myosin V walks hand-over-hand: single fluorophore imaging with 1.5-nm localization. Science *300*, 2061–2065.

Yildiz, A., Tomishige, M., Vale, R.D., and Selvin, P.R. (2004a). Kinesin walks hand-over-hand. Science *303*, 676–678.

Yildiz, A., Park, H., Safer, D., Yang, Z., Chen, L.Q., Selvin, P.R., and Sweeney, H.L. (2004b). Myosin VI Steps via a Hand-over-Hand Mechanism with Its Lever Arm Undergoing Fluctuations when Attached to Actin. J Biol Chem *279*, 37223–37226.

Yildiz, A., Tomishige, M., Gennerich, A., and Vale, R.D. (2008). Intramolecular strain coordinates kinesin stepping behavior along microtubules. Cell *134*, 1030–1041.

Zhang, X., Shaw, a, Bates, P. a, Newman, R.H., Gowen, B., Orlova, E., Gorman, M. a, Kondo, H., Dokurno, P., Lally, J., et al. (2000). Structure of the AAA ATPase p97. Mol. Cell *6*, 1473–1484.

Zhuang, L., Zhang, J., and Xiang, X. (2007). Point mutations in the stem region and the fourth AAA domain of cytoplasmic dynein heavy chain partially suppress the phenotype of NUDF/LIS1 loss in Aspergillus nidulans. Genetics *175*, 1185–1196.